The Thesis Committee for Adam Carl Schulz
Certifies that this is the approved version of the following thesis:

Characterization of Connection Details for Truss-Diaphragm for Use in Full-Scale Experiments Focused on Lateral Contribution of Gravity Connections in Steel Frames

APPROVED BY
SUPERVISING COMMITTEE:

Patricia Clayton, Supervisor

Todd Helwig

Characterization of Connection Details for Truss-Diaphragm for Use in Full-Scale Experiments Focused on Lateral Contribution of Gravity Connections in Steel Frames

by

Adam Carl Schulz

Thesis

Presented to the Faculty of the Graduate School of

The University of Texas at Austin

in Partial Fulfillment

of the Requirements

for the Degree of

Master of Science in Engineering

The University of Texas at Austin

May 2021

ACKNOWLEDGEMENTS

For their time, knowledge, and support I would like to thank Dr. Patricia Clayton and Dr. Todd Helwig. I appreciate your guidance both in the completion of the project and in writing this thesis. I also thank Sangwook Park, who was a pleasure to work with in and out of the lab.

I would also like to thank my family and friends for their support and encouragement throughout this process.

ABSTRACT

Characterization of Connection Details for Truss-Diaphragm for Use in Full-Scale Experiments Focused on Lateral Contribution of Gravity Connections in Steel Frames

Adam Carl Schulz, M.S.E

The University of Texas at Austin, 2021

Supervisor: Patricia Clayton

Typical structures derive lateral strength and stiffness from only a limited number of lateral load resisting elements. Gravity framing normally accounts for the vast majority of members in a structure and is assumed not to contribute to the lateral resistance of the frame. This assumption is partly due to the perfect pin idealization for gravity connections. However, research has indicated that gravity framing offers a nonnegligible amount of lateral resistance both due to moment resistance in the connections and continuity of gravity columns. In aggregate, the moment resistance of gravity framing may substantially impact the lateral capacity of a structure. This thesis presents the details of a system-level test specimen that will be used to evaluate the contribution of gravity framing to the lateral resistance of a steel building structure. This overall research investigation is an extension of the work published by Donahue (2019) and employs many of the same details. The specimen described herein is a two-bay by three-bay structure that utilizes double-angle shear connections in the direction of loading. This structure represents one floor of a representative building with columns spanning from mid-height of the story below to

mid-height of the story above. The specimen will be tested as a bare-steel frame to collect calibration data for forthcoming tests that include composite decking. In addition to explaining the geometry of the specimen, this thesis details computational and experimental testing completed to validate a horizontal-to-vertical connection between a knife plate and a WT section in a top truss diaphragm that is used to distribute lateral loads throughout the specimen. This connection was designed with the intent that the WT section will accommodate bending while limiting permanent deformations in the knife plate. While the knife plate was observed to experience substantial plastic strains in experimental subassembly testing, it was decided that the magnitude of residual deformation sustained by the knife plate would not substantially impact the constructability of subsequent test specimens. Therefore, the detail was used in the full-scale system-level specimen.

TABLE OF CONTENTS

LIST OF FIGURES

LIST OF TABLES

1 INTRODUCTION

In steel construction, standard practice is to detail a limited number of frames in a structure to resist lateral loads induced by wind and seismicity while detailing the rest of the structure to resist only gravity loads. Gravity framing connections are idealized as perfect pins, having no resistance to moment and contributing no stiffness to the structural system. Prior research has indicated that gravity framing commonly seen in practice has a nonnegligible contribution to the lateral strength and stiffness of a structure. This contribution can arise from moment resistance in the connection itself, as discussed in Leon's work on partially restrained frames (1990), or it may be a result of frame action in continuous gravity columns as theorized in Foutch and Yun (2002) and Flores, Charney, and Lopez-Garcia (2014). A more thorough understanding of structural performance including the lateral contribution of gravity framing will allow designers to evaluate the collapse safety of existing buildings and the need for strengthening measures to achieve a safe building with an acceptable level of collapse risk. Including the resistance provided by gravity framing connections may give designers a powerful tool in reducing costly and invasive strengthening methods during retrofit projects.

The experimental database concerning the lateral resistance of gravity framing is largely focused on bare-steel connections. Research completed by Donahue (2019) sought to quantify the lateral contribution of gravity framing in composite construction using a cruciform test specimen. This specimen included a representative gravity column in a typical structure with composite girders framing in on each side. Moment-rotation relationships were established using this experimental setup, but several unforeseen behaviors limited the applicability of the data. Chief among these behaviors was the phenomenon of frame expansion, the increase in distance

between two column-lines as the structure deforms laterally. This phenomenon led to cracking of the deck, limiting the ability of the connections to resist moments. This limitation of the cruciform test setup motivated the full-scale, multi-bay experiment described in this thesis. Additionally, literature concerning the impact of gravity framing identifies frame action of continuous columns as a lateral force resisting mechanism (Foutch & Yun, 2002; Flores, Charney, & Lopez-Garcia, 2014). To more fully account for the impact of gravity framing on system-level behavior, the research described in this thesis seeks to expand Donahue's work using a full-scale specimen representative of a typical steel structure.

A two-bay by three-bay composite steel gravity frame was designed using the member sizes and details presented in Donahue (2019). Auxiliary components including the truss diaphragm connecting the tops of each column and the fixture of the assembly to the strong floor were designed in Saavedra (2020) and Hernandez (2020). Before testing with a composite slab, a bare-steel calibration test will be completed to observe the behvior of the specimen. The design of this specimen is described in this thesis. While most of the bare-steel specimen design was within the scope of typical design practice, one connection was subject to increased scrutinity. The tops of the columns were connected to the horizontal truss diaphragm using a vertical-to-horizontal connection that utilized a WT section. This was dubbed the "T-stub connection." This connection was intended to concentrate deformations in the easily replacable T-stub rather than in the truss member framing into the connection. Preliminary analysis suggested that the connection did not behave in this manner and deformations instead were shared between the connection component and the truss component. To assess the efficacy of the connection, computational and experimental trials were completed to characterize the behavior of the connection with respect to the design intent.

1.1 Scope

The primary objectives of this thesis are to present a comprehensive description of the bare-steel test specimen and to explain the experimental program that was used to validate the T-stub connection. The full-scale assembly described herein was designed according to the forces predicted in the pushover model developed by Hernandez (2020). This thesis explains the design of the test specimen based on those forces. Each detail of the bare-steel assembly, as presented in the structural plan, is described in this thesis. Analysis of the T-stub connection, including design, computational analysis, and experimental testing, is also described. Instrumentation, loading, and data analysis are described and reccomendations concerning the use of the detail are delivered.

1.2 Outline

The following chapter provides a summary of the existing literature that influenced the development of the research program. Research contributing to the development of this experiment has been divided into three categories: experimental testing of bare-steel connections, experimental testing of composite connections, and computational analysis that incorporates partially restrained behavior of gravity connections. Chapter 3 describes the framing and details that will be used in the bare-steel test. This chapter provides the design basis of the specimen as well as a physical description of the assembly. Chapter 4 describes the analysis of the T-stub connection described previously. Analysis of the T-stub connection including both computational analysis as well as an experimental trial are described. Finally, Chapter 5 presents the key results from the previous sections and contains recommendations for future work.

2 LITERATURE REVIEW

Prior research has established the expected behavior of individual double-angle connections, though little of that research has focused on the bending behavior of gravity connections in system-level testing. This review presents several key publications that informed the research presented in this thesis. The review is divided into sections that cover existing experimental research of both bare-steel and composite connections, as well as computational research on the system-level impact of gravity framing on the seismic response of buildings. Donahue (2019), presented in the section on composite connections, was a direct precursor to the original research presented in this thesis. This review informed both the design of the specimen presented herein and aided the researchers in predicting failure modes and behavior patterns that are expected in the experimental phase.

2.1 Experimental Testing of Bare-Steel Connections

2.1.1 Shen and Astaneh-Asl (1999)

Shen and Astaneh-Asl (1999) presented a study analyzing the moment-rotation behavior and ductility of bolted, top-and-bottom seated, semi-rigid angle connections, such as those depicted in **Figure 2-1(a)**. Rather than testing the full connection, a simplified model consisting of two angles and a flange was tested under cyclic axial load. This simplification is shown in **Figure 2-1(b)** and is justified by the nominal flexural behavior of a top and seat angle connection, which derives resistance primarily from the moment arm between the top and bottom angles in compression and tension, respectively (Shen & Astaneh-Asl, 1999). While not directly analogous to the bare-steel gravity framing with double-angle connections described in Section 3.2.1 of this thesis, this test program does provide insight into the behavior of connection angles as an isolated component.

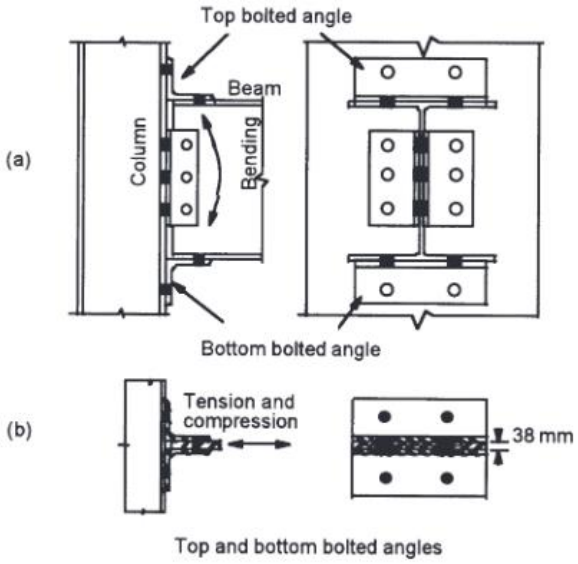

Figure 2-1: (a) Subject connection and (b) experimental simplification *(Shen & Astaneh-Asl, 1999)*

Eight experiments were conducted with four different angles. The angles tested were L3 ½ x 4 x ⅜, L3 ½ x 4 x ½, L4 x 6 x ½, and L4 x 6 x ¾. These were connected to the web of a W14x120 beam and reacted against a rigid plate. The L3 ½ x 4 sections were connected with ¾ inch bolts while the L4 x 6 sections were connected with 1-inch bolts. All bolts were fully pretensioned using the turn-of-nut method. There was minor variation in the gage distance of the bolt groups (commensurate with the size of the angle) and the clearance between the beam web and the reaction plate. In terms of yield load, maximum load, and energy dissipated, these variables had a lesser impact than the relationship between angle and bolt strength. A schematic view of the cyclic displacement pattern is shown in **Figure 2-2**.

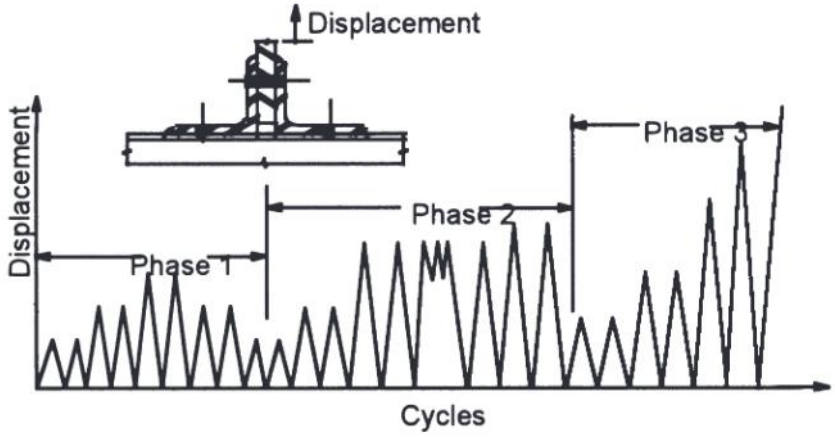

Figure 2-2: Cyclic displacement pattern for double angle connection *(Shen & Astaneh-Asl, 1999)*

The researchers observed distinct pre-yield, transitionary, and post-yield responses in the behavior of the angles. Before yield, the connection exhibited minimal elastic deformation and there was significant stiffness loss as the angles transitioned to plastic behavior. The transitionary period was described by the authors as "the response between first yielding and the formation of a mechanism" (Shen & Astaneh-Asl, 1999). The post-yield response exhibited the most deformation as well as the most strength. The authors attributed the increased strength of the connection primarily to catenary action in the angle legs and strain hardening. Ductility, defined

as the maximum displacement divided by the displacement and full yield, was between 8 and 10 for all specimens.

Depending on the thickness of the angle and the size of the bolts, different post-yield deformation patterns were observed for the different specimens. The authors distinguished between “thin angle” connections and “thick angle” connections: those configurations where the angle was weak relative to the bolts were described as “thin angle,” while configurations where the angle was strong relative to the bolts were described as “thick angle.” Typical failure modes are shown in **Figure 2-3**. Thin angles tended to yield at the bolt line and fillet toe on the reaction plate leg (Pattern 1 in **Figure 2-3**). The bolts in both the reaction plate and the beam web remained elastic. Thick angles, by contrast, tended to yield along the outside edge of the reaction plate bolt line and at the fillet toe on the beam side leg (Pattern 2 in **Figure 2-3**). The reaction plate bolts yielded and, in the new deformed configuration, large plastic rotation demand was placed on the fillet of the angles. In both configurations, failure most often occurred in the form of fracture on the side of the fillet where yielding occurred. This form of failure was attributed to low cycle fatigue. Secondary strength failure modes that controlled in two of the specimens consisted of bolt tear-out and bolt shear. Even the two strength-controlled specimens exhibited cracking near the fillet due to low cycle fatigue. For this reason, the strength failure modes were considered secondary. Monotonic testing showed a 30% increase in strength and ductility for a thin angle specimen when compared to cyclic testing. Little difference was observed between the cyclic and monotonic strength and ductility of a thick angle specimen.

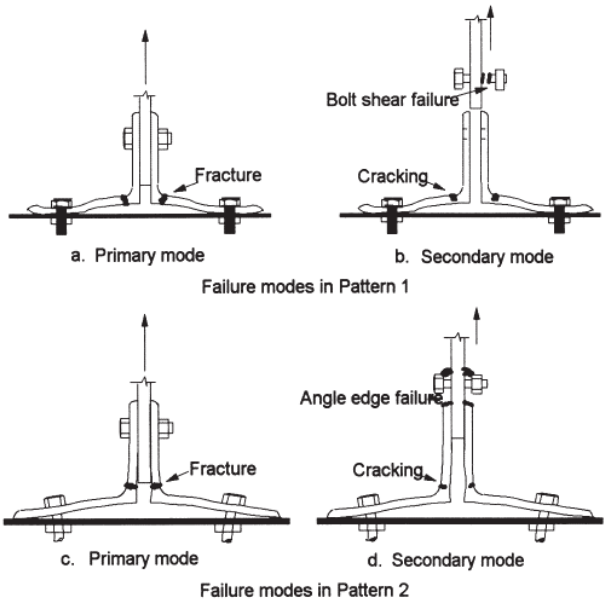

Figure 2-3: Typical failure modes for thin angles (a & b) and thick angles (c & d) *(Shen & Astaneh-Asl, 1999)*

The hysteretic behavior of the connections were also delineated by the thickness of the angles. As shown in **Figure 2-4**, thin angle connections such as Specimen 5 had only minor pinching in their hysteretic loops while Specimen 6, a thick angle connection, demonstrated much more pinching. This effect is attributed to the deformation of the bolts in thick angle connections: the resulting gap was closed at the beginning of each cycle before the stiffer mechanism was engaged. Some pinching also occurred due to bolt slip when the force in the connection exceeded the capacity of the slip-critical connection. This effect was persistent in cycles after the initial slip took place.

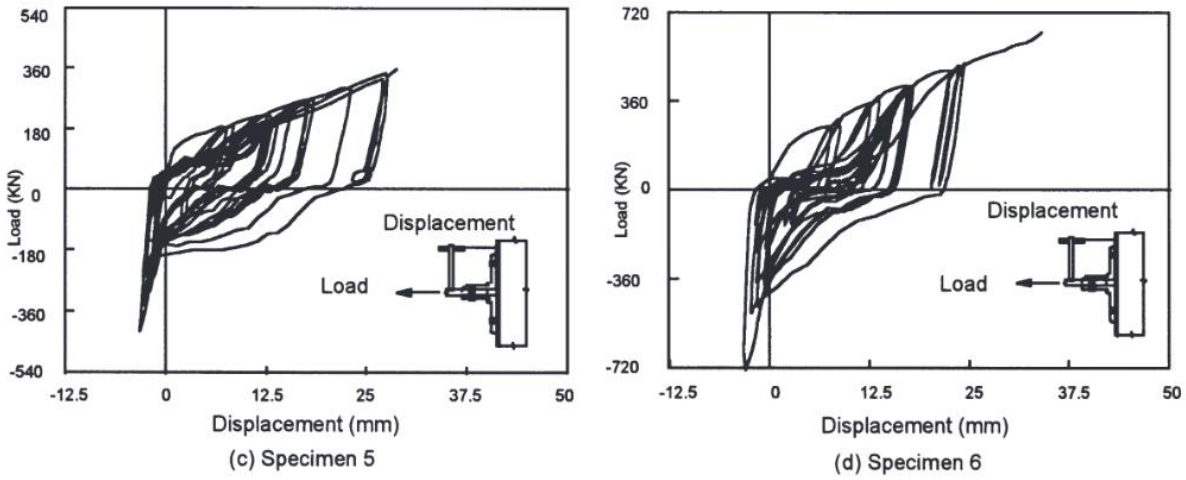

Figure 2-4: Hysteresis curves for (c) thin angle connection and (d) thick angle connection *(Shen & Astaneh-Asl, 1999)*

This study by Shen and Astaneh-Asl suggests that the cyclic behavior of double angle connections is characterized by wide hysteretic loops with some pinching. The bare-steel test assembly presented in this thesis utilizes a double-angle connection detail that is similar in configuration and scale to those tested in the 1999 study. Therefore, there is reason to believe that the connections in the bare-steel test will dissipate energy within the same order of magnitude as those in the prior research. Further, while this test focusses on the energy dissipation of one double-angle connection, it is unknown how many of these connections will behave in aggregate. This knowledge gap motivates system level testing. Additionally, Shen and Astaneh-Asl identify common failure modes for double angle connections. Prior knowledge of failure modes will help the researchers involved in this thesis instrument and observe the specimen efficiently and in high detail.

2.2 Experimental Testing of Composite Connections

2.2.1 Leon (1990)

In this study, Leon uses experimental data collected on a variety of semirigid connections to present strategies for analysis and design of systems that economically utilize such connections (Leon, 1990). The author focuses on developing bilinear moment-rotation curves to simulate the inherent nonlinearity of the connections. The paper focuses on composite connections due to the added resistance of a concrete slab.

Figure 2-5 shows the four types of connections tested. These four specimens represent some typical configurations that may be found in existing buildings or specified in new construction. Connection Type A featured a seat angle at the bottom of the beam section and clip angles on either side of the web. Connection Type B was similar except that it used a welded plate as a seat for the beam rather than an angle. Connection C used only a seat angle. Finally, connection Type D was a double angle connection, similar to the gravity connections that are the subject of this thesis. All connections were topped by a composite floor slab. Connection Type A was tested both monotonically and cyclically in the cruciform and subassembly setups shown in **Figure 2-6**. All other connections were tested in the cruciform setup only. Cyclic loading was applied up to 3% drift. Note that these connections are intended for areas of low seismicity. Therefore, values consistent with wind loading were used.

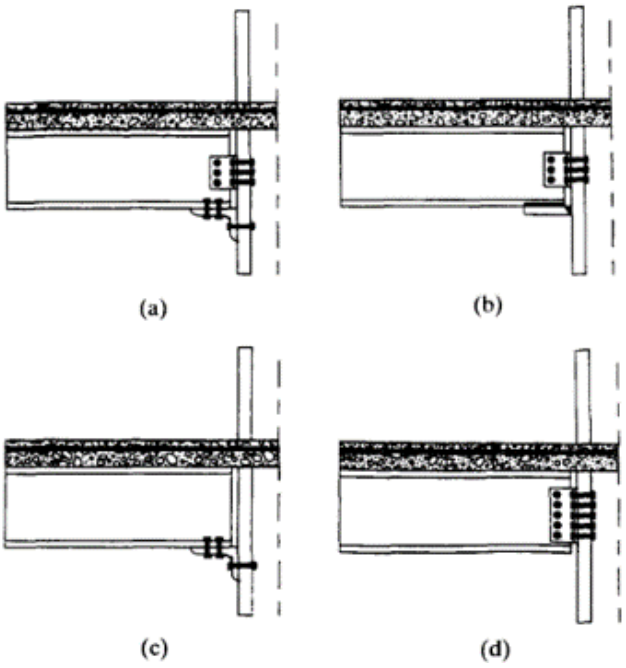

Figure 2-5: Four tested connection types *(Leon, 1990)*

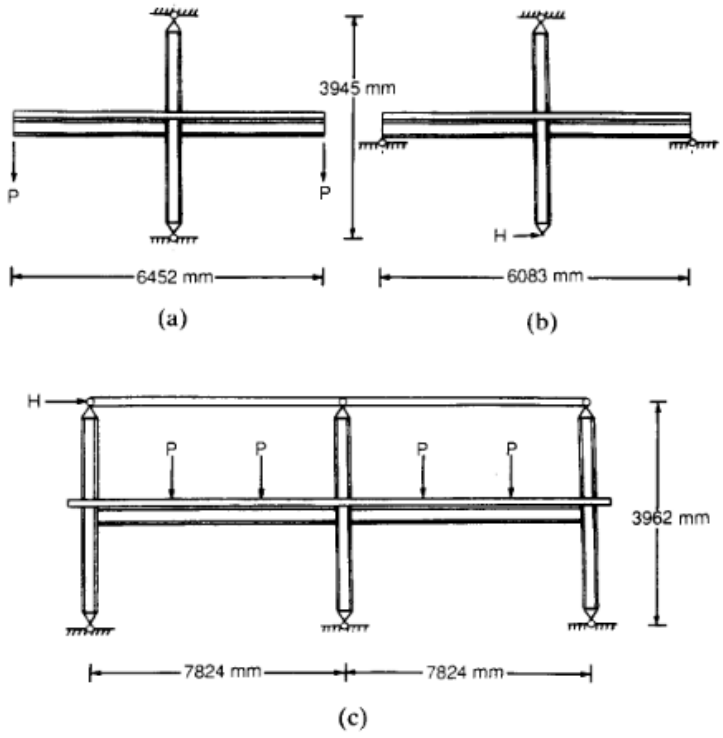

Figure 2-6: (a) Monotonic single connection setup, (b) Cyclic single connection setup, (c) Subassembly setup *(Leon, 1990)*

Type A connections, which were tested both in a cruciform subassembly and in a frame assembly, are of particular interest to this thesis as the research presented herein is an expansion of Donahue's (2019) cruciform subassembly tests to a system-level specimen. The primary observation made by Leon was that the exterior connections – i.e. those on the boundary of the specimen – resisted the same amount of moment as the interior connections. The slab was extended over the exterior connections by two feet to provide for development of the reinforcing bars, a detail that is impractical and uncommon in practice (Leon, 1990). Leon posited that development of the slab reinforcement is neccesary to ensure uniform performance of the connections and reccomended that mechanical anchorage be provided at the slab boundary. This thesis focuses on gravity connections, not partially restrained connections as in Leon's research, therefore it is unlikely that special detailing would be provided. In the bare-steel study, the relative engagement of each gravity connection will be studied. When a composite slab is added in the future, the researchers expect to observe less engagement along the boundary in agreement with Leon's work.

The limit states identified by the author for connection Type D are relevant to the topic of this thesis due to that connection's similarity with the connections used in this research. The connections designed by Leon were not meant to be simple gravity connections, but were instead detailed to resist moments by specifying the maximum number of bolts that could fit in between the flanges. In cruciform testing, Leon observed bolt-hole deformation in the beam web at the bottom bolts, which resulted in a decrease in stiffness. Additionally, the two angles tended to pull away from the column. This behavior was consistent with the results of Shen & Astaneh-Asl (1999). Low-cycle fatigue was also a failure mechanism in the angle; fatigue fracture was observed after cycles exceeded 3% drift. All of these failure modes were also observed in

research by Donahue (2019). This consensus in the literature will inform the instrumentation for the specimen presented in this thesis.

2.2.2 Donahue (2019)

The original research presented in this thesis builds upon the work done by Donahue at the University of Texas at Austin. This 2019 dissertation detailed the collection and analysis of experimental cyclic load response data for full scale, composite double-angle connections. A cruciform subassembly, shown in **Figure 2-7**, was used to test the seven specimens listed in **Table 2-1**. The subassembly test set-up was designed to capture the interaction between a W12x96 column and W21x55 beams connected with bolted-bolted double angles and overlain with a 4.5-inch composite concrete slab on 2-inch metal deck. As detailed in **Table 2-1**, trials were conducted with a bolted-welded connection and "bare-steel" specimens that did not include a composite slab. Specimen B-BB – a specimen featuring a bolted-bolted connection and no composite slab – is of particular interest in this thesis because this configuration was used for the system level test conducted.

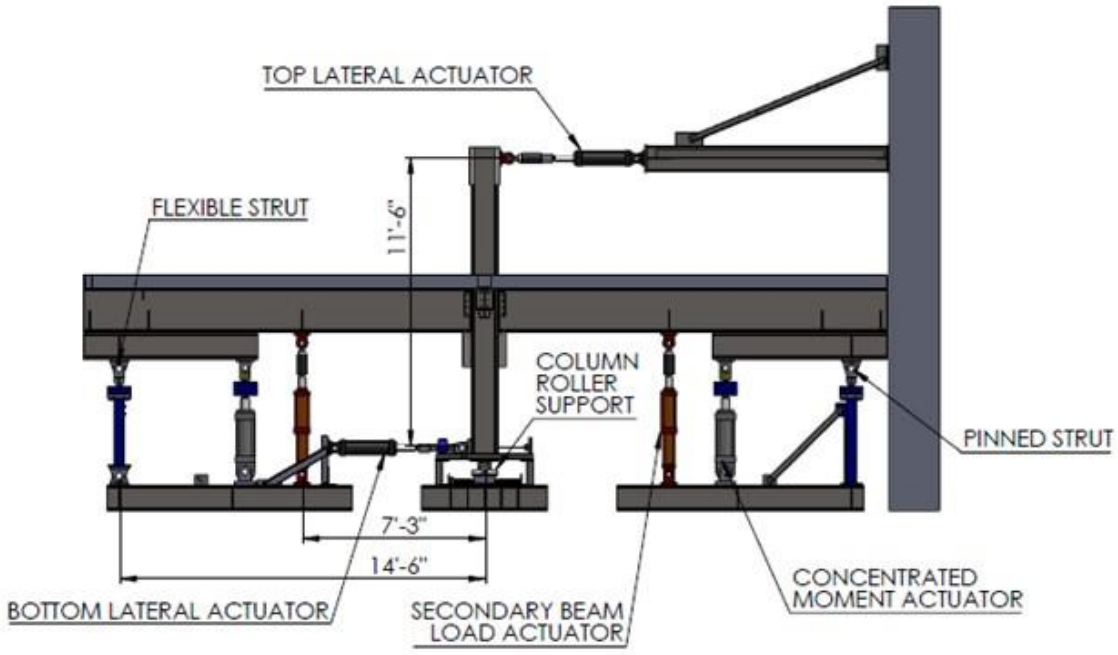

Figure 2-7: Cruciform testing subassembly from Donahue (2019)

Table 2-1: Test specimen details *(Donahue, 2019)*

Specimen Name	Angle Size	Bolts	Weld Size	Deck Orientation	Other Notes
B-WB	2L4x3-1/2x1/4 11-1/2" Long	3/4" A325 Bolts 4 Rows	3/16"	N/A	
B-BB	2L4x4x1/4 11-1/2" Long	3/4" A325 Bolts 4 Rows	N/A	N/A	
S-SC	2L4x4x1/4 11-1/2" Long	3/4" A325 Bolts 4 Rows	N/A	Parallel to Girder	
S-LS	2L4x4x1/4 11-1/2" Long	3/4" A325 Bolts 4 Rows	N/A	Parallel to Girder	Longitudinal Seam at Column Line
S-HA	2L4x4x5/8 17-1/2" Long	3/4" A325 Bolts 6 Rows	N/A	Parallel to Girder	
W-SC	2L4x4x1/4 11-1/2" Long	3/4" A325 Bolts 4 Rows	N/A	Perpendicular to Girder	
W-CC	2L4x4x1/4 11-1/2" Long	3/4" A325 Bolts 4 Rows	N/A	Perpendicular to Girder	#4 Bars 5' Long at 6" Spacing at Column Line
W-RB	2L4x4x1/4 11-1/2" Long	3/4" A325 Bolts 4 Rows	N/A	Perpendicular to Girder	Ring Beam Around Test Slab Restraining Expansion

Actuators on the beams were used to apply forces and moments corresponding to ASCE 7 gravity loading. Lateral loads were applied using actuators at the top and bottom of the column – a half story above and below the connection. These points displaced in opposite directions to produce the cyclic drift pattern described in the SAC loading protocol defined in FEMA 355

(2000) with minimal lateral translation of the slab. This setup simulated the interaction between an in-situ column and floor slab in a full building assembly.

Donahue identified several key phenomena and failure mechanisms that occurred as the bare-steel test progressed. In the angles that made up the connection, deformations in the form of prying or catenary action were observed as the angle pulled away from the column, consistent with the deformations observed in Shen & Astaneh-Asl (1999). Bolt-hole deformation occurred in both the angle and the web of the beam early in the experiment. Yielding around the bolt holes progressed to fracture at the top and bottom of the angles as drifts exceeded 8%. As drifts reached 6% and the effects of low-cycle fatigue began to develop, angles were observed tearing at the top heels. Cracking at the top of the heel and at the bolt holes can be observed in **Figure 2-8**. The bottom heels began to tear at a drift of 8%. This effect was accelerated when the flange of the beam made contact with the face of the column; the resulting point of contact was stiff enough to become the center of rotation of the connection. This phenomenon resulted in a large moment arm that placed significant tensile demands on the extreme top or bottom of the angle, resulting in a tear that progressed to complete or partial fracture. For Specimen B-BB, all four angles avoided complete fracture because the tears originating at the top formed in the column side of the angle while the tears originating at the bottom formed in the beam side of the angle. This tearing left a small isthmus of steel between the two tears that was still capable of carrying gravity load. The tearing pattern observed by Donahue was consistent with Shen & Astaneh-Asl (1999) in that cracking initiated in the heels of the angles. However, the cracking pattern was not consistent with the dichotomy of thick and thin angle behavior from the previous study. Shen & Astaneh-Asl observed that thin angles tended to crack on the column-side leg while thick angles tended to crack on the girder-side leg. Cracking on both legs as observed by Donahue may be the

result of the bending load pattern that was applied to the angles in the experiments. Specimens in Shen & Astaneh-Asl (1999) were subjected to uniform translation perpendicular to the column flange while the angles in Donahue's test were subjected to bending. The major phenomena observed by Donahue, tagged with the drift at which they initiated, are reproduced in **Table 2-2**. Bolt hole deformation on the girder, visible as yielding near the bolt holes in **Figure 2-9**, led to the conclusion that the primary moment-resisting mechanism in the connection at high rotations was the force couple between the bearing flange (compression) and the clip angle (tension). Note that this mechanism only existed under negative moment; in positive bending, the flange did not make contact with the column and thus the moment resistance was limited to the self-reacting capacity of the clip angles.

Figure 2-8: Cracking pattern in the angles initiating at 6% drift at the heel and 8% drift at the bolt hole (Donahue 2019)

Table 2-2: Phenomena observed during B-BB test (Donahue 2019)

Drift (%)	Phenomenon
1.5	Elastic deformation of clip angle
2.5	Slip between beam web and clip angle*
3.0	Plastic deformation of clip angle
3.5	Initial flange contact (binding), yielding between bolts and at top of angles
6.0	Tearing at the top heel of clip angles
8.0	Tearing at bottom heel of clip angles
10.0	Tearing reaches full depth, test setup reaches limit (end)

* Continued bolt slip was observed throughout the test as metallic pinging

Figure 2-9: Girder bolt hole deformation, Specimen B-BB (Donahue 2019)

The moment-rotation response of the bare-steel bolted-bolted connection is shown in **Figure 2-10**. Pinching of the hysteretic loops occurred at large negative moments. This behavior was due to flange binding, which increased the stiffness of the connection. Ultimately, the connection only reached 11% of the plastic moment capacity of the beam.

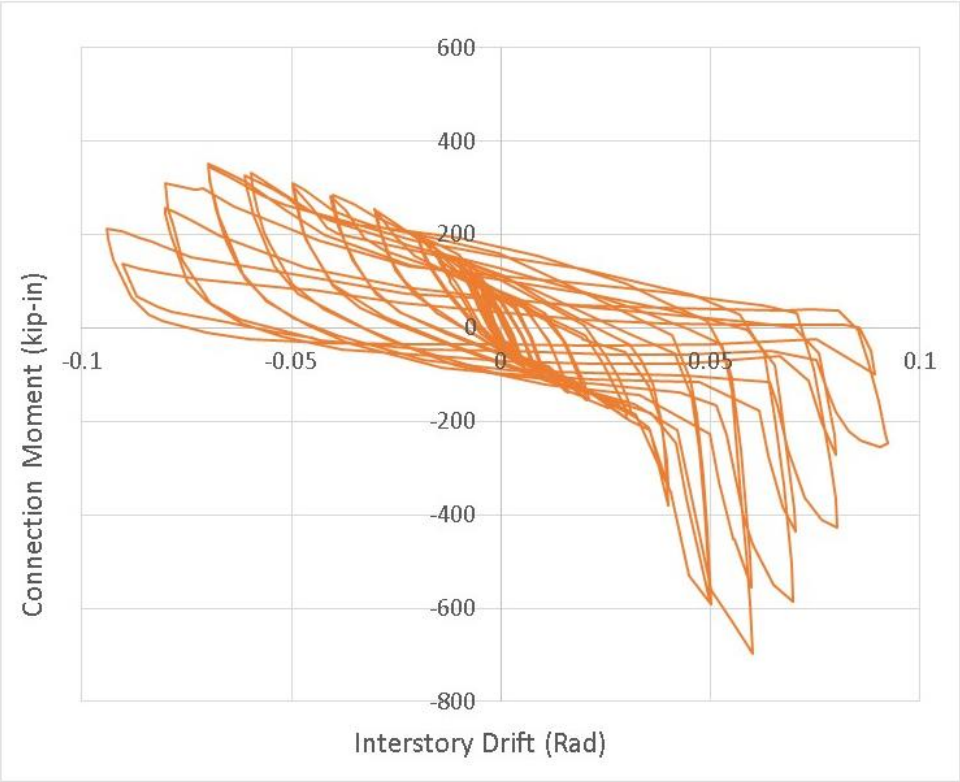

Figure 2-10: Moment-rotation response of bare-steel bolted-bolted connection (Donahue 2019)

2.3 Computational Analysis of the Effect of Gravity Framing on Seismic Response

2.3.1 Foutch and Yun (2002)

In this study, Foutch and Yun compared simple and complex nonlinear modelling methods of two prototype buildings with moment resisting frames (MRFs) designed according to the 1997 NEHRP provisions to identify high-fidelity methods that may be worth incorporating into design practice. These models varied in their use of rigid-end offsets, panel zones, nonlinear springs to simulate partially restrained connections, and the inclusion of gravity framing (in the form of an equivalent gravity bay) (Foutch & Yun, 2002). Models were analyzed both statically and dynamically. Models were constructed with and without the contribution of a composite slab. For the purposes of this thesis, the model M2-SC is of most interest. This model used rigid end offsets, nonlinear springs for the beam-column connections and panel zones, and one bay to represent the internal gravity columns. Comparisons may be drawn between this model and model M2-WO, which used a leaner column on each story to capture P-Δ effects rather than an internal gravity bay, as well as M2-COMP, which incorporated a composite deck.

Gravity connections in the composite model were modelled using flexural hinges to simulate the simple connection response seen in **Figure 2-11**. This model is based on the interaction between the clip angle (tension) and the composite slab (compression); for the model lacking a composite slab, gravity connections were modelled using the conventional pin approximation. A visualization of the model including the equivalent gravity framing bay is shown in **Figure 2-12**. The authors observed that the interaction of the continuous columns combined with the rigid diaphragm (typical in all buildings regardless of composite or non-

composite construction) produced significant lateral resistance independent of the beam-column connection model.

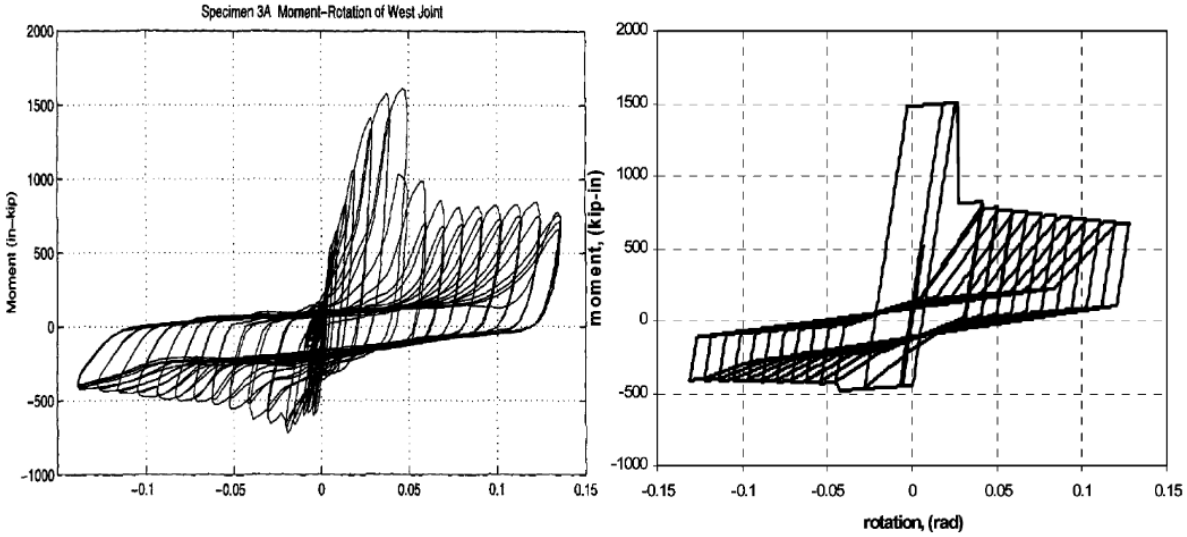

Figure 2-11: Moment-rotation relationship for gravity connection with composite slab *(Foutch & Yun, 2002)*

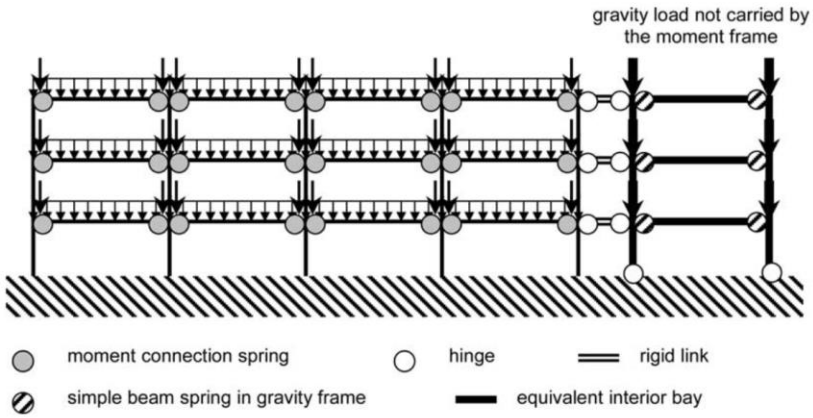

Figure 2-12: Equivalent gravity bay used to capture P-Δ effect *(Foutch & Yun, 2002)*

Two ground motion suites – one typical for California and one from near-fault activity – were applied to the building models. All ground motions were scaled to represent a 2% in 50-year hazard. The nine-story model had a median drift of approximately 3% for the typical California ground motions and a median drift of approximately 4% for the near fault ground motions. The twenty-story model experienced a median drift of approximately 3% for both ground motion suites. It was found that models incorporating the gravity framing bay were both

stiffer and stronger, exhibiting less drift demand and more drift capacity when compared to models that used leaner columns. This effect was attributed primarily to the inclusion of the gravity columns rather than the gravity connections, which tended to lose strength quickly. As shown in **Figure 2-13**, the bare-steel model M2-SC with a gravity bay had noticeably higher drift capacity than the leaner model M2-WO and was similar to the composite model M2-COMP in most cases.

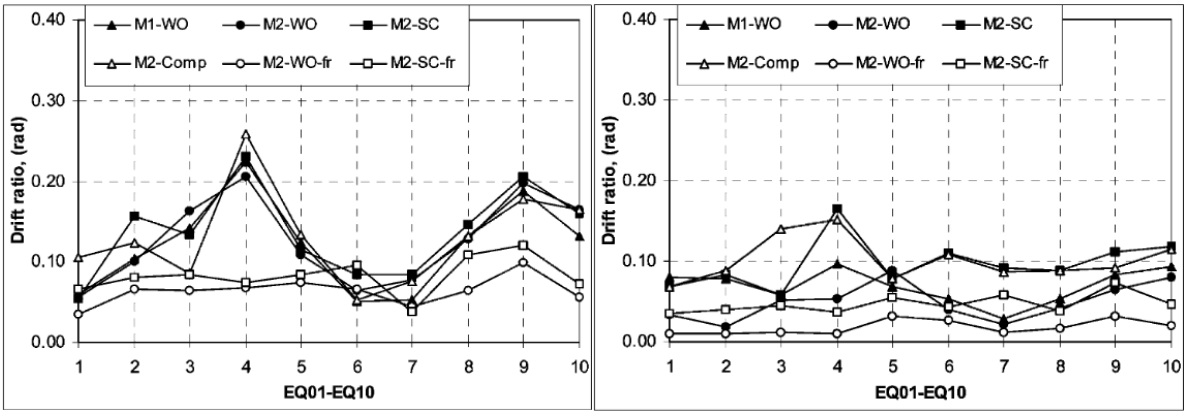

Figure 2-13: Drift capacities for 9-story (left) and 20-story (right) models subjected to typical California ground motions *(Foutch & Yun, 2002)*

Much of the literature focuses on connections as the primary source of stiffness and energy dissipation in gravity framing. This is likely due to the fact that deformations tend to be concentrated at the connections. By asserting that it may be frame action providing stiffness rather than the connections alone, this study further motivates system level testing of gravity connections.

2.3.2 Flores, Charney, & Lopez-Garcia (2014)

In response to the observed collapse performance of buildings after the 1994 Northridge earthquake, this study computationally investigated the contribution of gravity framing to the stiffness and strength of special moment frame (SMF) steel buildings. To this end, the researchers modelled a number of buildings including the gravity framing and completed a

collapse analysis according to FEMA P-695 (FEMA, 2009). The results obtained using just the SMFs were validated against previously published results before trials including the gravity framing were conducted.

The three buildings analyzed were 2-, 4-, and 8-stories and all were modelled using the plan view shown in **Figure 2-14**. The first story had a height of 4.6 meters while higher stories each had a height of 4 meters. Dead and live loading was calculated according to ASCE 7-05, consistent with prior research (ASCE, 2006). Plastic hinges were assigned to the OpenSees model at the ends of both beams and columns, as well as within the panel zones (McKenna, Fenves, & Scott, 2006). These hinges followed the general shape set forth in ASCE 41-13. (ASCE, 2013). For the validation model, a leaner column was included to capture the P-Δ effect of the gravity system. The results obtained by the researchers for both the nonlinear static pushover and collapse performance analyses were "nearly identical" to results obtained in prior research by the Applied Technology Council (ATC) in partnership with the National Institute of Standards and Technology (NIST) (NIST, 2010).

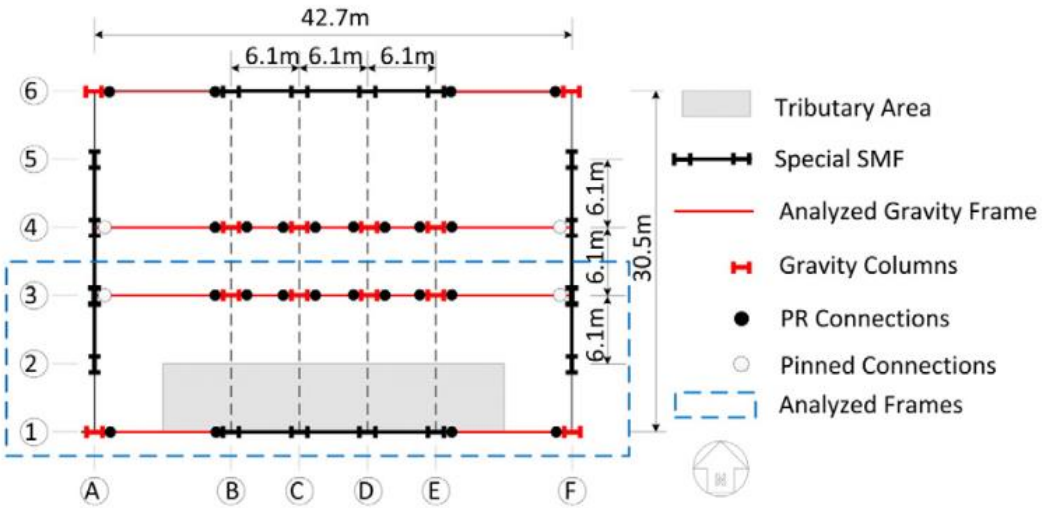

Figure 2-14: Typical plan view for SMF buildings modelled with gravity framing *(Flores, Charney, & Lopez-Garcia, 2014)*

After demonstrating the validity of the SMF model, the authors proceeded to incorporate the gravity framing into the analysis. A preliminary nonlinear static pushover analysis was conducted on the eight-story building with gravity framing using the typical assumption of pinned gravity connections. **Figure 2-15** shows the resulting pushover curves compared to the model that only incorporated the SMFs; these results indicate that the secondary stiffness of the continuous gravity framing columns in conjunction with the rigid diaphragm provides a nonnegligible amount of ductility to the structure. This observation agrees with the conclusion of Foutch & Yun (2002) that continuty of the gravity columns can provide significant stiffness without considering the stiffness of the gravity connections. The two gravity systems shown in **Figure 2-15** were designed with W14 and W18 columns as referenced in the plot legend. Strength was not significantly impacted as the connections between gravity beams and columns were assumed to be true pins. The difference in stiffness observed after 2% drift can be attributed to the stiffness of the continuous columns alone. In subsequent analyses, gravity connections were included using nonlinear springs with a moment capacity equal to 0%, 35%, 50%, and 70% of the plastic moment capacity (M_P) of the beams. These values were chosen to diversify the patterns of behavior observed in the model. A strength of 35% M_P was chosen as a lower bound given that this resistance was the minimum required to prevent the connections from yielding under gravity load. Yielding of the connections was defined as a rotation of 0.005 radians. The two higher strengths, 50% M_P and 70% M_P were chosen to represent possible stronger gravity connections despite being dubbed “somewhat unrealistic” by the authors (Flores, Charney, &

Lopez-Garcia, 2014). Trials were conducted with gravity column splices at different levels. These splices were considered pinned (zero moment capacity) to simplify the model.

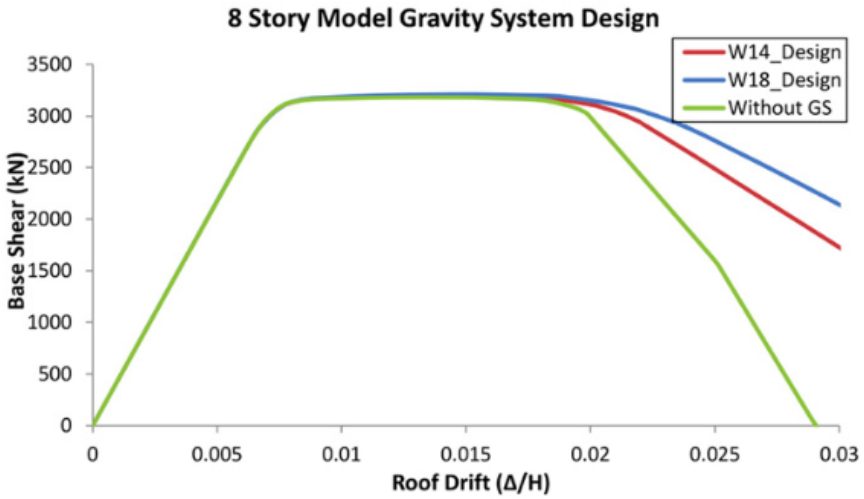

Figure 2-15: Nonlinear static pushover curves for eight story model with and without gravity framing *(Flores, Charney, & Lopez-Garcia, 2014)*

Results from the different analyses provide insight into the effects of each variable. Pushover curves for the four-story model are shown in **Figure 2-16**. The naming convention for the models is explained in **Table 2-3**. The researchers note that, with the pinned splice model, the inclusion and location of column splices significantly impacted the performance of the structure. When continuous gravity columns were provided, the gravity system provided additional ductility – as seen when contrasting 4Story+LeaningCol and 4Story+0GS_Fib in **Figure 2-16(a)** – and helped to prevent soft story behavior at the base of the building. However, when splices were included at an elevation of one third of the story height over a floor level, the gravity framing provided less secondary stiffness and much less ductility when compared to the continuous case. The decreased secondary stiffness may be observed when comparing 4Story_35GS_Fib and 4Story+35GS_Lev_Spl_Fib in **Figure 2-16(b)**. The loss of ductility may be observed in the same figure: the trial with level splices crosses below trial without gravity framing (4Story+LeaningCol) at a drift of approximately 5.5%. Column splices had the least

impact relative to the continuous column case when they were located two thirds of the story height over a floor level. This splice location was referred to as the ideal splice location. The authors noted that a model with non-ideal splices in the gravity framing still exhibited better performance than a model without any gravity framing, despite the decreased efficacy of the system. Predictably, a stronger gravity connection was found to provide more overstrength in the system. All things equal, a building with stronger gravity connections was found to exhibit less ductility and a shorter period of vibration than a building modelled with weaker gravity connections.

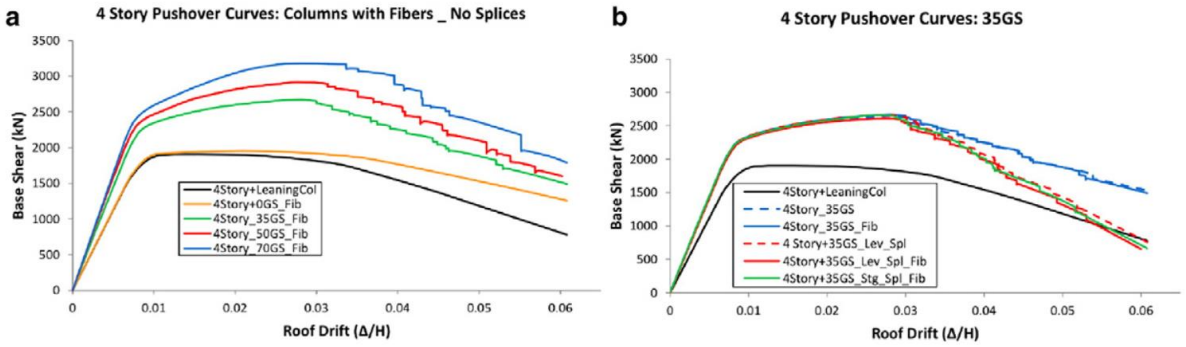

Figure 2-16: Nonlinear static pushover curves for four story models *(Flores, Charney, & Lopez-Garcia, 2014)*

Table 2-3: Naming convention for models in Flores, Charney, & Lopez-Garcia (2014)

Name Component	Meaning
#Story (i.e. 4Story)	Height of model
+LeaningCol	P-Δ effect included using leaning column, no gravity framing included
_##GS (i.e. 35GS)	Capacity of gravity connections as ## percentage of beam M_p
_Fib	Gravity columns modelled using nonlinear fiber models
_Lev_Spl	Splices included in columns at one elevation
_Stg_Spl	Splices included in columns at staggered elevation

Flores, Charney, & Lopez-Garcia's analytical work lead to the conclusion that gravity framing can substantially impact the behavior of a structure. The interaction between gravity connections, continuous columns, and column splices in this research implies that no one part of a gravity framing element can fully characterize the behavior of the system. For that reason,

system-level testing is required to identify and quantify the contributions of different mechanisms to the overall performance of gravity framing.

2.4 Literature Summary

This chapter presented research from the current body of knowledge that supported the development of the specimen described in this thesis. Three research categories were explored in this review: experimental tests of bare-steel connections, experimental tests of composite connections, and computational analysis of the effects of gravity framing on seismic response. Experimental tests of bare-steel connections presented in Shen and Astaneh-Asl (1999) provided an understanding of the double-angle shear connections that are the subject of this thesis. Shen and Astaneh-Asl (1999) described the primary failure mechanism of double-angle shear connections – fracture at the toe of the angles – and the behavior of the connections as they were loaded. The experimental study of composite connections presented in Leon (1990) described the same failure mechanisms observed in Shen and Astaneh-Asl (1999). Leon also documented the stiffness loss in the system due to bolt hole deformation. The research presented in Donahue (2019) provided a basis for the research presented in this thesis. Donahue's crucifom tests of gravity framing connections were extrapolated into the full-scale frame described in Chapter 3. Computational analysis of systems including gravity framing as presented in Foutch and Yun (2002) and Flores, Charney, and Lopez-Garcia (2014) indicated that gravity framing provides nonnegligable stiffness and strength to structural systems, motivating additional system-level testing.

3 Experimental Setup – Bare-Steel Frame

A rendering of the two-bay by three-bay bare-steel specimen is shown in **Figure 3-1**. The structural plans for the specimen are provided in Appendix A. Member sizes and connections were designed to match the cruciform subassembly tested by Donahue (2019). Donahue, in turn, based the design of his specimen on the SAC model building presented in FEMA-355C (FEMA, 2000). The full-scale specimen mimics the behavior of a single floor of a building, with test columns representing a half story above and a half story below the floor.

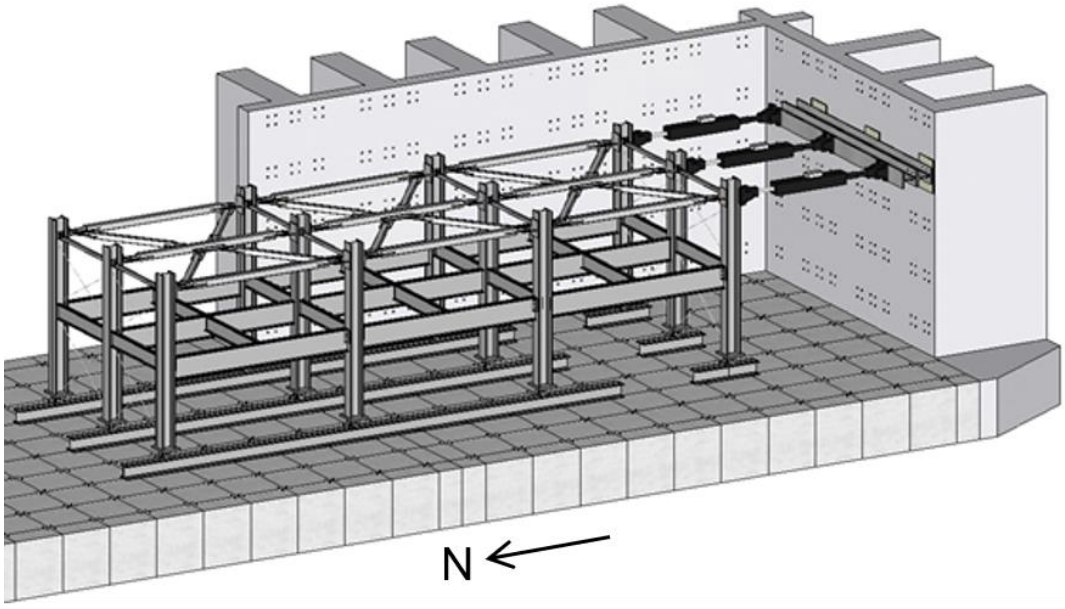

Figure 3-1: 3-D render of the full-scale bare-steel specimen

Bays were sized 16 feet parallel to the axis of motion (North-South, the strong direction) and 8 feet perpendicular to the axis of motion (East-West, the weak direction). W12x96 columns were used in the structure. On the first floor, W21x55 girders spanned between the columns in the strong direction and W14x22 infill beams spanned between the columns and between the midspan of the girders in the weak direction. An essentially rigid truss diaphragm consisting of HSS members was constructed at the tops of the columns. The focus of the

experiment was the lateral load-resisting contribution of the first-floor gravity framing with a special emphasis on the girder-column connections. The specific assembly and detailing of each structural component are discussed in this chapter, starting with the foundation and working up to the top diaphram.

3.1 Foundation

3.1.1 Base Beams

W12x65 beams were anchored to the strong floor along column-lines A, B, and C in the North-South direction to provide a mounting surface for the column bases. These beams, shown at the bottom of the elevation in **Figure 3-2**, were sized to accommodate the expected vertical forces during testing and to transmit the base shear to the strong floor. A continuous beam anchored the columns on lines 1, 2, and 3 while a shorter beam anchored the columns on line 4. This division resulted from length limitations from the steel manufacturer. Pre-tensioned rods were installed at each bolt group in the strong floor along the length of the frame. A coefficient of friction of 0.2 was assumed between the bottom flange of the base beams and the concrete of the strong floor to determine the pretension force. Each rod was tensioned to develop a normal force between the strong floor and the base beam that resulted in static frictional resistance exceeding the maximum expected base shear during testing. Shear demands were assumed to be uniformly distributed over the length of the structure. The total normal force provided was 400 kips on the short beam and 880 kips on the long beam, resulting in a total expected slip resistance of 256 kips. This resistance exceeded the maximum base shear of 226 kips determined in the pushover analysis presented in Hernandez (2020).

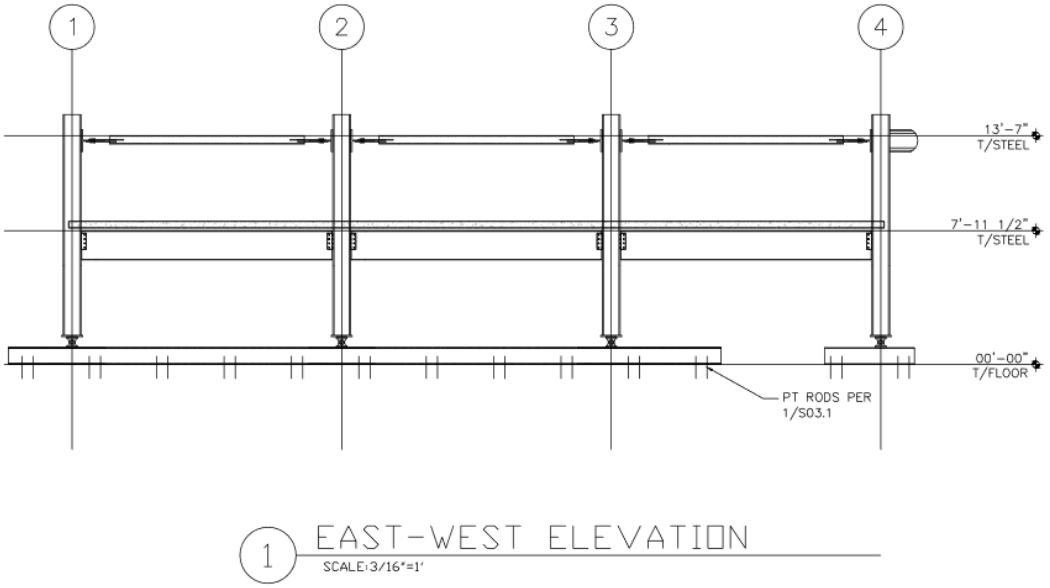

Figure 3-2: Elevation of frame specimen (1/S2.2)

3.1.2 Clevises

The bottoms of the columns were constrained by clevises attached to the base beams. The clevises, manufactured by Miller Fluid Power, consisted of a clevis bracket, a pin, and an eye bracket with model numbers 0960160200, 0692150000, and 0959810200, respectively. The strength of the clevis assembly was checked in Hernandez (2020) and exceeded the expected demand at each column base. Pretensioned 1" diameter A325 bolts connected the clevis bracket to the base beam and the eye bracket to the column baseplate. The tension in these bolts prevented differential motion between the faying surfaces at the top and bottom of each clevis during loading. Clevises were used because they present negligible moment resistance, enforcing the assumed zero-moment behavior at the half-story level. The baseplate-clevis-base beam detail is depicted in **Figure 3-3**. A photograph of the clevis connecting the base beam and the base plate is shown in **Figure 3-4**.

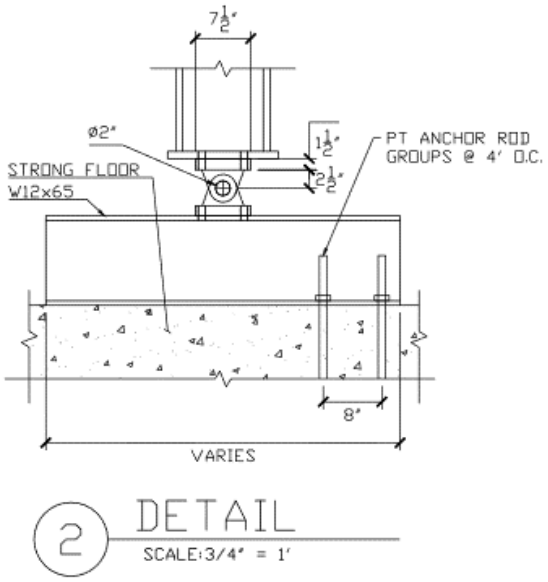

Figure 3-3: Column base connection detail (2/S3.1)

Figure 3-4: Photograph depicting clevis attached to base beam and base plate

3.1.3 Columns and Out-of-Plane Bracing

Columns were W12x96 sections oriented with the strong axis in the North-South direction, which was the direction of loading. The W12x96 section was chosen to match the work of Donahue (2019). Strong-axis lateral resistance was provided exclusively by the gravity framing; there was no lateral system present in the North-South direction (see **Figure 3-2**). In the weak axis, cross bracing was provided using 5/8" diameter threaded rods at the northernmost and southernmost columnlines. Although significant out-of-plane forces and deformations are not expected, bracing was provided for stability. **Figure 3-5** shows an elevation of a typical braced columnline. The bracing rods were anchored in the column webs using short slotted holes with nuts on either side of the web. Hill-side washers were used to accommodate the inclination in the bracing rods. See **Figure 3-6** for the typical out-of-plane bracing details used at these locations.

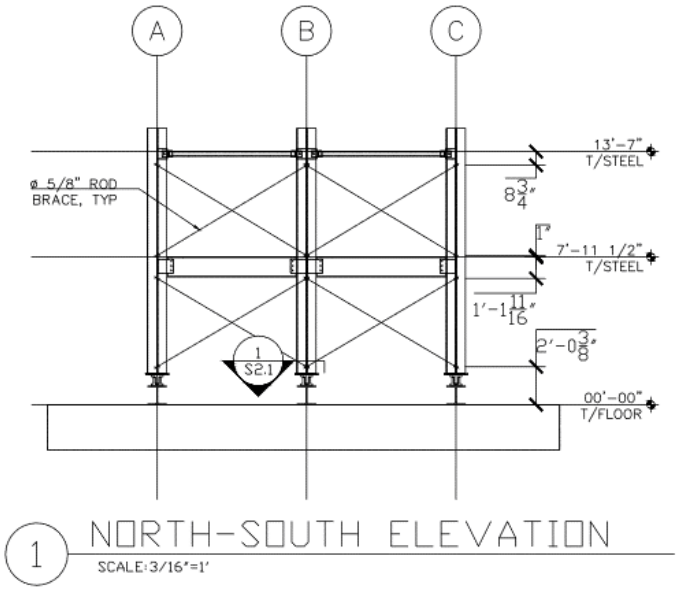

Figure 3-5: Elevation showing out-of-plane bracing scheme (1/S2.1)

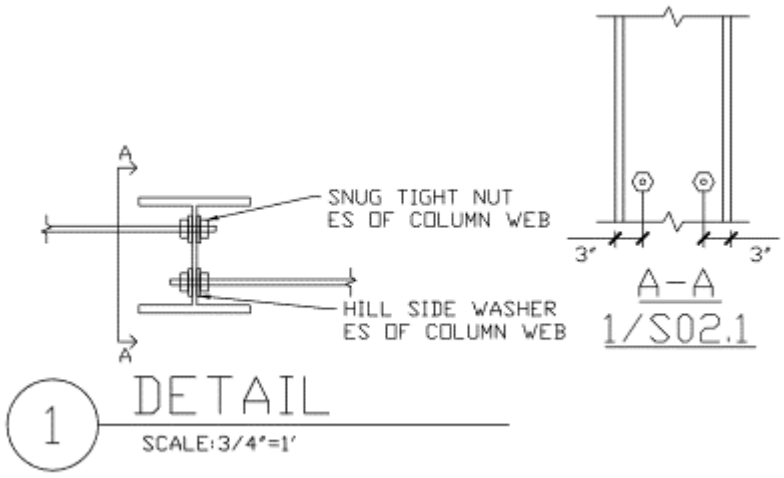

Figure 3-6: Out-of-plane bracing details (1/S2.1)

3.2 First Story

The first story of the test specimen contained the gravity framing that is the focus of this research. Members on this floor were sized to match Donahue (2019), who in turn based his design on the SAC Model Building presented in FEMA 355 (2000). The gravity connections of interest were located on this story between the columns and the North-South girders. Additional connections were developed for the infill beams that ran in the East-West direction. Connection details for each component are discussed in the following sections.

3.2.1 Girder-Column Connection

A schematic of a typical girder-column double angle connection is shown in **Figure 3-7**. **Figure 3-8** shows a photograph of this connection. The connection consisted of two L4x3-1/2x5/16 sections oriented with their long legs on the column and their short legs on either side of the web of the W21x55 girder. Standard holes for 3/4" diameter A325 bolts were spaced at 3" on center. Long-slotted holes were provided in the long legs for ease of construction. A 1/2" gap was provided between the end of the girders and the flange of the column. During testing, it is expected that this gap will close at high drifts and the compression flange of the girder will

contact the column. Per the recommendation of the project's industry advisory committee, bolts passing through the girder web were pretensioned. In a building construction application, it is common to attach the angles to the girder prior to shipping. Fabricators generally fully tension the bolts to prevent loosening as the girder is handled and installed. Tension was assured using direct tension indicators (DTIs - Applied Bolting squirter washers). As suggested by the manufacturer, the installation process was validated on a Skidmore-Wilhelm hydraulic tension calibrator. Note that the connection was originally designed as a bearing type connection. Due to the large normal force provided by the pretensioned bolts, it is expected that these connections will behave as slip-critical connections at low drifts. The deformation at which the connection will reseat and engage the bolts in shear will be recorded as part of the experimental program.

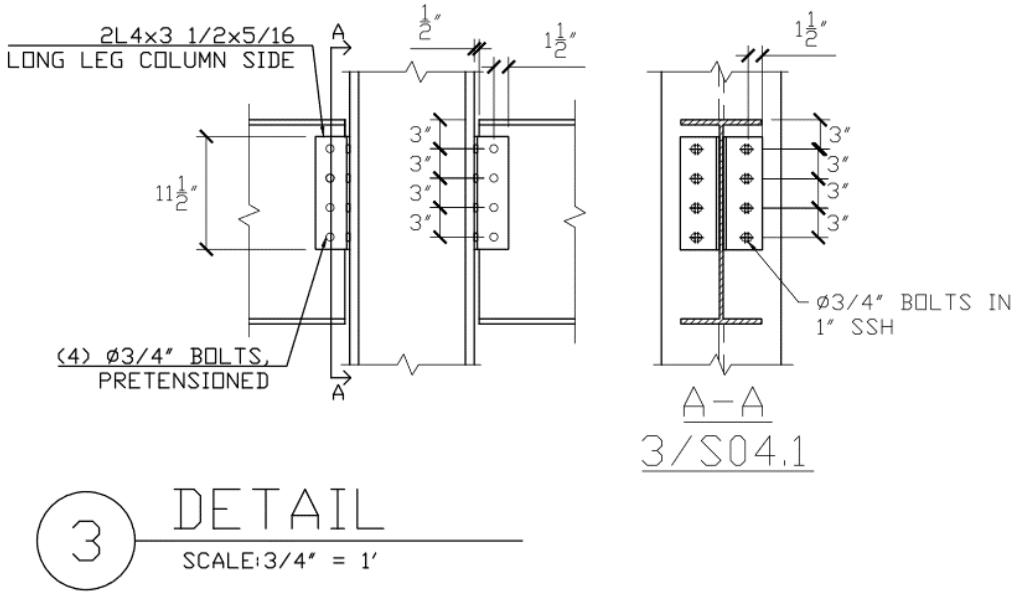

Figure 3-7: Typical girder-column connection of interest (3/S4.1)

Figure 3-8: Photograph of double-angle connection on girder

3.2.2 Infill-Column Connection

For infill beams spanning between the columns in the East-West direction, a simple shear tab connection was used. The tab was welded to the column web and three 3/4" diameter bolts were connected to the web of the beam. A drawing of this connection is provided in **Figure 3-9**. A photograph of this connection is shown in **Figure 3-10**.

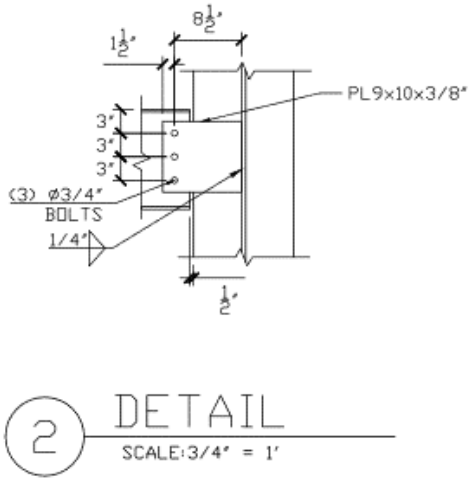

Figure 3-9: Typical shear tab connection for infill beams (2/S4.1)

Figure 3-10: Photograph of shear tab on column-spanning infill beam

3.2.3 Infill-Girder Connection

Intermediate girder-supported infill beams utilized a double angle connection similar to the gravity connection for the girders that spanned in the strong direction. This connection is shown in **Figure 3-11**. The same angle section used in the girder-column connection, a L4x3-1/2x5/16, was used in these beam-girder connections. A 1/2" cutback was provided at these fixtures as in the primary gravity connections. Four holes were provided for the three-bolt connection to facilitate the offset configuration shown in **Figure 3-11**. This practice allowed at least two bolts to remain installed on each infill beam during erection as the connection on the opposite side of the girder web is installed.

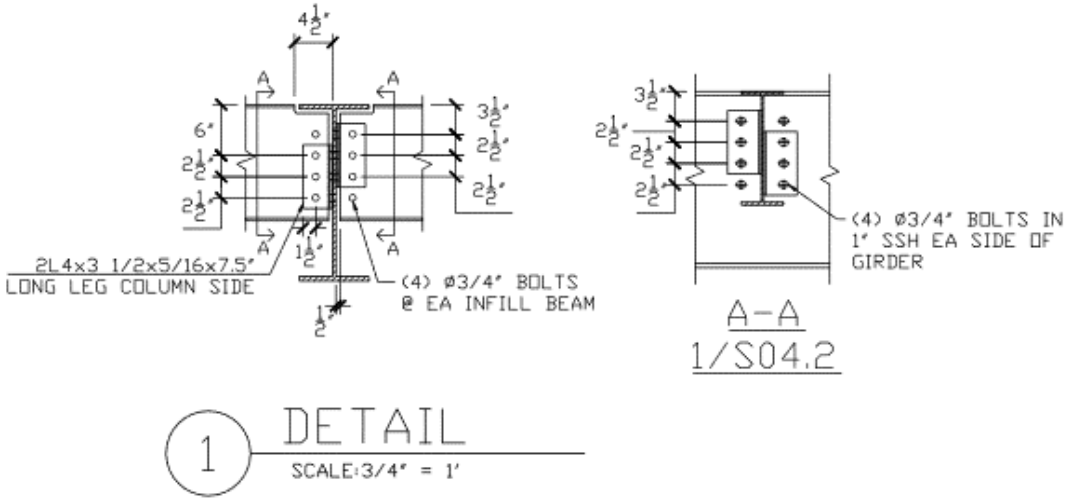

Figure 3-11: Typical double angle connection between girder and infill beams (1/S4.2)

3.3 Top Diaphragm

The top diaphragm of the test specimen was designed according to the demands presented in Hernandez (2020). The design presented herein is a modification of the work shown in Saavedra (2020). The purpose of the top diaphragm in the specimen was to transimit the forces from the actuators at the south end of the specimen to each column while preventing lateral translation between the tops of the columns. As shown in **Figure 3-12**, HSS 6x6x1/2 members

were used in the North-South direction while HSS 5x5x1/4 sections were used on the diagonals. HSS 3x3x1/4 sections were provided in the East-West direction to distribute out-of-plane forces. These sections were sized in Saavedra (2020). Connection details for the top diaphragm are provided in the following sections.

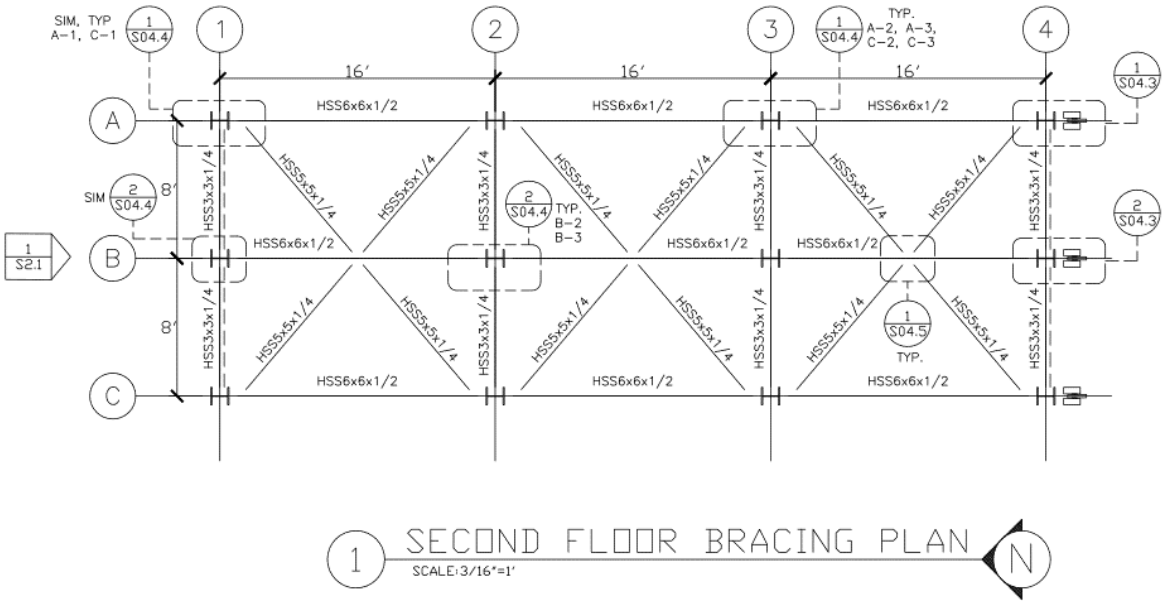

Figure 3-12: Top diaphragm plan (1/S1.2)

3.3.1 HSS 3x3x1/4 – Column Connection

The out-of-plane HSS members were attached to the columns with a WT section. A one-foot length of WT6x25 was bolted to the column web as depicted in **Figure 3-13 (Right)**. Knife plates were welded into slots at each end of the HSS sections as shown in **Figure 3-13 (Left)**. The HSS members were then installed by bolting the knife plates to the webs of the WT sections. The use of a knife plate welded into a slot was typical for all HSS members in the top diaphragm. **Figure 3-14** shows the shop drawing used in the manufacture of the HSS 3x3x1/4 members for the top diaphragm. A photograph of connection is shown in **Figure 3-15**. While member and plate sizes were variable, this same basic detail was used for all HSS sections.

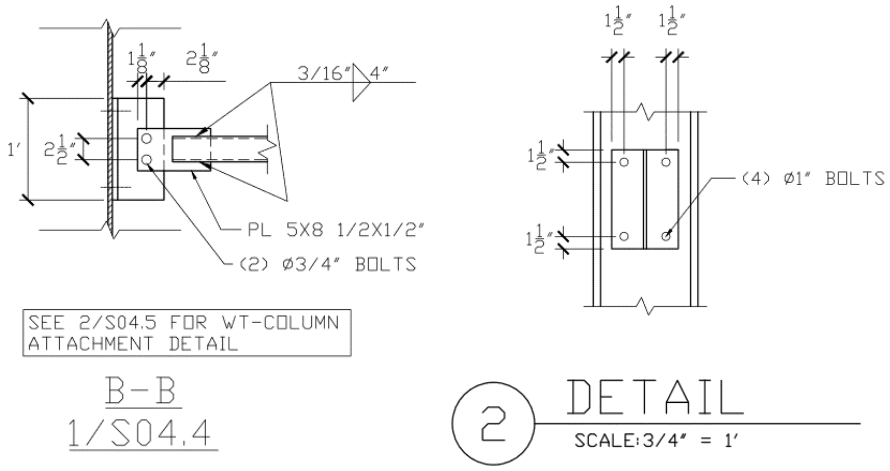

Figure 3-13: (Left) HSS 3x3x1/4-WT6x25 connection detail (B-B 1/S04.4); (Right) WT6x25-Column connection detail (2/S04.5)

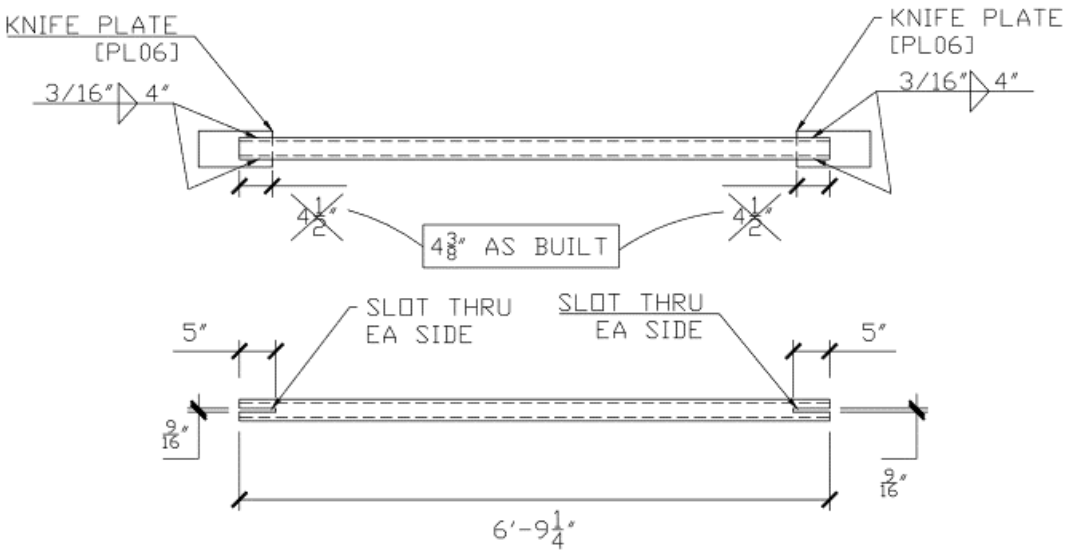

Figure 3-14: Shop drawing showing slot and knife plate assembly for HSS 3x3x1/4

Figure 3-15: Photograph of HSS 3x3x1/4 framing into WT section in column web

3.3.2 HSS 5x5x1/4 – HSS 6x6x1/2 Midspan Connection

The diagonal HSS 5x5x1/4 sections were connected to the midspan of the HSS 6x6x1/2 sections via a gusset plate. This connection, shown in **Figure 3-16**, utilized the same slot and knife plate assembly discussed previously. The knife plates were bolted to a 1/2" thick gusset plate that was welded at mid-height of the HSS 6x6x1/2 section. The A325 bolts, 1 1/4" in diameter, were pretensioned such that the connection transmits the anticipated experimental forces without slip. As with pretensioned connections on the first story, squirter washers were used to ensure the proper tension was provided.

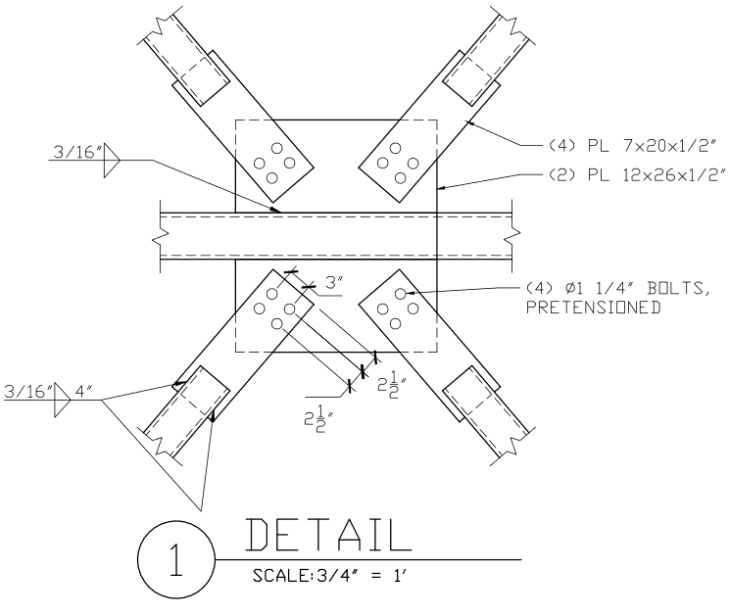

Figure 3-16: Gusset plate detail for HSS 5x5x1/4-HSS 6x6x1/2 connection (1/S4.5)

3.3.3 T-Stub Connection

The connection used in the North-South direction at the top diaphragm was referred to as the "T-stub connection." The flange of a WT section was attached to the vertical flange of the column with the WT stem in the horizontal plane. The motivation for this vertical to horizontal connection was to satisfy the assumption of negligible bending moment at the mid-height of a story. As with the clevis connection at the base of the structure, the T-stub connection was devised as a connection that provides minimal moment resistance. In theory, the top diaphragm remains relatively horizontal within each bay even as the columns tilt, because the predominant deformations are concentrated in the plate-like T-stem.

Several variants of the T-stub connection were constructed at different locations on the top diaphragm. The simplest of these connections, shown at column-line B in **Figure 3-17**, consisted of the HSS 6x6x1/2 knife plate bolted directly to the T-stem. Pretensioned 1 1/4" bolts were used in the horizontal plane. The T-stub was attached to the column per the drawings in **Figure 3-18**.

At most locations on the top diaphragm, the T-stub was simply bolted to the flange of the column as shown in **Figure 3-18 (Left)**. The column-line to which the actuators were attached used a larger T-stub to accommodate the hole pattern on the actuator head. As shown in **Figure 3-18 (Right)**, the larger T-stub was bolted to the column flange and threaded rods were attached from the actuator head through T-stub flange. This assembly required coping the flanges of the column to provide clearance for the threaded rods. Note that 1/2" stiffeners were provided in the column above the top bolt holes and below the bottom bolt holes at each T-stub connection. These stiffeners were provided to prevent web crippling and local buckling from the large actuator forces applied to the tops of the columns.

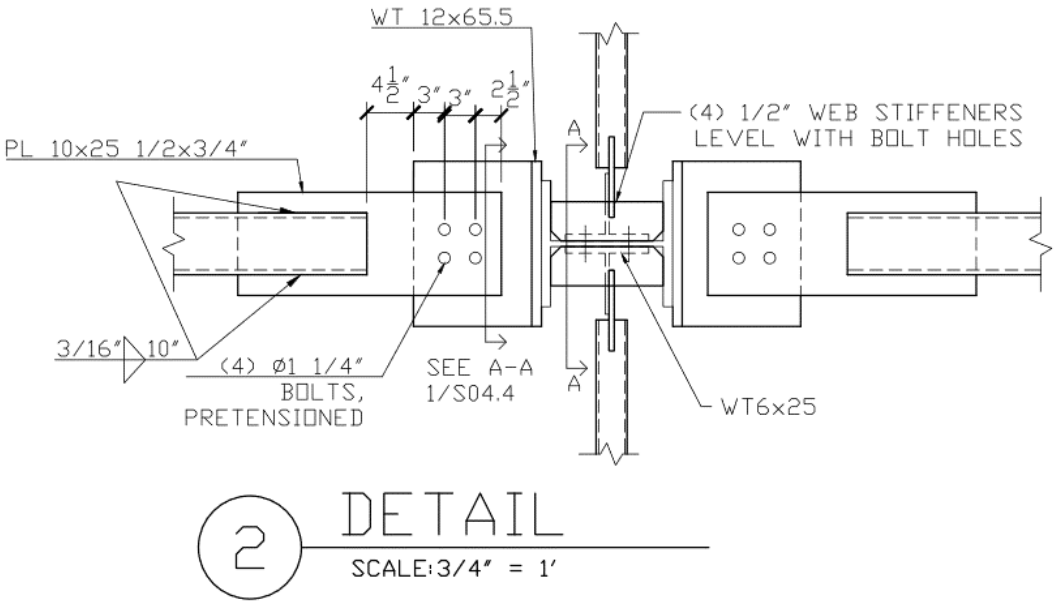

Figure 3-17: Typical T-stub connection at column-line B (2/S4.4)

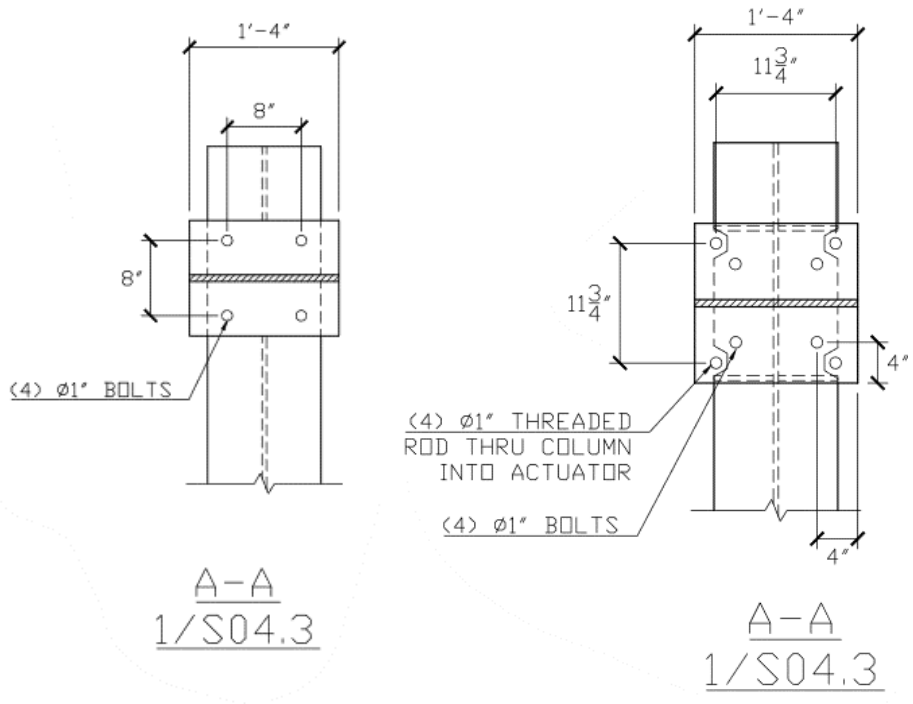

Figure 3-18: (Left) Typical T-stub to column connection (A-A /S4.4); (Right) T-stub to column connection at the actuator (A-A 1/S04.3)

At column-lines A and C, the diagonal HSS 5x5x1/4 knife plate framed in above the T-stem and under the HSS 6x6x1/2 knife plate as shown in **Figure 3-19**. As mentioned previously, the design intent was that the members of the top diaphragm remain relatively horizontal regardless of the inclination at the top of the column. Ideally, the T-stub experiences the majority of the deformation rather than the knife plate as the WT section is easier to replace in subsequent tests. By locating the diagonal knife plate between the T-stem and the HSS 6x6x1/2 knife plate, contact between the edge of the T-stem and the HSS 6x6x1/2 knife plate was avoided. The design intent is that bearing of the T-stem edge against the knife plate develops a force couple with the bolts as the structure deflects, potentially inducing additional bending stresses in the knife plate. The diagonal knife plate was coped at the column-facing corner to provide a "protected zone" on the T-stem where bending can occur. A photograph of a typical T-stub

connection, showing both the horizontal connection as well as the connection between the T-stub and the column flange, is shown in **Figure 3-20**.

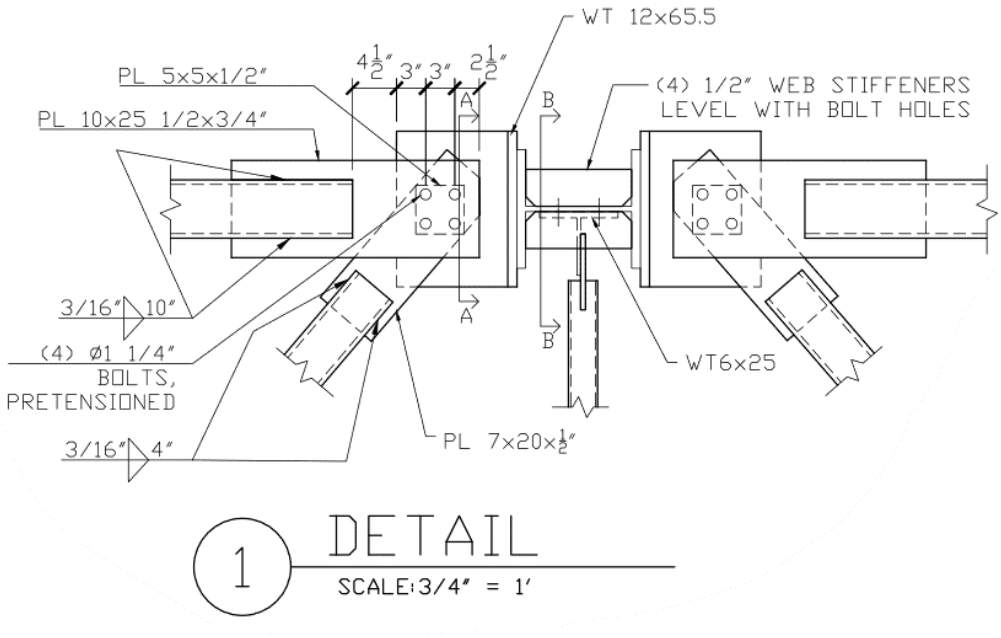

Figure 3-19: Typical T-stub connection at column-lines A and C (1/S4.4)

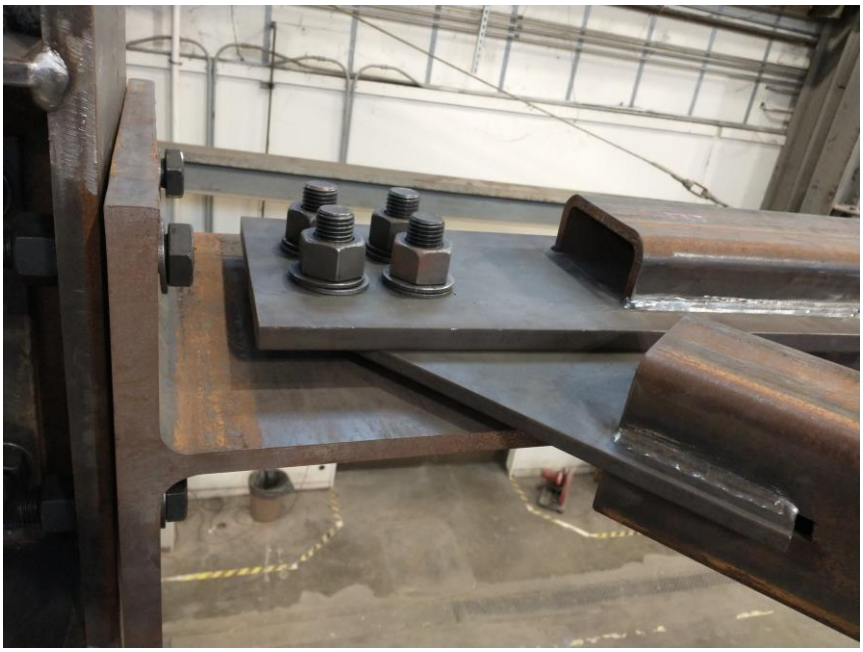

Figure 3-20: Photograph of typical T-stub connection

An additional 1/2" plate was inserted between the HSS 5x5x1/4 knife plate and the T-stem to ensure the HSS 5x5x1/4 sections remained level. This was necessary due to the discrepancy between the horizontal T-stub connections at column-line B and the two outer column-lines A and C. At column-line B, the knife plate for the HSS 6x6x1/2 rested directly on the horizontal T-stem. At the outer two column-lines, the knife plate for the HSS 5x5x1/4 rested directly on the horizontal T-stem, below the HSS 6x6x1/2 knife plate. Therefore, the outer knife plates on the HSS 5x5x1/4 were lower than the inner knife plates by approximately half an inch. Providing a plate to make up this difference kept the diagonal HSS members level.

Two concerns were raised about the T-stub connection prior to erection. First, it was unknown how much moment the connection assembly will resist during testing. Second, the distribution of deformations between the knife plate and the T-stem is unknown. While the efforts described previously were suggested to encourage deformation in the T-stem, the actual behavior of the assembly is uncertain. The former problem – ascertaining the moment resistance of the connection – was handled by including instrumentation on the bare-steel columns that allows the moment at the top of the column to be measured. The latter problem was addressed with the computational and experimental procedures described in the following chapter.

3.4 Summary

The geometry of the bare-steel test specimen was detailed in this chapter. Both the details of interest and the details pertaining to the test setup were explained. The two-bay by three-bay specimen was constructed to determine the behavior of gravity framing under lateral loading. Bolted double-angle connections were used to connect the girders to the columns at the first floor. These connections will be a primary subject of scrutiny as the moment resistance of such connections may provide nonnegligible lateral resistance to the structure as a whole. The

specimen was designed to represent one floor of gravity framing with columns spanning a half story above and below. A point of zero moment was assumed to occur at midstory. To enforce this assumed boundary condition, the bases of the columns were attached to the strong floor using clevises. The tops of the columns were attached to a truss diaphragm to distribute loading from the hydraulic actuators. This diaphragm was expected to remain horizontal as the system swayed. A T-stub connection was detailed to attach the column tops to the diaphragm. The ability of the T-stub to accommodate rotation between the column tops and the diaphragm was a concern, so a component test of the connection was conducted as outlined in the next chapter.

4 T-STUB CONNECTION TEST

The T-stub connection that joined the rigid diaphragm and the tops of the columns in the full-scale specimen was the subject of additional scrutiny due to its uncertain bending behavior. Ideally, the top truss diaphragm will remain horizontal throughout the experiment. Therefore, the T-stub connection must accommodate the relative rotation of the horizontal diaphragm and the inclined columns. To minimize inelastic deformation in the members of the lateral truss, rotations must be concentrated in the stem of the T-stub. In this deformation scenario, the members of the top diaphragm can be reused in subsequent experiments and the only component that needs to be replaced is the T-stub. Therefore, one of the primary goals of the tests discussed in this chapter is to simulate the inelastic deformation that are likely to occur when the full-scale frame is subjected the maximum anticipated drift ratios to determine if permanent deformations in the top truss members stay within tolerable levels that will permit the reuse in subsequent experiments.

Simple calculations to predict the bending profile of the T-stub connection suggested that deformations are likely to be shared between the knife plate and the web of the T-stub, which is referred to in this chapter as the T-stem. Both the knife plate and the T-stem cross-sections were idealized as rectangular sections bending about their weak axis. The knife plate had a moment of inertia of $0.35\ in^4$, while the thickest T-stem – the WT16.5x100.5 used at the actuator column-line – had a moment of inertia of $0.50\ in^4$. These two stiffness values were similar in magnitude, indicating that both members were likely to deflect under the uniform-moment load state anticipated at the top truss. The researchers were concerned that the greater stiffness of the T-stem might lead to excessive concentrated permanent deformations in the knife plate, thereby compromising the ability to reuse the top truss members in subsequent tests.

The alternate knife-plate detail depicted in **Figure 4-1** was devised to encourage deformation in the more easily replaceable T-stub. Rather than a section of rolled plate, it was proposed that a channel be inserted into the slot at the end of the HSS 6x6x1/2 member. The flanges of the channel provide a bending stiffness several orders of magnitude greater than the bending stiffness of the T-stem, thus concentrating bending deformations in the T-stem. A C12x25 was chosen to replace the knife plate. This selection was motivated primarily by geometry rather than stiffness considerations. In this application, the necessary channel geometry requires a flat portion of the web to fit the HSS 6x6x1/2 between the flanges, and the web thickness must meet or exceed the thickness of the knife plate so that the bolted connection can still maintain its integrity under bearing. The length of the channel was dictated by the welding requirements. Since the flanges of the channel obstructed the interface of the channel and the

HSS 6x6x1/2 at the top of the slot, all welds had to be located at the bottom of the slot. This increased the length of weld required from 10" to 15".

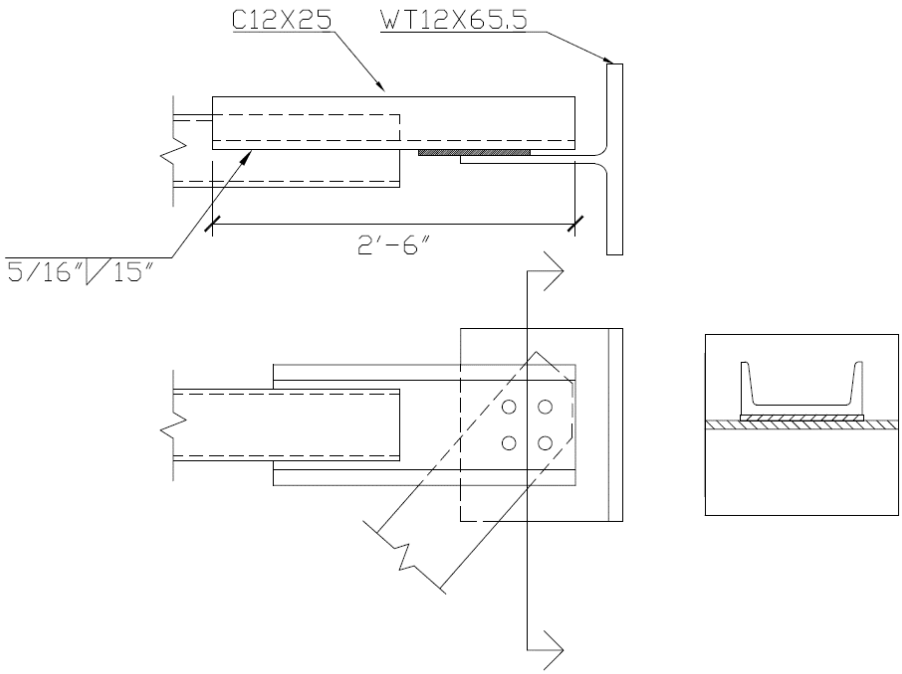

Figure 4-1: Alternate knife plate detail using a length of channel

The original and alternate knife plate details were compared using ANSYS Workbench as described in the following section (ANSYS, Inc., 2019). An experimental test setup was devised to verify the behavior of the connection. The proceedings of this experiment are described in Section 4.2. Results and recommendations are presented in Section 4.3.

4.1 Computational Analysis

Both the original and alternate knife plate details were analyzed in ANSYS Workbench. The members were modelled using 3D solid elements due to the complexity of the connection; the assembly could not reasonably be reduced to a plane section without losing fidelity. Shell elements were not used due to the presence of fillets at the corners of the rolled shapes. **Figure 4-2** shows the model of the original knife plate detail, while **Figure 4-3** shows the model of the

alternate knife plate detail. These models took advantage of the symmetry of the connection. This strategy allowed a higher-fidelity mesh to be used without incurring the associated computational cost.

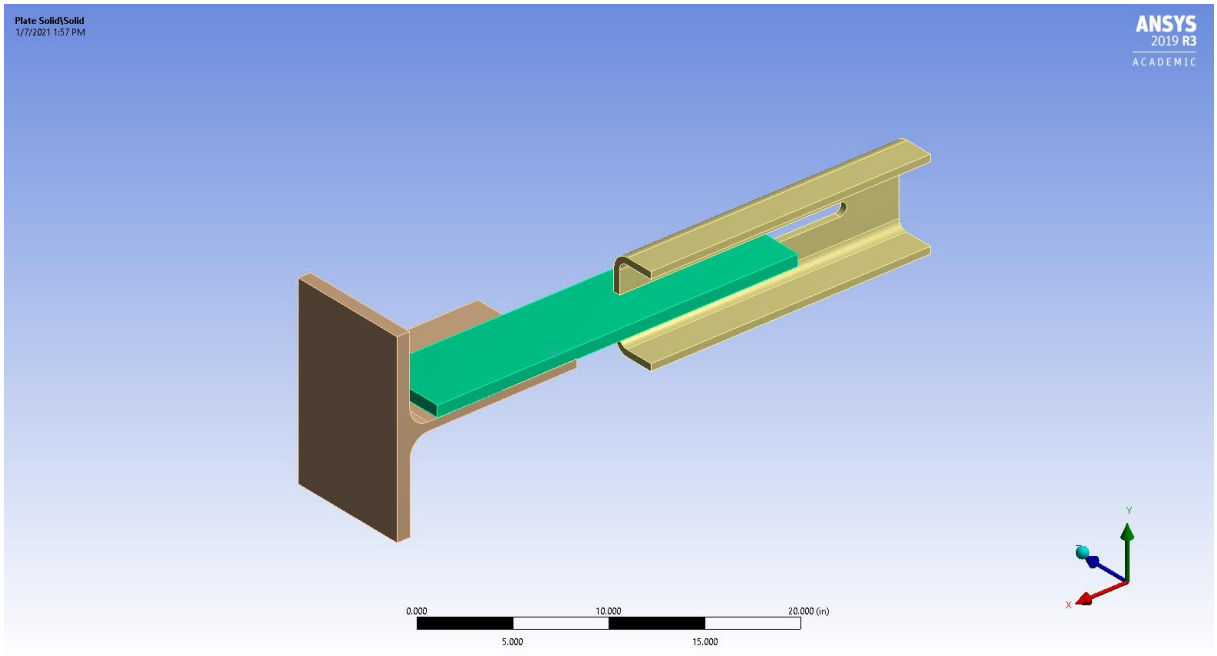

Figure 4-2: ANSYS model of the original knife plate detail

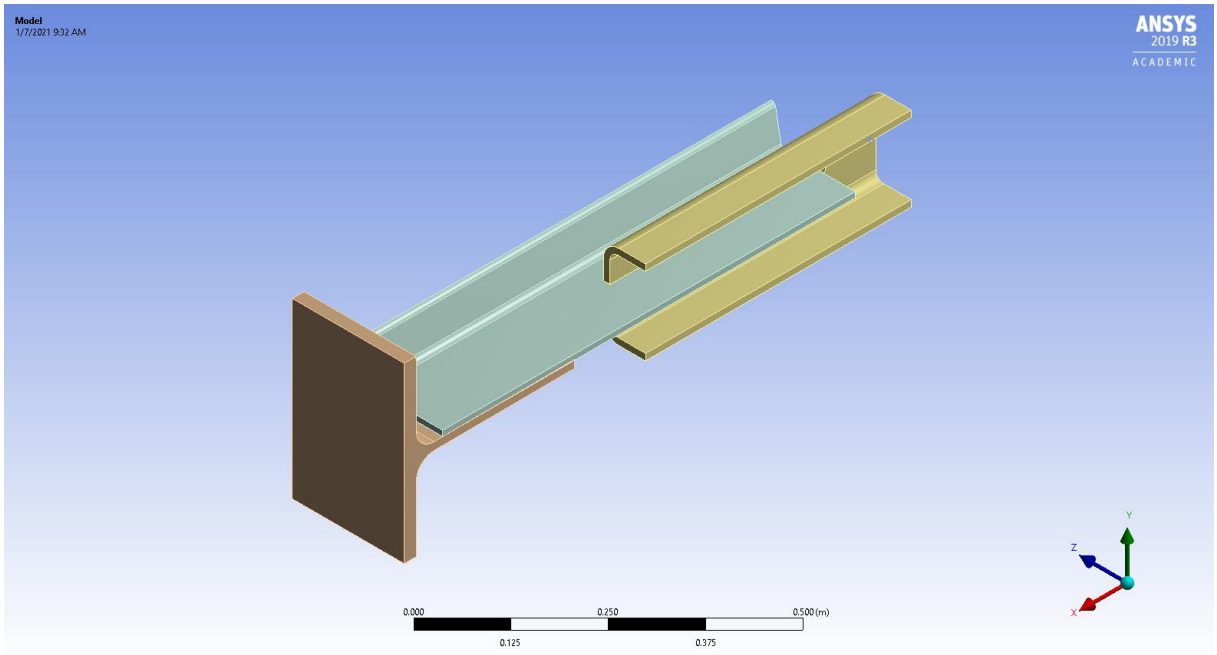

Figure 4-3: ANSYS model of the alternate knife plate detail

Elastic-perfectly plastic material models were used for all members. The HSS and WT sections had a material yield strength of $50\ ksi$, consistent with the nominal yield strength of the actual members. Both the original and the alternate knife plates were modelled with a yield strength of $36\ ksi$. While more complex material models exist that better capture the nonlinearity of steel, the elastic-perfectly plastic material model was chosen for its simplicity. The computational portion of this analysis was conducted as a preliminary check to determine if the alternate detail was viable. It was decided that the inclusion of an advanced material model would not appreciably contribute to this goal.

Each member was meshed using quadratic tetrahedral elements. By default, the elements were sized at 0.75". **Figure 4-4** shows the mesh of the model including refinements on the thin bending elements and on the contact surface at the inside of the HSS slot. All mesh refinements decreased the size of the elements to one half of the default size. The knife plate, the T-stem, and the inside surface of the HSS slot were refined. Refinements were applied primarily to ensure that there were two layers of elements in the bending members, the knife plate and the T-stem. Additionally, mesh refinement aided in the definition and convergence of the contact interactions between the HSS and the knife plate and the knife plate and the T-stem.

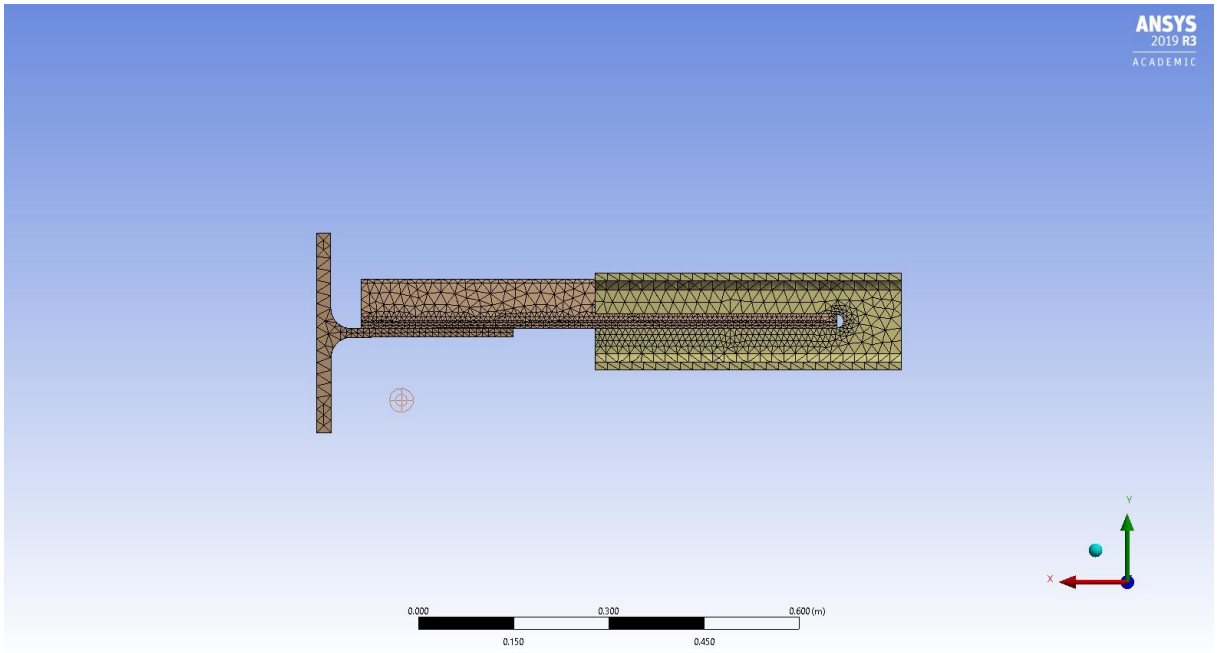

Figure 4-4: Mesh of T-stub specimen in ANSYS model viewed on the symmetry plane

Boundary conditions are shown in **Figure 4-5** and **Figure 4-6** on the alternate knife plate model. Identical boundary conditions were used in the original knife plate model. Displacement in the Z direction and rotation about the X-axis were constrained on all faces along the symmetry plane. Symmetry boundary conditions are marked "A" in **Figure 4-5**. To avoid rigid body translation of the assembly, the bottom edge of the WT flange – marked "B" in **Figure 4-5** – was restrained in the X- and Y-axes. Rotation was prevented about the Z-axis on the outer face of the HSS member as marked by "C" in **Figure 4-5** to simulate the expected behavior of the top diaphragm. As mentioned previously, it is expected that the members comprising the diaphragm will remain horizontal as the columns sidesway. Contact pair "B" in **Figure 4-6** shows the bottom plane of the knife plate rigidly attached to the bottom of the slot in the HSS section to simulate the behavior of the weld at that location. The same rigid connection was used for contact pair "A" in **Figure 4-6** to attach the bottom of the knife plate to the top of the T-stem. This boundary condition was a simplification of the pretensioned bolted connection between the

knife plate and the T-stem. Note that the diagonal knife plate was not included between the knife plate and the T-stem in this model. This omission was meant to simplify the analysis.

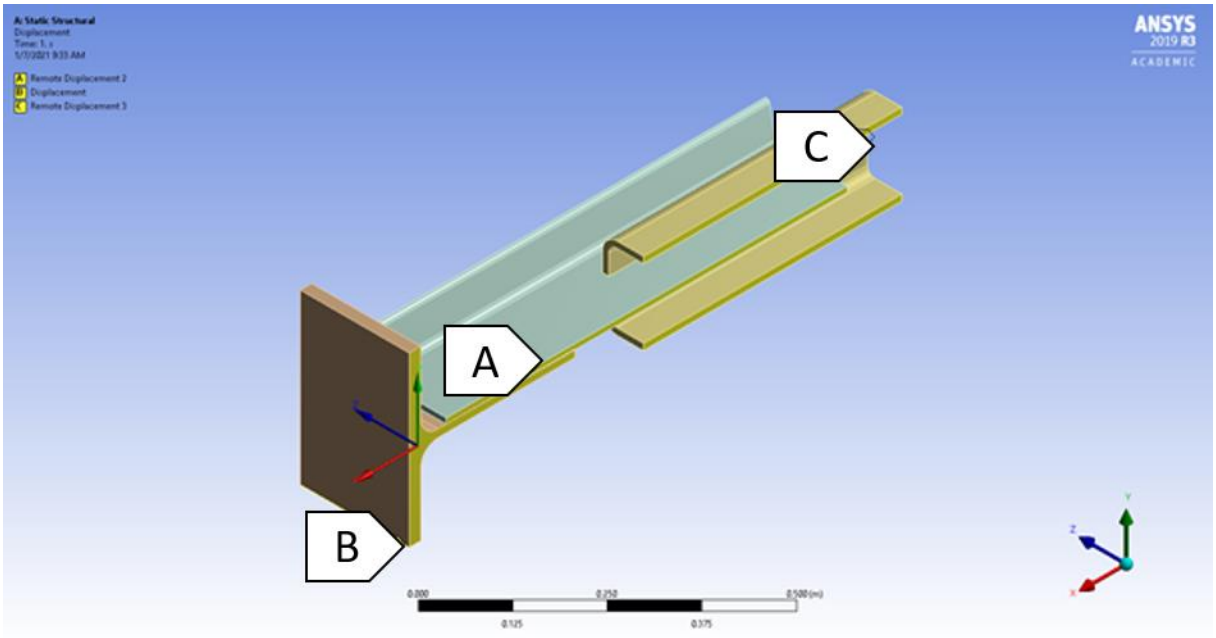

Figure 4-5: Typical boundary conditions for T-stub ANSYS model

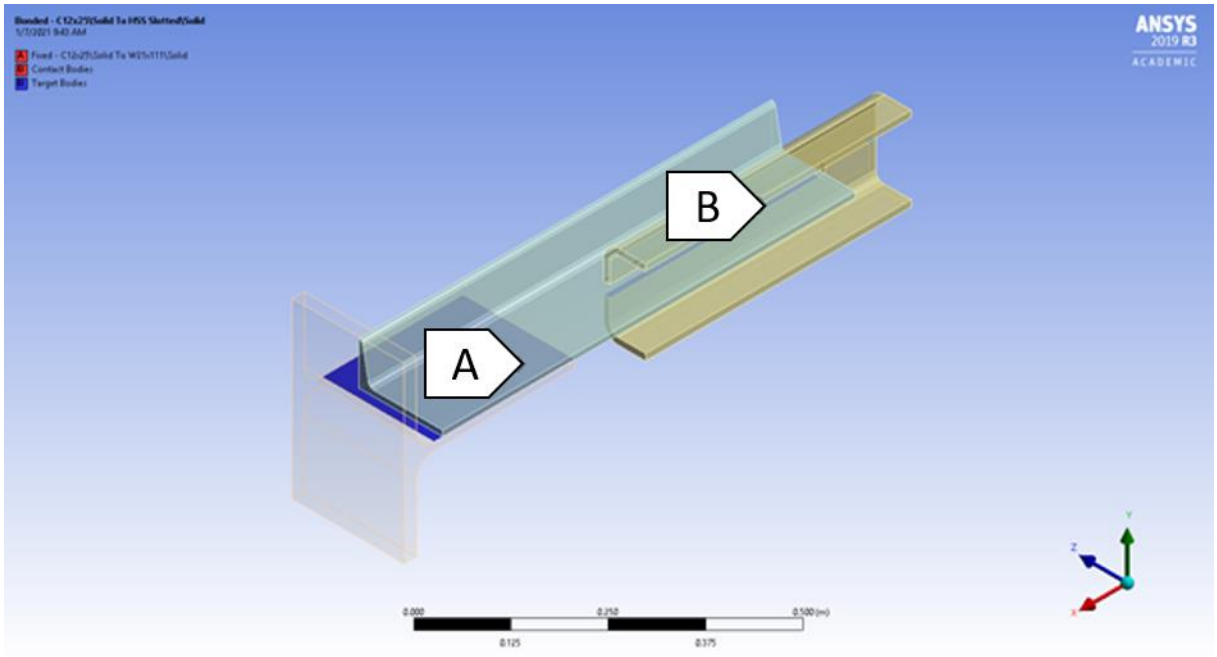

Figure 4-6: Typical connections for T-stub ANSYS model

Monotonic displacement-controlled loading was imposed on the assembly. Loading was applied as a fixed rotation at the two edges of the T-stub facing the column in the actual assembly. This rotation is shown in **Figure 4-7**. An angle of 5.71 degrees – equal to maximum drift of 10% expected during testing – was applied at this location.

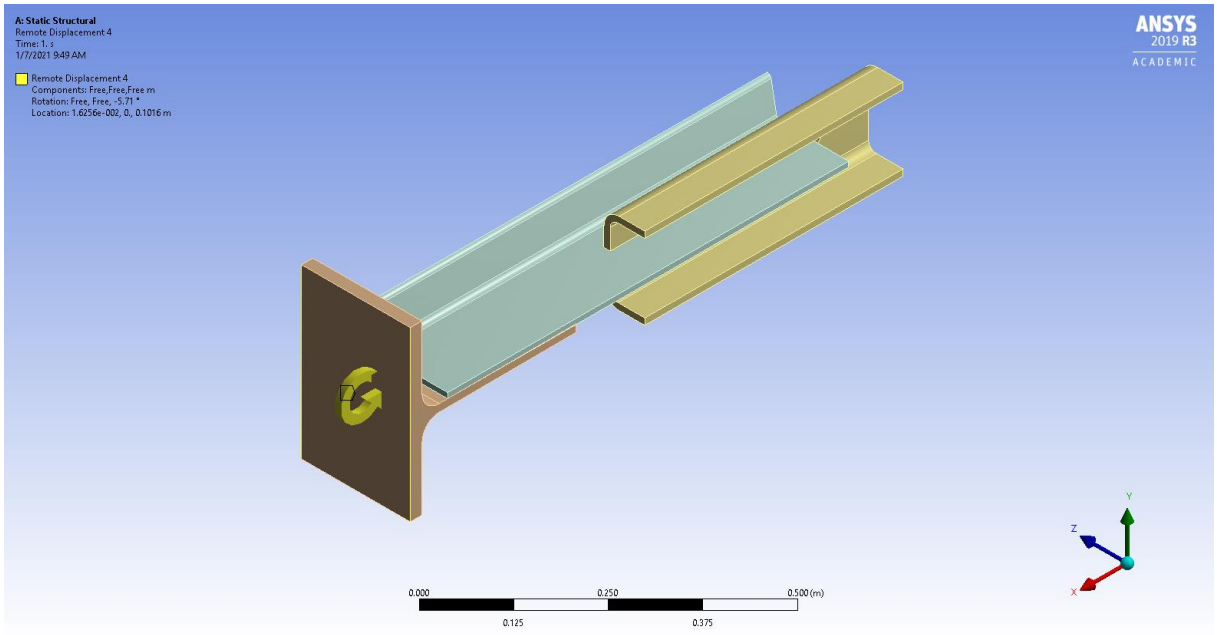

Figure 4-7: Monotonic loading for T-stub assembly

Results of the two ANSYS analyses were compared on a qualitative and quantitative basis. The objective of this exercise was to determine where deformations will predominantly occur in each connection. **Figure 4-8** and **Figure 4-9** show the deformation profile of the original and alternate knife plate models, respectively. Note that the HSS is not included in these figures for the sake of clarity. A pronounced curve may be observed in the original knife plate that was not present in the alternate model. This observation validated the researchers' concern that the flat knife plate would experience deformations contrary to the design intent. The deformation pattern

shown in **Figure 4-9** was considered the ideal deformation pattern. Qualitative results from the ANSYS analysis showed that the alternate detail is promising.

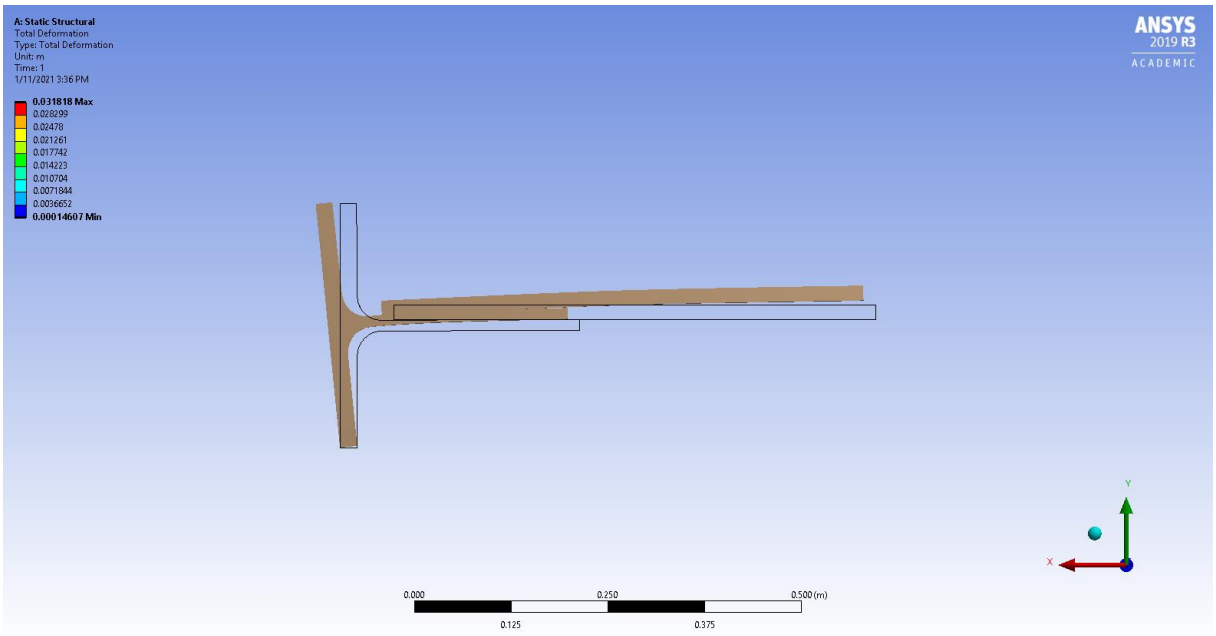

Figure 4-8: Deformed shape of original knife plate ANSYS model

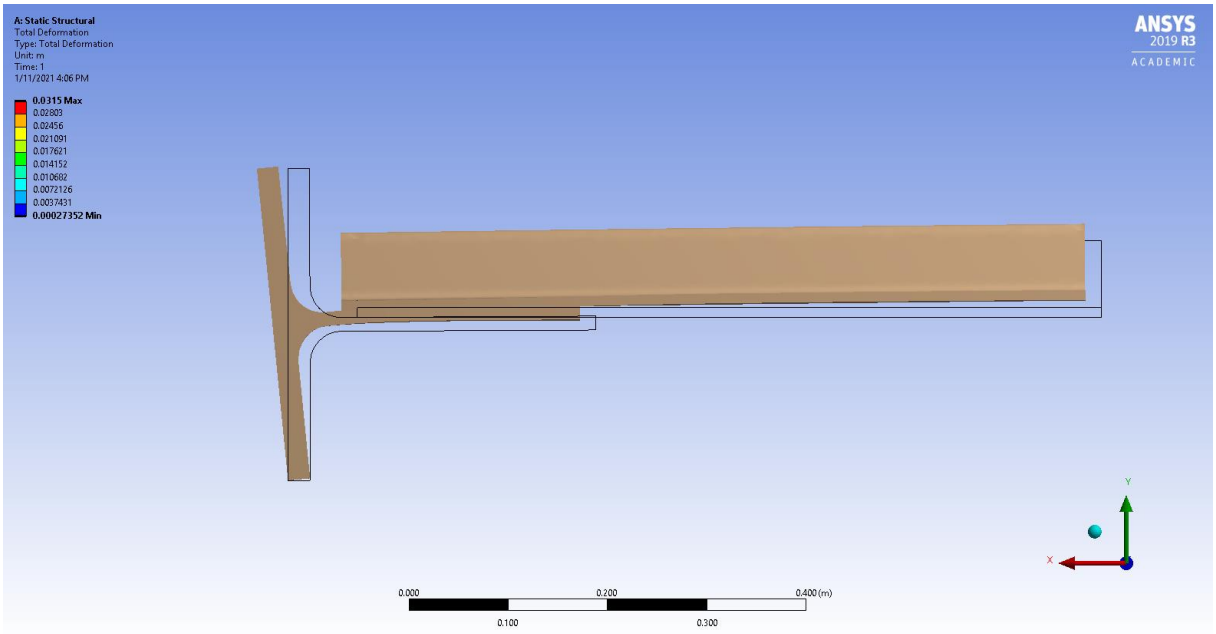

Figure 4-9: Deformed shape of alternate knife plate ANSYS model

A quantitative measure of relative deflection was accomplished by inspecting the strains on the two possible bending components in both analyses. Ideally, the knife plate would return to its undeformed shape after the structure was unloaded. Permanent deformations are caused by strains that occur in the plastic deformation range. Therefore, the likelihood of permanent deformations on each component was assessed by the prevalence of plastic strains on those members. Contour plots of strain for the original and alternate knife plate configurations are provided in **Figure 4-10** and **Figure 4-11**, respectively. In the original configuration, the maximum strain on each component was approximately 20% greater than the corresponding yield strain. By contrast, the alternate detail exhibited a maximum strain 62% above yield on the T-stem and strain did not exceed the yield limit on the knife plate.

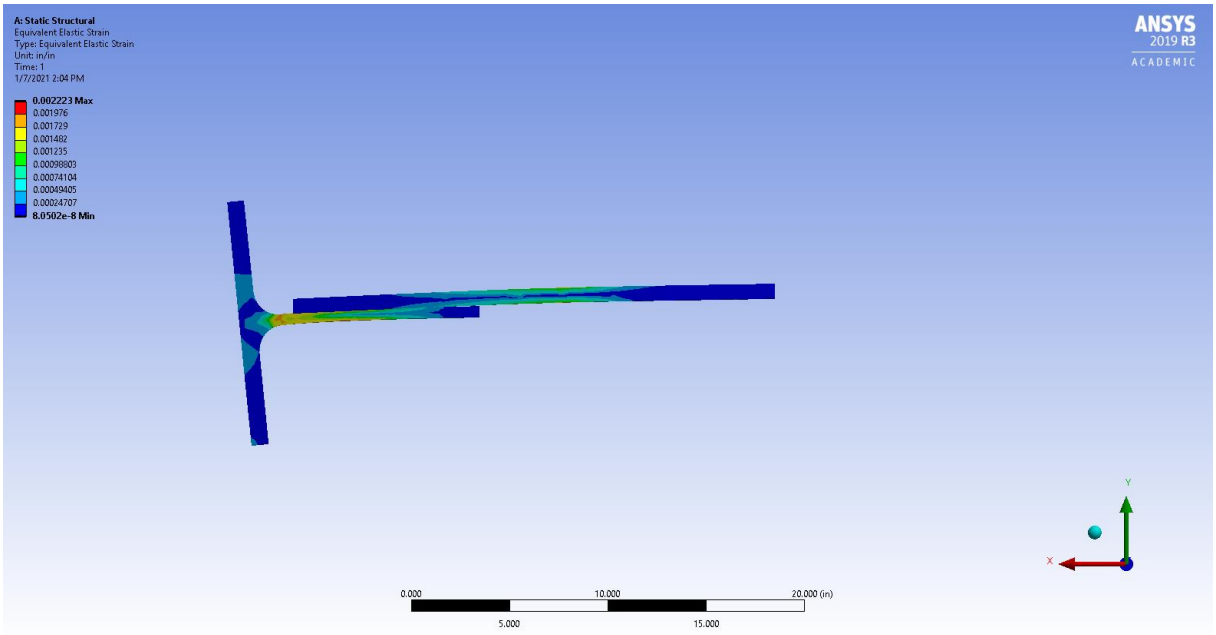

Figure 4-10: Strain distribution on T-stub and original knife plate, from ANSYS

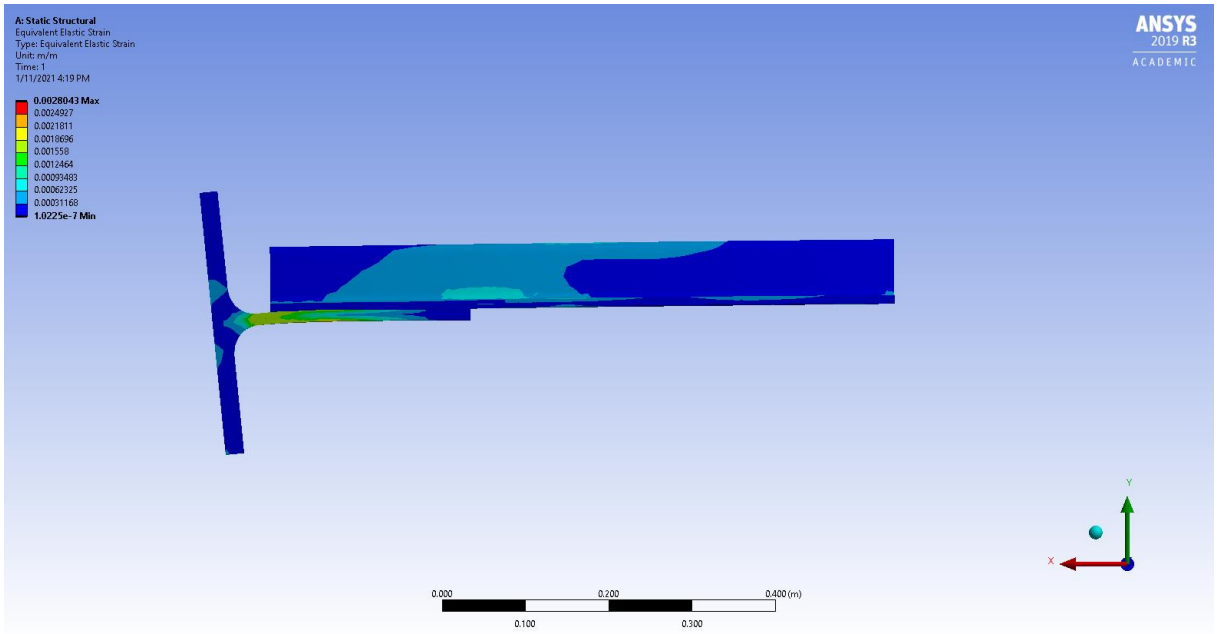

Figure 4-11: Strain distribution on T-stub and alternate knife plate, from ANSYS

Qualitative and quantitative results from the computational analyses carried out in ANSYS showed that the original detail exhibited deformations that were contrary to the design intent of the T-stub connection. As was predicted using simple hand calculations, deformations were distributed between the knife plate and the T-stub, rather than being concentrated in the T-stub alone. This observation was reinforced by the presence of plastic strains along the length of the original knife plate. This simulation also validated the proposed alternate knife that utilized a channel instead of a flat plate so that plastic strains and deformations were contained in the T-stem alone. However, this monotonic analysis did not provide any information about the hysteretic behavior of the connection. Deformed shape and inelastic strain excursions correlate with plastic deformations, but the extent of those deformations was not captured by this analysis. Before investing in the alternate detail within the full-scale setup, the researchers decided to verify the finite element results via experimental testing.

4.2 Experimental Testing

The test setup shown in **Figure 4-12** was used to evaluate the T-stub connection. This setup was designed to approximate the boundary conditions at each side of the T-stub connection in the bare-steel gravity framing assembly. For ease of assembly, the setup was designed using only bolted connections. The HSS member that holds the knife plate in the bare-steel assembly was not included. A base beam was bolted to the strong floor to provide a static reaction surface for the connection. The knife plate was then bolted to the base beam according to the hole pattern shown on the right in **Figure 4-13**. A half-inch spacer plate was placed between the knife plate and the T-stem to account for the diagonal knife plate that is present in the final assembly. Connecting the T-stem and the knife plate were 1" diameter bolts laid out as shown on the left in **Figure 4-13**. This hole pattern was the same pattern used in the bare-steel gravity framing assembly. A C15x40 channel referred to as the "spreader channel" was attached to the flanges of the T-stub. The spreader channel was intended to remain essentially rigid during testing, just as the column is intended to remain during the full-scale test. At the top of the spreader channel, 13" above the centerline of the T-stem, the actuator was connected to the assembly.

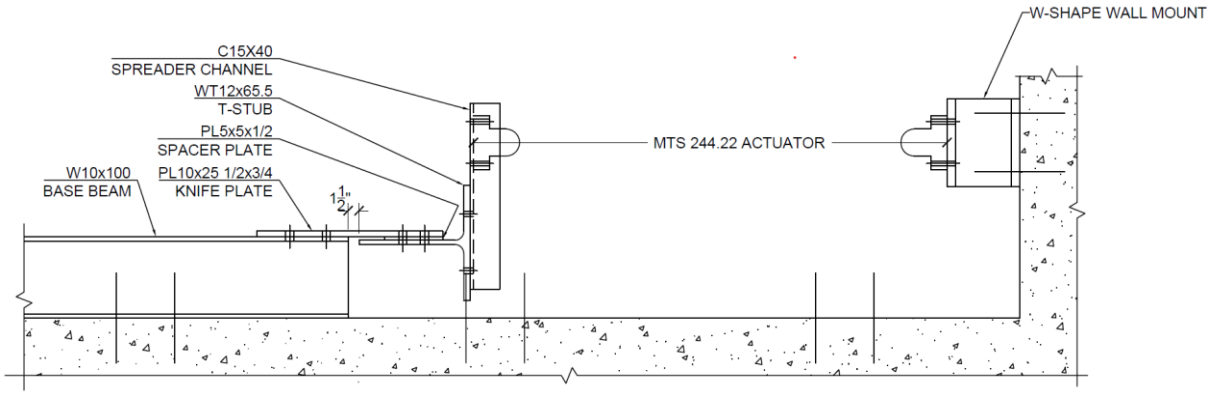

Figure 4-12: T-stub connection test set up schematic

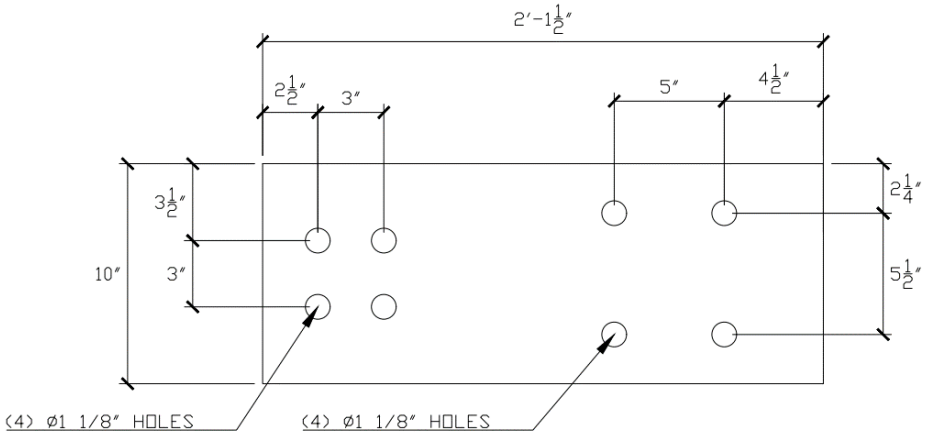

Figure 4-13: Hole pattern for knife plate used in T-stub test

4.2.1 Loading

An MTS 244.22 actuator, with a maximum capacity of ±22 kips, induced lateral motion at the top of the spreader channel. The actuator was driven by an MTS Flextest 60 controller and reacted against the laboratory strong wall. **Figure 4-14** shows the pattern of loading that was applied in terms of system drift. Each load step corresponded to a drift calculated over the moment arm between the centerline of the T-stem and the line of action of the actuator. This loading pattern was identical to the pattern that will be imposed on the bare-steel gravity framing specimen. Starting at a drift of 0.375%, the actuator pushed and pulled the assembly for six cycles. This set of six cycles were repeated at additional drifts of 0.5% and 0.75%. For all subsequent sets, the actuator was stopped at a drift of 0% in between each peak for visual documentation. A set of four cycles at a drift of 1% was then completed. The test proceeded increasing the drift by 0.5% per set of two cycles up to a drift of 11%. The assembly was returned to a drift of 0% at the end of the experiment.

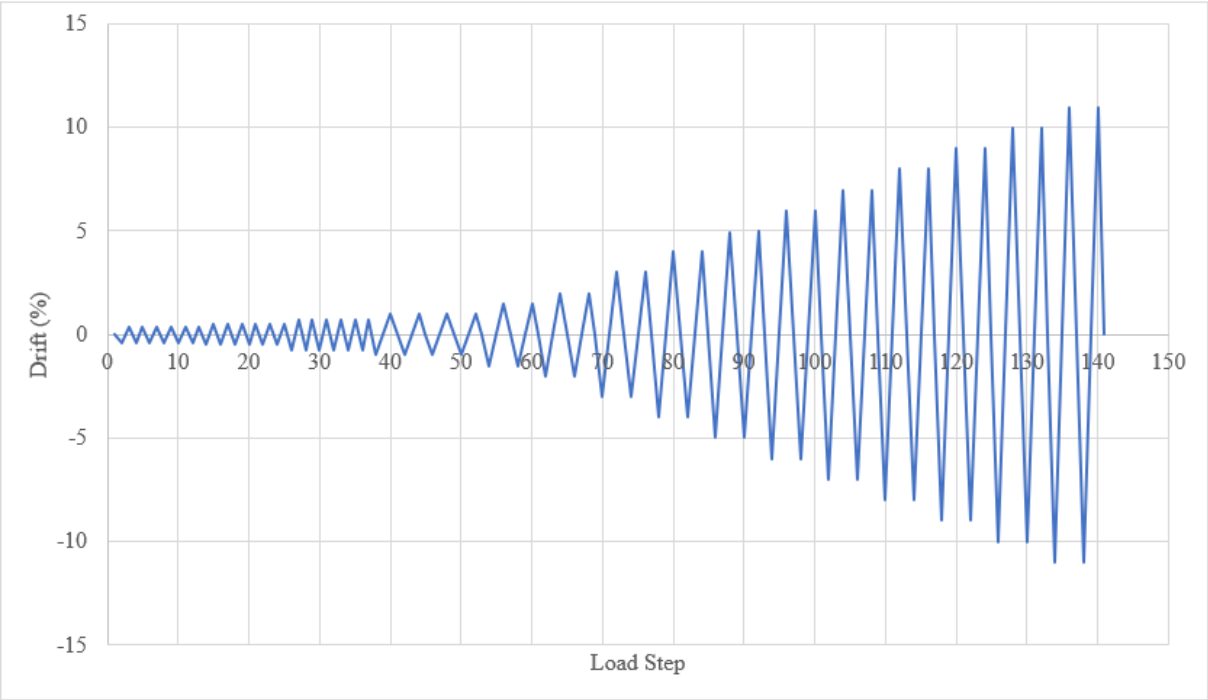

Figure 4-14: Load protocol used during T-stub test in terms of system drift

4.2.2 Instrumentation

Several different instrumentation components were used to measure the response of the assembly. For a qualitative, visual appraisal of yielding, whitewash was applied to the top surfaces of both the knife plate and the T-stem. As plastic strains occurred, the brittle mill scale would flake off, thereby removing the whitewash. This phenomenon allowed the researchers to observe the location of inelasticity as the test progressed. **Figure 4-15** shows the whitewash applied to the two members of interest prior to testing.

Figure 4-15: Photograph of T-stub test setup showing whitewash on the members of interest

An Optotrak Certus system was set up with infrared LED markers along the edge of the specimen as shown circled in blue in **Figure 4-16**. Twenty-two markers were used to collect data. This optical tracking technology measured the position of the infrared LEDs relative to a rigid body consisting of an additional four markers, shown boxed in red in **Figure 4-16**. These measurements were accurate to 0.1 millimeters and allowed the researchers to record the profile of the specimen continuously during testing. Data were recorded at a rate of 2 Hz. In addition to tracking the bending profile of the T-stem and knife plate, the Optotrak system recorded valuable observations of the test setup itself, including the behavior of the connections between the

specimen and the auxiliary testing members. Markers on the knife plate and the T-stub were spaced at 3" while markers on the spreader channel were spaced at 6".

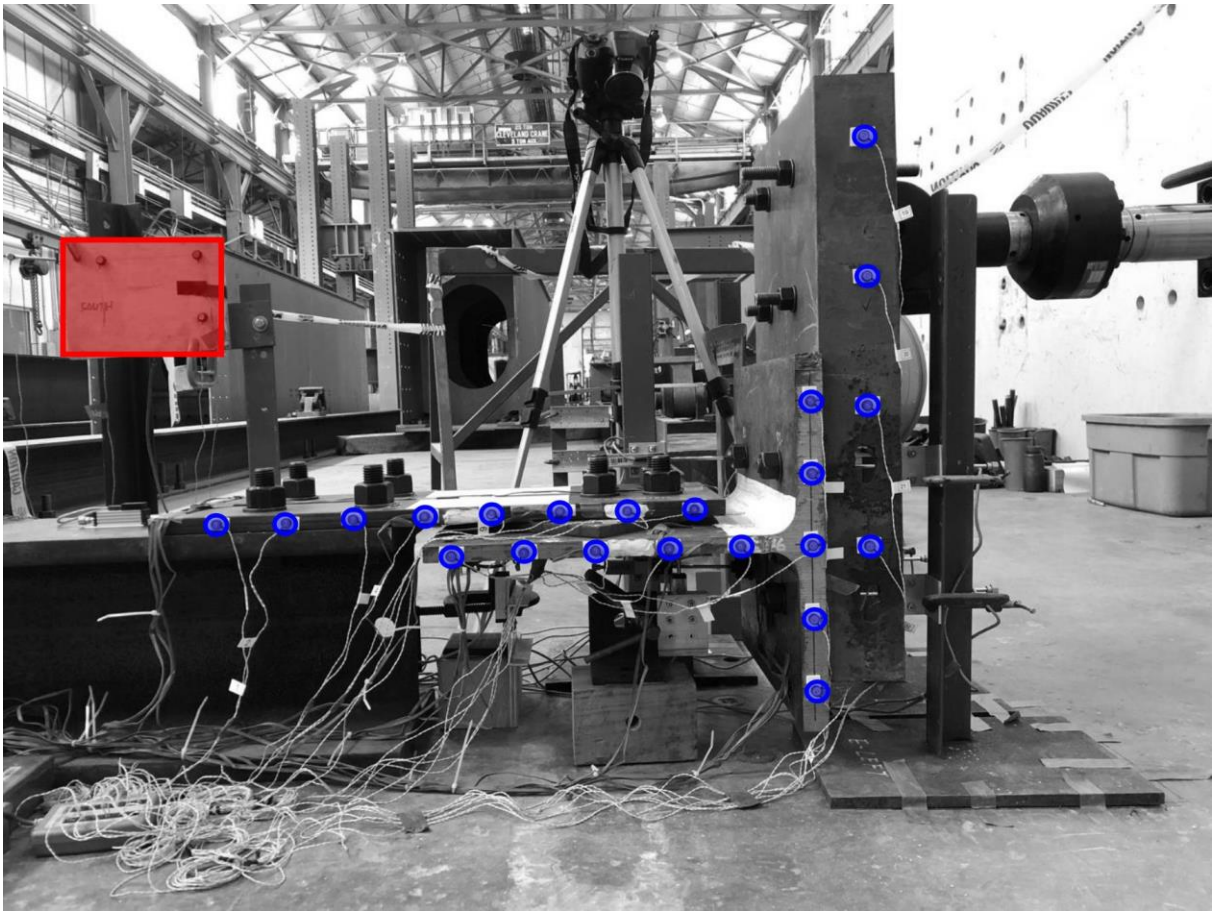

Figure 4-16: Photograph of LED markers used for Optotrak Certus instrumentation

Strain gauges were applied to the knife plate and the T-stem as indicated by filled rectangles in **Figure 4-17**. These quarter-bridge gauges from Tokyo Instruments (model number FLAB-6-11-5LJCT-F) had a gauge length of 6 millimeters and resistance of 120 ohms. Strain gauges mounted on the sides of the specimen provided a measure of axial deformation of each section while the strain gauges mounted on the top and bottom of the members provided a measure of flexural strains. These gauges tracked excursions into the inelastic strain range, providing a basis for comparison between the experimental and computational analyses.

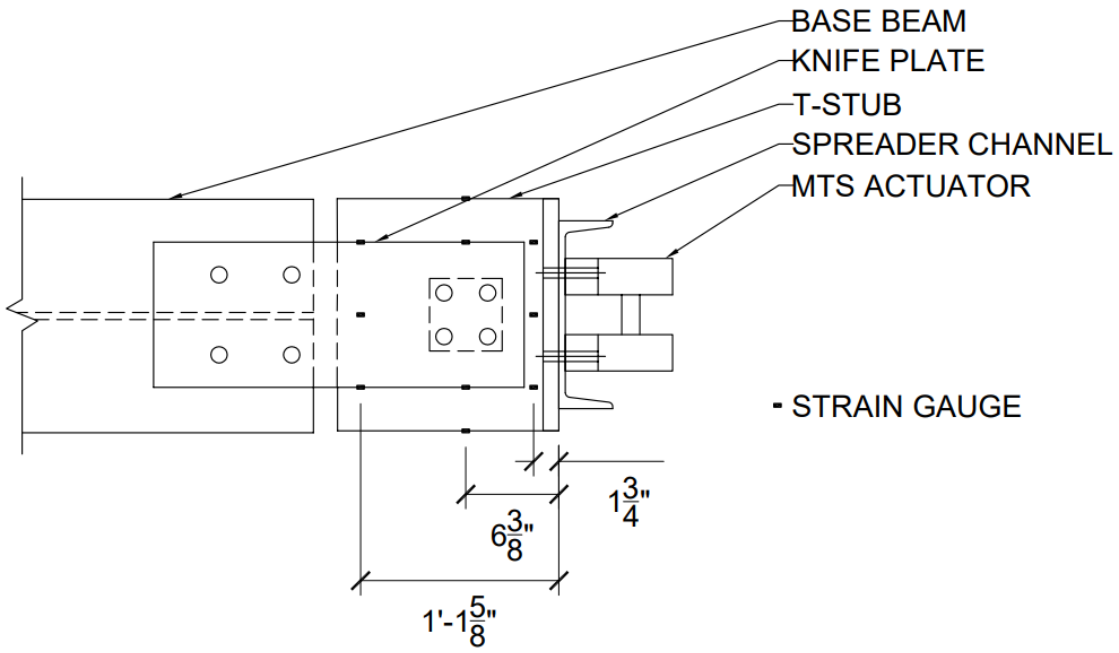

Figure 4-17: Layout of strain gauges on the members of interest during T-stub testing

Linear potentiometers were used to track the motion of points on each member relative to the static position of the potentiometer mounting. One set of potentiometers was set against the head and threaded end of the bolts connecting the T-stub and the spreader channel. This set of six potentiometers, marked "A" in **Figure 4-18**, were used to observe the rigid rotation of the T-stub flange and the spreader channel. During testing, the mountings of the potentiometers marked "A" physically moved, resulting in an inconsistent reference. Therefore, these sensors did not provide usable data. Another linear potentiometer, marked "B" in **Figure 4-18**, was mounted on top of the reaction beam and reacted against the end of the knife plate. Data from this channel was used to quantify slip in the bolted connection between the knife plate and the reaction beam. Finally, two potentiometers marked "C" in **Figure 4-18** were mounted beneath the assembly and measured deflection at two points on the T-stem at and beyond the bolted connection. Bending in the T-stem was expected to be limited to the protected zone between the bolted connection and

the flange. Therefore, lacking curvature beyond the bolted connection, the average slope of the T-stem could be derived as the slope between the two “C” potentiometers. Had set “A” produced usable results, the angle between the T-stub flange and the stem could have been derived by comparing the inclination of those two components. This data would have allowed the researchers to determine the proportion of deformation in the T-stem as a fraction of the total deformation imposed by the actuator. Ultimately this result was derived using data from the Optotrak system.

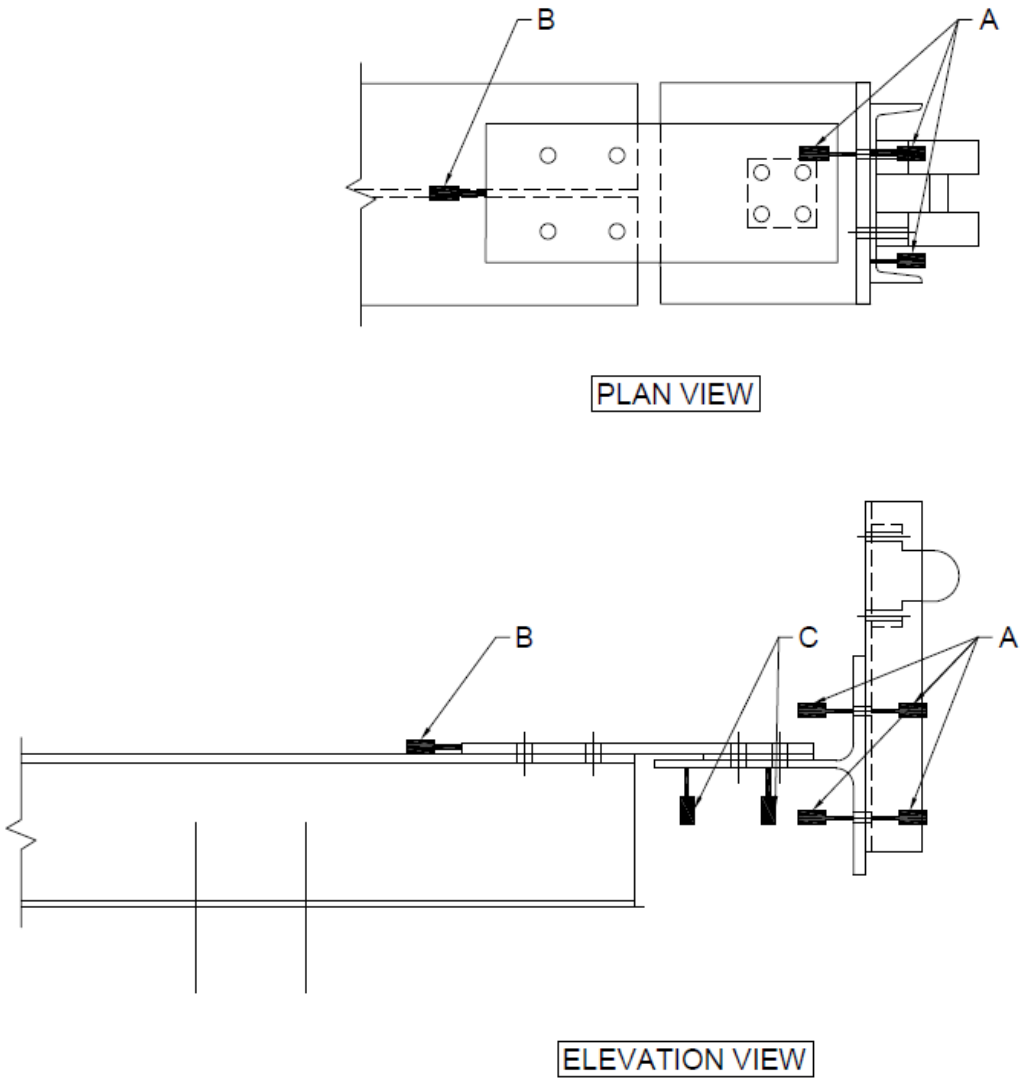

Figure 4-18: Layout of linear potentiometers on the members of interest during T-stub testing

Finally, two cameras were set up as shown in **Figure 4-19**. These cameras were used to take photographs at each increment in the load cycles. Photographs from these cameras were used to assess damage. Select photographs from these cameras are included in this thesis.

Figure 4-19: Photograph of T-stub test setup including cameras used to document damage

4.3 Results

Data from the experiment were analyzed as described in the following three subsections. Linear potentiometer data were not used due to the error that occurred when the Group A sensors moved. Optotrak position data was used to quantify the proportion of deformations shared between the knife plate and T-stem. Rotation at the bolted base beam connection, which was meant to simulate the welded connection between the knife plate and HSS member, was also

assessed using Optotrak data. Strain gauges tracked strain excursions into the inelastic range on both bending components. Data from the load cell embedded in the MTS actuator was used to derive a moment-rotation relationship for the connection. Visual observations were recorded throughout the duration of the experiment.

4.3.1 Optotrak Data

Output from the Optotrak system was in the form of 3D cartesian coordinates for each LED marker at each time step. Data were provided in millimeters with the origin defined at the rigid body. The initial position of each of the markers in the X-Y plane is shown in **Figure 4-20**. To assess the distribution of deformations between the two bending components, lines were fit using a least-squares algorithm to mathematically define the T-stub flange and the T-stem. **Figure 4-21** shows the lines fit to the initial positions of the markers on the T-stub flange and the T-stem with the markers used to define those lines circled in blue. Starting from the left in the figure, only the first four markers on the T-stem were used to define that component. These four markers were placed at or after the bolted connection and were therefore assumed to experience only the rotation that took place on the T-stem between the T-stub flange and the bolted connection. The same strategy of using lines of best fit to determine deformation at each time step was used to quantify rotation at the bolt group attaching the knife plate to the base beam. The two markers boxed in red in **Figure 4-21** were positioned at the bolts that connected the knife plate and the base beam. Rotation calculated between these two markers was used to correct for the fact that a welded connection accommodating no rotation is used in the full-scale specimen.

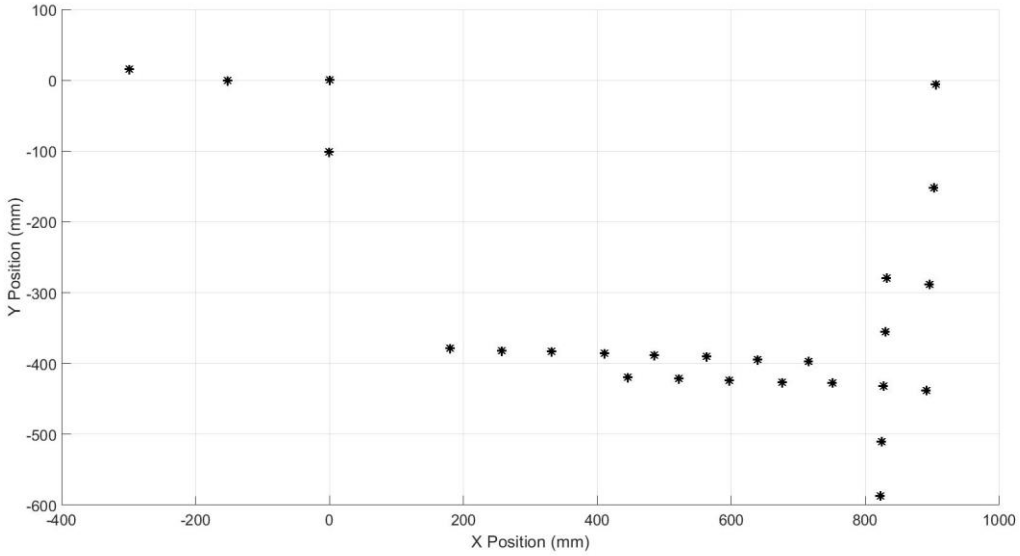

Figure 4-20: Initial position of Optotrak markers on the profile of the T-stub test setup

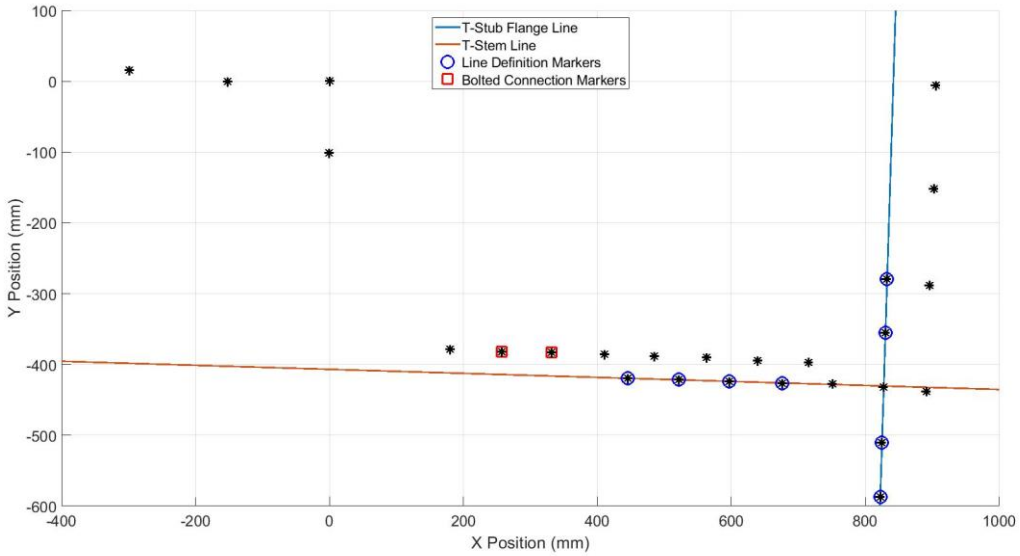

Figure 4-21: Initial position of Optotrak markers with best-fit lines describing the spreader channel and the T-stem

For each frame of data collected by the Optotrak system, the overall drift of the system was calculated as the angle of the T-stub flange relative to the starting position. The rotation of the T-stem was calculated at each time step as the angle between the T-stem and the initial position. Deformation of the T-stem was calculated as the difference between the overall drift and T-stem

rotation. A plot of the overall drift, deformation of the T-stem, and rotation at the bolted base beam connection at each time step is shown in **Figure 4-22**. Deformation at the bolted base beam connection never exceeded 0.05% rotation or 1% of the total drift. Functionally, deformations were shared exclusively between the knife plate and the T-stem. **Figure 4-23** shows the proportion of the total rotation accommodated by each component. Records associated with drifts less than 0.1% were eliminated in **Figure 4-23** because the ratio of deformations and system drift was not meaningful when drift was small. Between 60% and 70% of deformations took place in the knife plate. As drifts became large, causing inelastic strains to become more likely, the share of deformations stabilized with 40% of the system rotation taking place in the T-stem and 60% of the system rotation taking place in the knife plate.

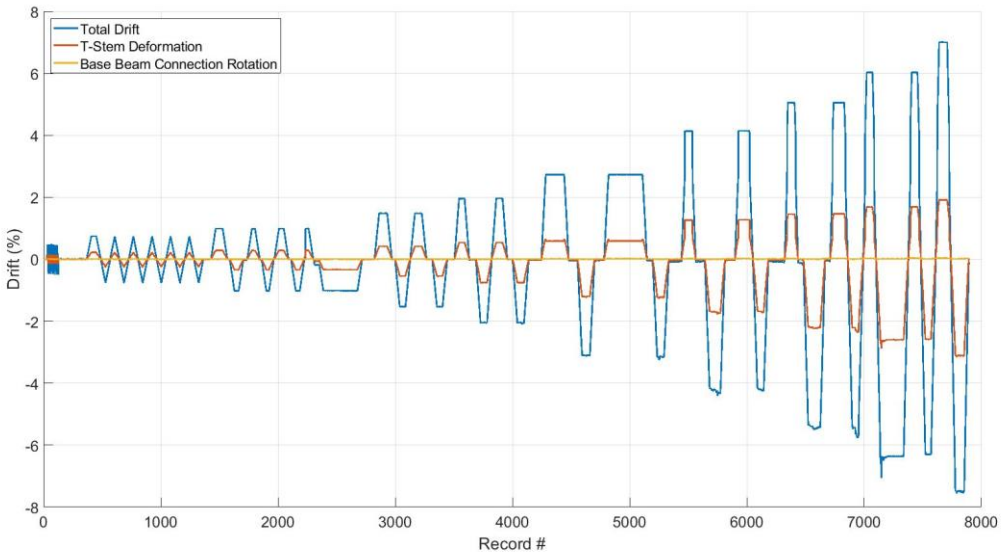

Figure 4-22: Plot of total system drift, T-stem deformation throughout the T-stub test

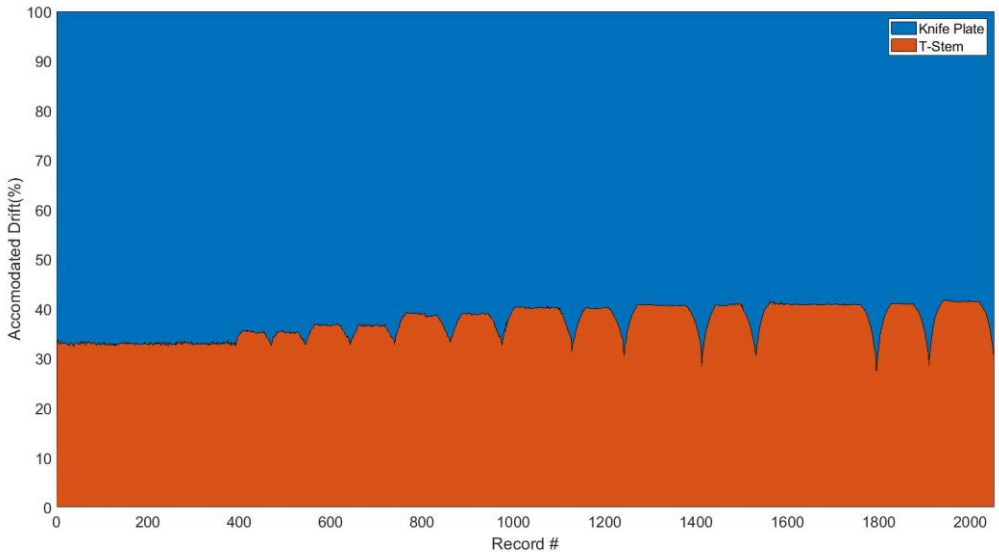

Figure 4-23: Share of deformation between the knife plate and T-stem as a proportion of total drift

The results obtained from the Optotrak system validated the experimental design and the results obtained from computational analysis. The total system drift measured at the T-stub flange matched the load protocol within a fraction of a percent. The small error that existed is attributable to the precision of the actuator used to impose deformations. Additionally, it was found that the bolted base beam connection allowed minimal rotations, closely approximating the welded connection in the full-scale assembly. As predicted in computational analysis, deformations were shared between the T-stem and the knife plate. Data from the Optotrak system suggests that the knife plate experienced more deformation that the T-stem. This result is contrary to the intended behavior of the detail wherein deformations are concentrated in the T-stem. However, the deformations and inelasticity observed in the knife plate may or may not lead to unacceptable permanent deformations.

4.3.2 Strain Gauges

Just as inelastic strain excursions were used to quantify the distribution of bending deformations in the computational model, strain gauge readings in the inelastic range were used to characterize the behavior of the experimental specimen. **Figure 4-24** identifies the two strain gauges used for this purpose. One of these strain gauges, SG1.2, tracked strain on the top of the knife plate while gauge SG2.5 tracked strain on the top of the T-stem. **Figure 4-25** shows a plot of each strain record at these locations over the duration of the test. Horizontal lines denoting the yield strain for the A992 T-stub and the A36 knife plate are shown. Peaks that cross these lines indicate that yielding occurred.

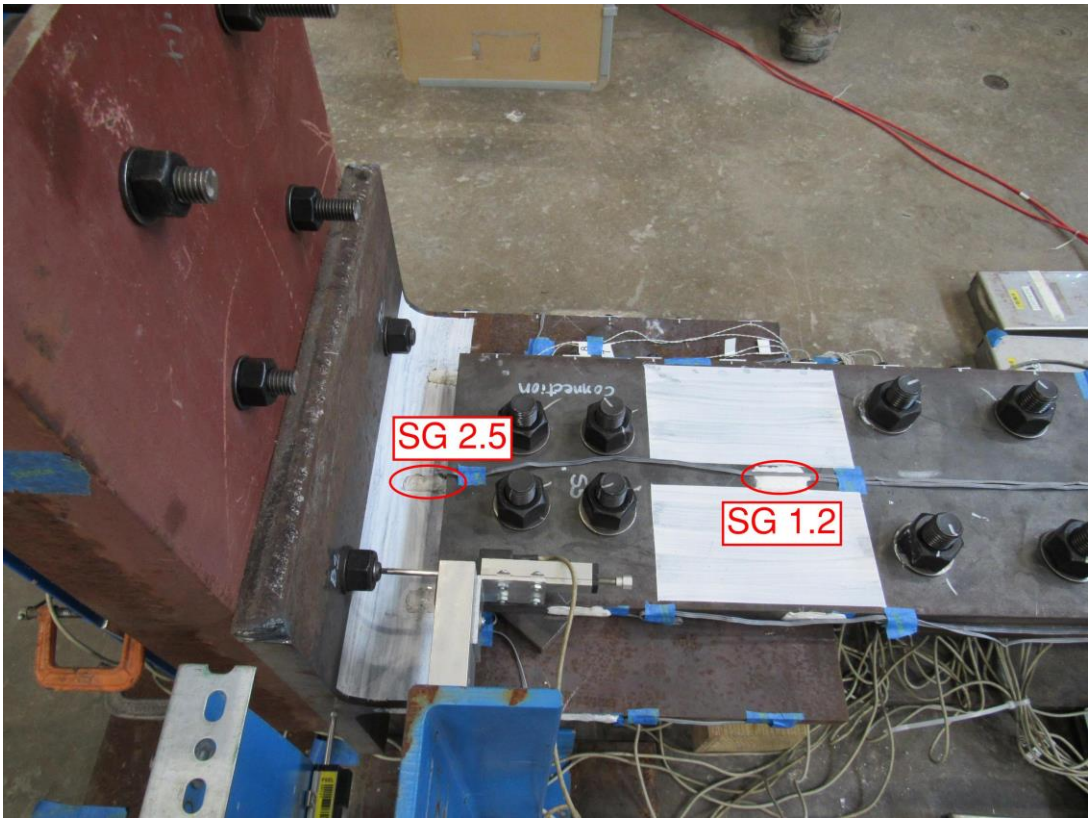

Figure 4-24: Photograph of T-stub specimen with strain gauges 1.2 and 2.5 marked

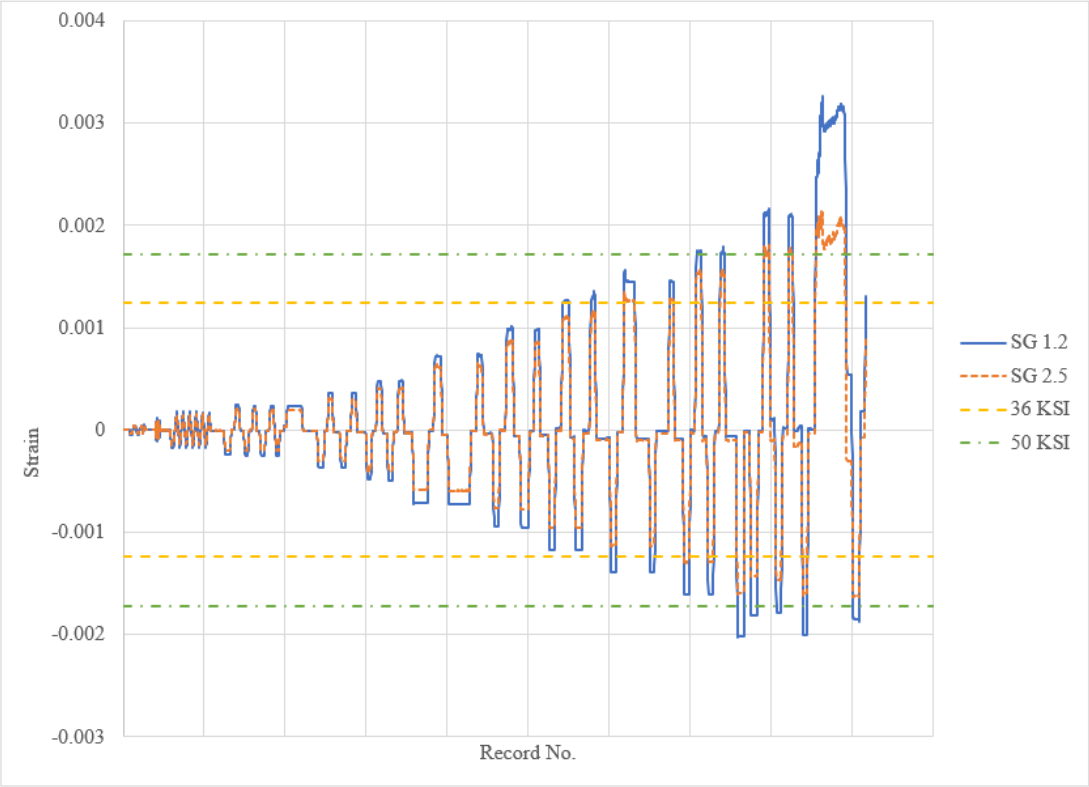

Figure 4-25: Plot of strain excursions at the top of the knife plate (SG1.2) and the top of the T-stem (SG2.5)

As shown in **Figure 4-25**, the knife plate experienced greater strains than the T-stem at every load increment. The knife plate was manufactured from A36 steel while the T-stub was manufactured from A992 steel. Due to this difference and the larger strains experienced by the knife plate, yielding was observed in the knife plate earlier in the experiment than the T-stem. The knife plate first experienced strains in the inelastic range at a drift of 5% while the T-stem did not begin to yield until a drift of 8%. This result was consistent with the computational analysis of the connection. The large strains observed on both sections indicated that deformations were shared between the two components. The maximum strain observed on the knife plate was 260% of the yield strain. This is contrasted with the T-stem, which experienced a maximum strain equal to 120% of the yield strain. Experimental strain data indicate that the knife plate experiences substantially higher strains than the T-stem both in absolute terms and

relative to the yield strain of the component. This result differs from the computational analysis, which suggested that both components experience peak strains approximately 20% greater than their respective yield strain. The presence of greater strains in the knife plate than in the T-stem is consistent with the observation from the Optotrak system that the knife plate experienced more deformation than the T-stem.

During the experiment, the maximum actuator force was 3.5 kips. As stated previously, the expected base shear on the gravity framing specimen is 226 kips, based on preliminary nonlinear analyses. Dividing this load evenly among the three actuators at the top story, each T-stub connection at the southernmost column-line is expected to experience 75.3 kips of axial loading. The difference between the axial loading in the T-stub test and in the full-scale experiment is significant. The increased axial stress during the full-scale experiment will cause additional yielding to occur on both bending components at locations where bending stresses cause compression. This additional yielding is not expected to impact the distribution of deformations between the two members because it will be uniform over each cross section. When decomposed into axial and bending strain profiles, no difference is expected in the bending profiles experienced in the T-stub test and the full-scale test. The increased axial load in concert with the deformed shape due to bending may encourage a buckling limit state. Buckling is not expected due to the factors of safety used when designing the top diaphragm.

4.3.3 Load Cell Data

The load cell embedded in the MTS actuator tracked the resistance of the T-stub connection to motion along the axis of loading. Assuming a moment arm of 13", the distance between the axis of loading and the centerline of the T-stem, the moment in the connection was calculated. This derived moment was likely greater than the actual moment experienced by the

connection because the centroid of the connection is expected to be between the centerline of the knife plate and the centerline of the T-stem. A moment-rotation relationship for the connection is shown in **Figure 4-26**. Some inelasticity is observed in the moment-rotation relationship. An elastic stiffness of $354\ \mathrm{k-in/rad}$ was calculated for the connection. Due to the assumed moment arm, this stiffness is approximate. The moment-rotation relationship of the T-stub connection will be subject to further study during full-scale testing.

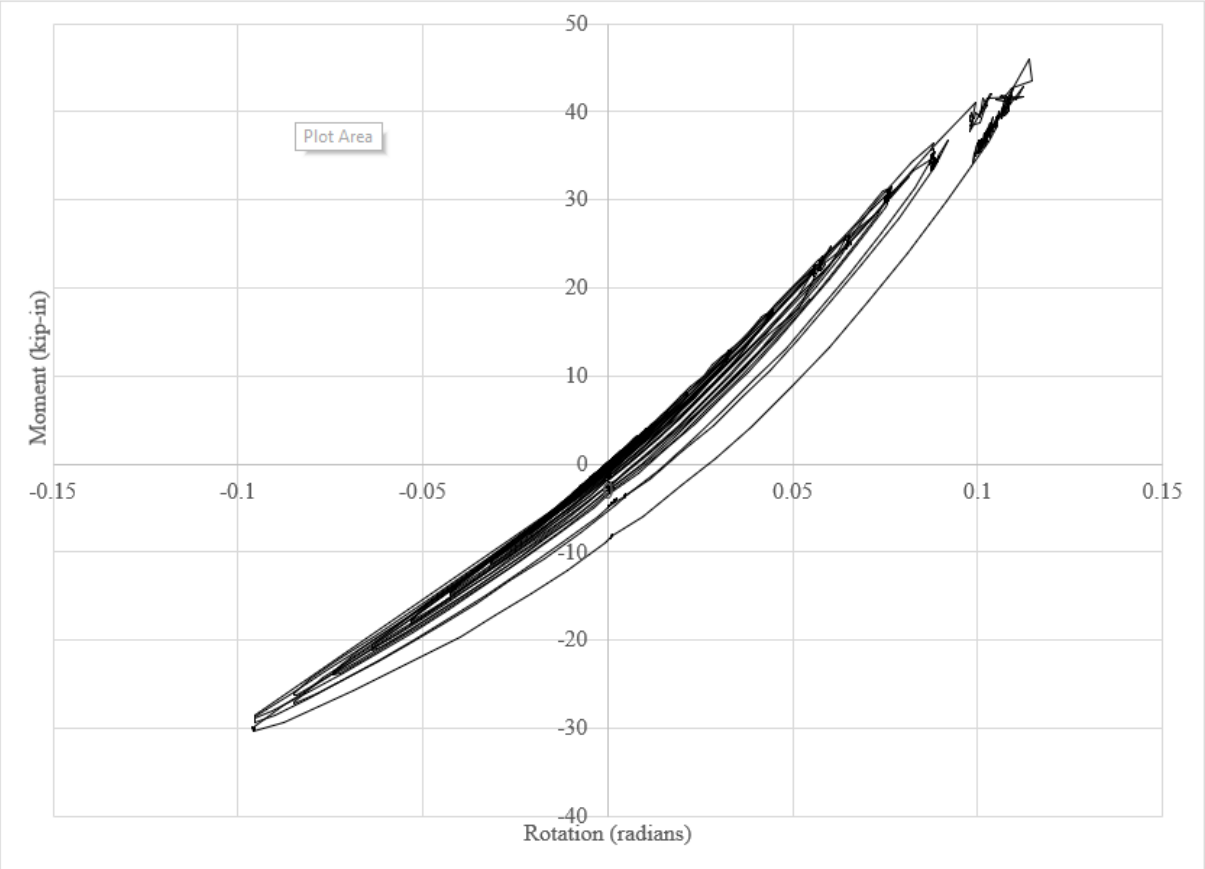

Figure 4-26: Plot of moment-rotation relationship for T-stub connection

4.3.4 Visual Observations

Visual observations were taken during and after the T-stub test. These observations included inspection of the whitewash, the assembly, and the individual components. Photographs were taken at every load increment for review.

Despite yielding detected by the strain gauges, a yield pattern was not observed in the whitewash applied to the tops of each component. This behavior may have been due to the ratio of lime to water used when mixing the whitewash. A mix containing a larger proportion of water is less likely to prevent the mill scale from separating from the steel substrate. It is also possible that the mill scale simply did not flake off in the strain range experienced by the components. Whitewash provided no valuable observations.

Large deformations were observed in each component at the peak of a drift cycle. **Figure 4-27 (Left)** shows the system before displacement while **Figure 4-27 (Right)** shows the system at 10% drift. Both components are visibly bent in this photograph. The knife plate shows the most dramatic deformation directly to the right of the base beam connection. An oblique angle may be observed between the T-stem and the T-stub flange. Prior to deformation, the T-stem and the T-stub flange were nominally perpendicular.

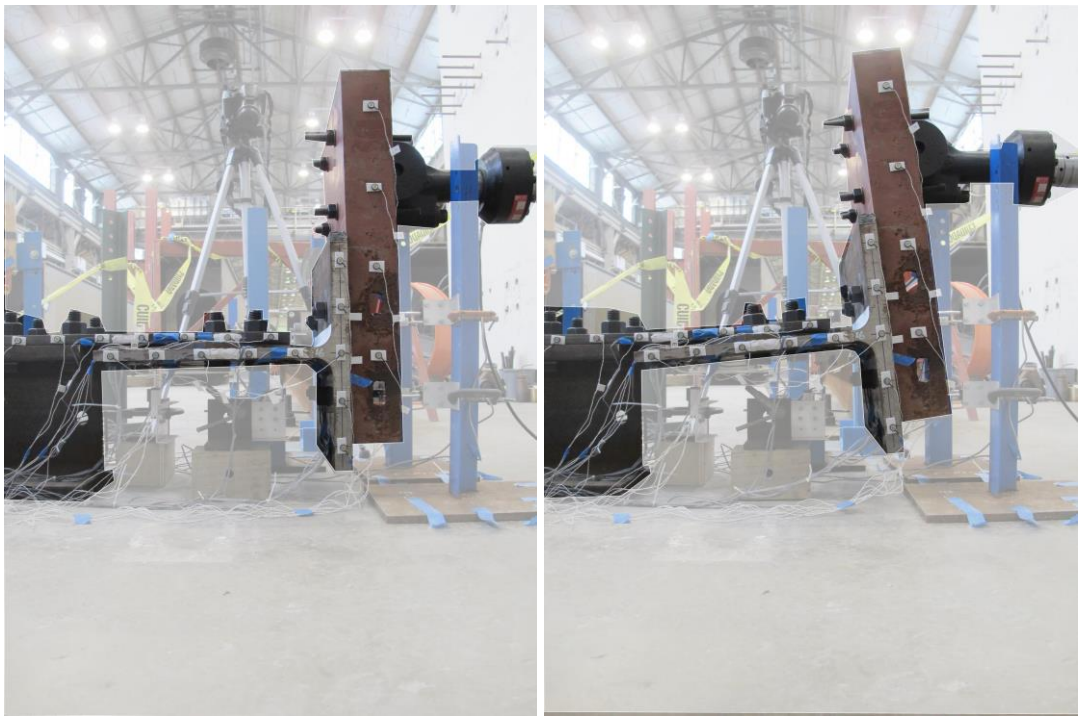

Figure 4-27: (Left) T-stub test assembly at 0% drift, (Right) T-stub test assembly at 10% drift

After the experiment was completed and the specimen was disassembled, each component was inspected to observe residual deformations. The knife plate is pictured in **Figure 4-28** with the side corresponding to the bolted base beam connection resting on a nominally flat surface. Permanent deformation of the plate resulted in an offset of 3/8" at the end that connects to the T-stem. The plate was observed to be nominally flat prior to the experiment. Similarly, **Figure 4-29** shows the T-stem after the T-stub experiment with a right-angle measuring device aligned to the center of the T-stub flange. An offset of 1/8" was observed at the tip of the T-stem due to permanent deformations. These measurements of permanent deformation provided a sense of scale to the expected plastic deformations that will be present after the full-scale test. These deformations are small enough to be corrected for during construction.

Figure 4-28: Permanent deformation observed on the knife plate after specimen disassembly

Figure 4-29: Permanent deformation observed on the T-stub after specimen disassembly

4.4 Summary and Recommendations

Spatial data collected with an Optotrak Certus system, strain data from strain gauges, and visual observations were used to characterize the behavior of the T-stub connection. The Optotrak system captured the location of LED markers placed on the profile of the T-stub test specimen. By comparing the overall drift of the system with the tracked rotation of the T-stem, it was determined that the T-stem accommodated approximately 40% of total drift while the knife plate accommodated approximately 60%. This pattern was reinforced by strain gauge data. Strain gauge data from the T-stem indicated lower strains and fewer excursions into the inelastic range when compared to the knife plate. Both these results speak to a failure of the connection to behave according to the design intent. Ideally, deformations are concentrated in the T-stem and the knife plate does not experience any inelastic deformation. After the experiment was

concluded, permanent deformations of 3/8" were measured on the knife plate while the T-stem exhibited permanent deformations of 1/8".

Despite the data showing large deformations and plastic excursions on the knife plate, it was decided that the original knife plate detail would be sufficient for the full-scale experiment. After the experiment was completed and the assembly was returned to the initial position, permanent deformations were observed to be within construction tolerance. The ultimate objective of the T-stub test was to determine if the components of the top diaphragm could be reused in subsequent tests. By reusing the T-stubs and HSS members in the same position each time, the components are expected to mate correctly despite deformations on each member. Additionally, construction methods are available that will allow for deformation correction as the components are installed. For these reasons, an investment in the alternate knife plate detail was deemed unnecessary.

5 CONCLUSIONS AND FUTURE WORK

Contrary to the conventional design assumption that gravity framing does not contribute any lateral stiffness or strength to a building, research has suggested that gravity framing may substantially impact the lateral behavior of structures. Multiple mechanisms of lateral resistance have been observed, including moment resistance in the connection (Leon, 1990) and continuity of the gravity columns (Foutch & Yun, 2002; Flores, Charney, & Lopez-Garcia, 2014). Most of the literature focusses on bare-steel behavior. Donahue (2019) sought to study the impact of a composite slab on the lateral performance of gravity framing using a cruciform test specimen. This thesis discusses an extension of Donahue's research to system-level testing.

To study the behavior of gravity framing in a typical structure, a full-scale, two-bay by three-bay frame was developed. Although the experiments on the full frame have not yet been conducted at the completion of this thesis, the frame has been fabricated and erected. Before testing the system with a composite slab, an experiment will be conducted on the bare-steel frame. The steel frame specimen consists of W12x96 columns and W21x55 girders. Double angle connections are used to attach the girders to the columns. Perpendicular to the lateral loading, W14x22 beams frame between the columns. Clevises are used to connect the column bases to a reaction beams anchored to the strong floor. These clevises have negligible resistance to moment and were chosen to enforce the idealized point of zero moment at midheight of a story. The tops of the columns attach to a truss diaphragm. This diaphragm will transmit lateral loads to each column-line and maintain the spacing during the experiments. The connection between the tops of the columns and the truss diaphragm members utilized a WT section. Throughout this thesis, this connection is dubbed the "T-stub connection." The goal of T-stub connection is to transmit minimal moment to the members of the diaphragm in order to enforce the idealized point of zero moment at midheight of the story above.

Prior to fabrication of the bare-steel specimen, there was uncertainty regarding the beahvior of the T-stub connection. The intent of the connection is to avoid damaging the diaphragm members by isolating deformations in the replacable T-stub, thereby making the top diaphragm easier and less expensive to reassemble in subsequent tests. However, prelminary analyses demonstrated that the knife plate connecting the truss members to the WT was marginally less stiff than the WT. Computational analyses in ANSYS indicated that this difference in stiffness led to deformations being shared between the knife plate and the WT section. It was unknown whether plastic deformations during the full-scale experiments will

result in permenent deformations hindering reassembly of the specimen. Therefore, an experiment focusing on the diaphragm connection was completed. Strain gauge data from the experiment agreed with the results of the ANSYS model, and optical tracking data indicated that the knife plate accomodated more deformation than the WT section. Upon dissassembly, however, the observed permanent deformations in the knife plate were found to be within construction tolerances. Therefore, the top truss was fabricated using the T-stub connection without modification.

5.1 Future Work

The bare-steel experiment will provide information regarding the behavior of the specimen and testing frame. This information will inform the instrumentation of subsequent tests that include a composite slab. Preliminary details regarding the composite slab are included in the plan set in the Appendix. These details will be refined as the specimen is developed following the completion of the bare-steel test. Ultimately, composite specimens will be constructed and tested to determine the behavior of composite gravity framing under seismic loading. The results from these experiments will be used to develop computer models that can be used to predict behavior of more general cases.

APPENDIX: SPECIMEN GEOMETRY

GENERAL NOTES

PRIMARY CODES AND SPECIFICATIONS

1. GENERAL BUILDING CODE – IBC 2015
2. DESIGN LOADING – ASCE 7–14
3. STEEL CODE – AISC MANUAL, 15TH EDITION
4. CONCRETE CODE – ACI 318–14
5. DESIGN IS BASED ON SAC MODEL BUILDING PRESENTED IN FEMA 355C

STEEL

1. ASTM MATERIAL DESIGNATIONS, UNLESS OTHERWISE NOTED
   - 1.A. W–SHAPES – A992, Fy = 50KSI
   - 1.B. HSS – A500 GR.C, Fy = 50KSI
   - 1.C. PLATES & GUSSETS – A36, Fy = 36KSI
2. BOLTS AND ANCHORS, UNLESS OTHERWISE NOTED
   - 2.A. BOLTS – A325, Fu = 120KSI
3. PRETENSIONED BOLTS SHALL BE TENSIONED TO THE MINIMUM SET FORTH BY AISC. BOLT TENSION SHALL BE VERIFIED USING SQUIRTER WASHERS CALIBRATED ON A SKIDMORE, OR SIMILAR
   - 3.A. MINIMUM PRETENSION: 3/4"ø – 28KIPS
     1"ø – 51KIPS
     1 1/4"ø – 81KIPS
4. ALL WELDS SHALL BE E70XX

CONCRETE

1. MATERIAL DESIGNATIONS, UNLESS OTHERWISE NOTED
   - 1.A. CONCRETE ON METAL DECK SHALL BE NORMALWEIGHT, f'c = 4KSI
   - 1.B. WELDED WIRE REINFORCING STEEL SHALL BE 6x6x1.4

GENERAL REQUIREMENTS

1. STRUCTURAL DRAWINGS INDICATE STABILITY ONLY FOR THE FULLY ASSEMBLED STRUCTURE. CONSTRUCTION BRACING SHALL BE PROVIDED DURING ERECTION.

LIST OF SHEETS	
SHEET #	CONTENT
S0.0	GENERAL NOTES
S1.1	FIRST FLOOR FRAMING PLAN
S1.2	SECOND FLOOR BRACING PLAN
S2.1	NORTH-SOUTH ELEVATION
S2.2	EAST-WEST ELEVATION
S3.1	BASE CONNECTION DETAILS
S4.1	FIRST FLOOR CONNECTION DETAILS
S4.2	FIRST FLOOR CONNECTION DETAILS
S4.3	SECOND FLOOR CONNECTION DETAILS
S4.4	SECOND FLOOR CONNECTION DETAILS
S4.5	SECOND FLOOR CONNECTION DETAILS
S5.1	DECK ATTACHMENT PLAN
S5.2	DECK ATTACHMENT DETAILS
S6.1	STRONG WALL ATTACHMENT PLAN AND DETAILS

General Notes

No.	Revision/Issue	Date

Firm Name and Address

Project Name and Address
NSF Gravity Framing

Project

Sheet
S0.0

Date
3/8/2021

Scale
As Noted

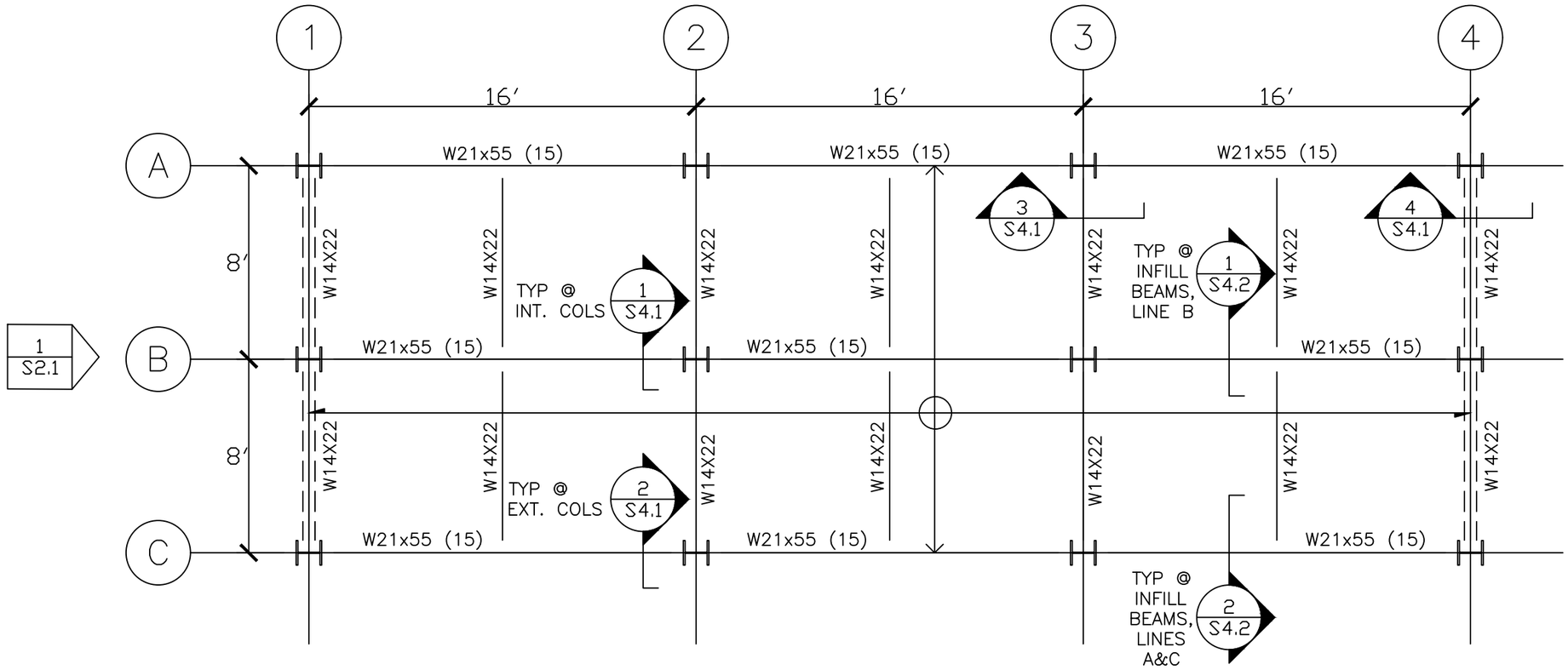

1 FIRST FLOOR FRAMING PLAN

SCALE: 3/16″=1′

N

1. FLOOR CONSTRUCTION: 4 ½" CONCRETE ON 2VL1 METAL DECK. TOTAL FLOOR THICKNESS 6 ½". WWR6x6x1.4 MAT REINFORCEMENT ON 3" CHAIRS IN DECK TROUGHS.
   1.1. SEE S5.1 FOR DECK ATTACHMENT PLAN
   1.2. DECK PANEL LENGTH SHALL NOT EXCEED 30'
2. TOP OF STEEL ELEVATION 7'–11 1/2"
3. COMPOSITE FLOOR CONSTRUCTION:
   3.1. 5"x¾"ø SHEAR STUDS
4. STUDS SHALL BE ATTACHED TO BEAMS PERPENDICULAR TO DECK SPAN AT EACH DECK TROUGH
5. SYMBOLS:

– DECK SPAN

– X BRACE ABOVE

– X BRACE BELOW

(XX) – NUMBER OF COMPOSITE STUDS

COLUMN SCHEDULE

COLUMN	SECTION	BASEPLATE
A-1,A-2,A-3,A-4,B-1,B-2,B-3, B-4,C-1,C-2,C-3,C-4	W12X96	1/S3.1

General Notes

No.	Revision/Issue	Date

Firm Name and Address

Project Name and Address

NSF Gravity Framing

Project

Date 3/8/2021

Scale As Noted

Sheet S1.1

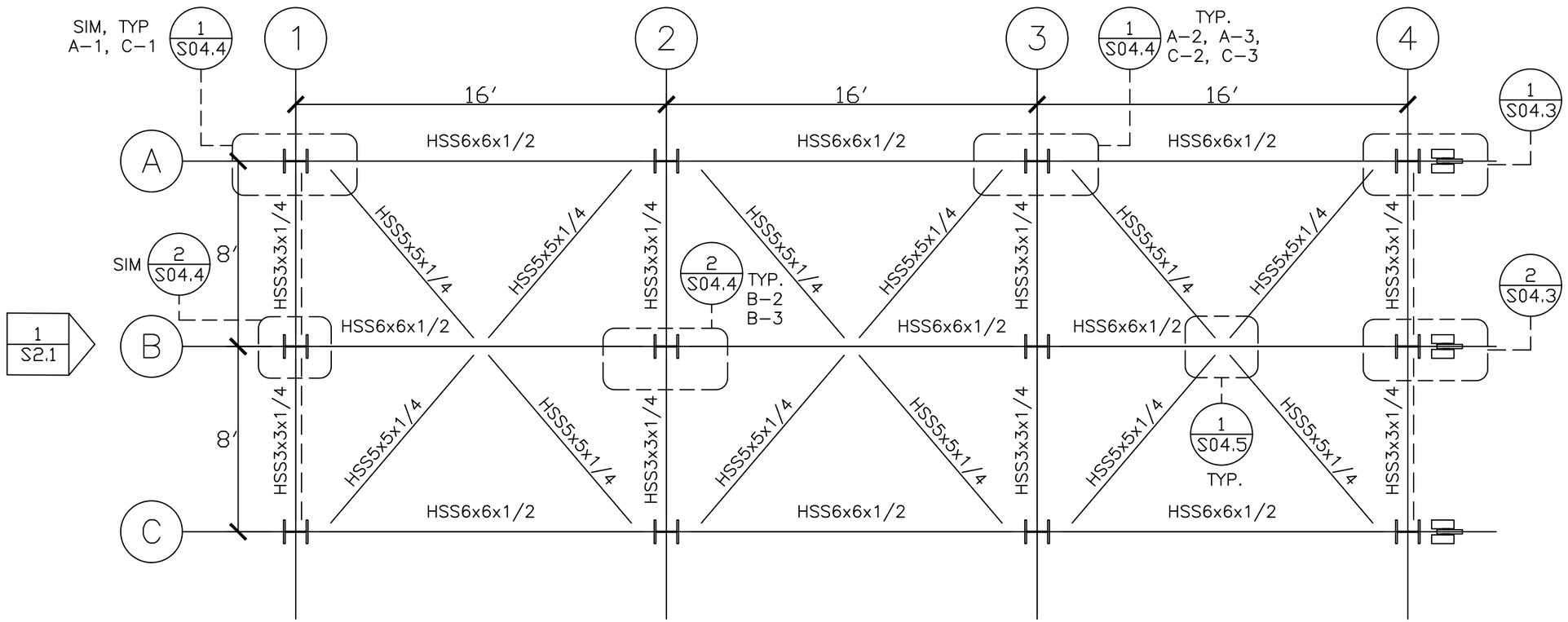

1 SECOND FLOOR BRACING PLAN

SCALE: 3/16"=1'

N

1. ACTUATORS ACT IN THE NORTH–SOUTH DIRECTION ON COLUMN LINE 4
2. TOP OF STEEL ELEVATION 13'–7"
3. SYMBOLS:

– ACTUATOR

– X BRACE ABOVE

– X BRACE BELOW

General Notes

No.	Revision/Issue	Date

Firm Name and Address

Project Name and Address

NSF Gravity Framing

Project	Sheet
Date 3/8/2021	S1.2
Scale As Noted	

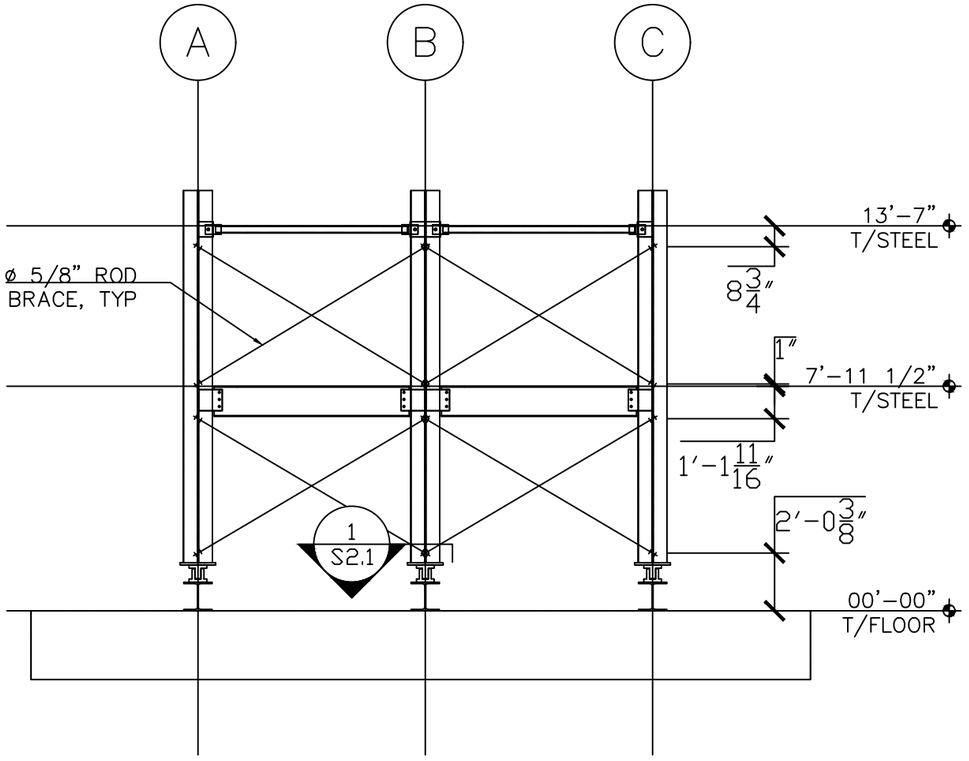

1 NORTH-SOUTH ELEVATION

SCALE:3/16"=1'

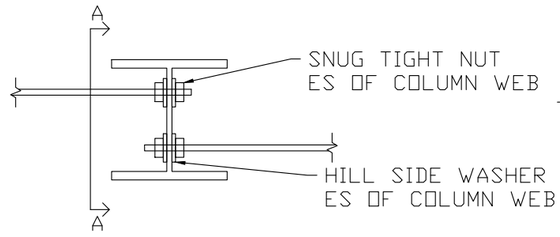

1 DETAIL

SCALE:3/4"=1'

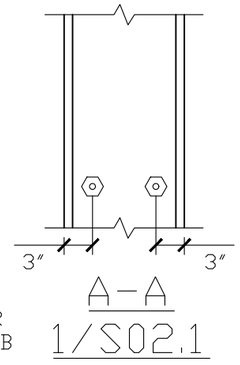

General Notes

No.	Revision/Issue	Date

Firm Name and Address

Project Name and Address

NSF Gravity Framing

Project	Sheet
Date 3/8/2021	S2.1
Scale As Noted	

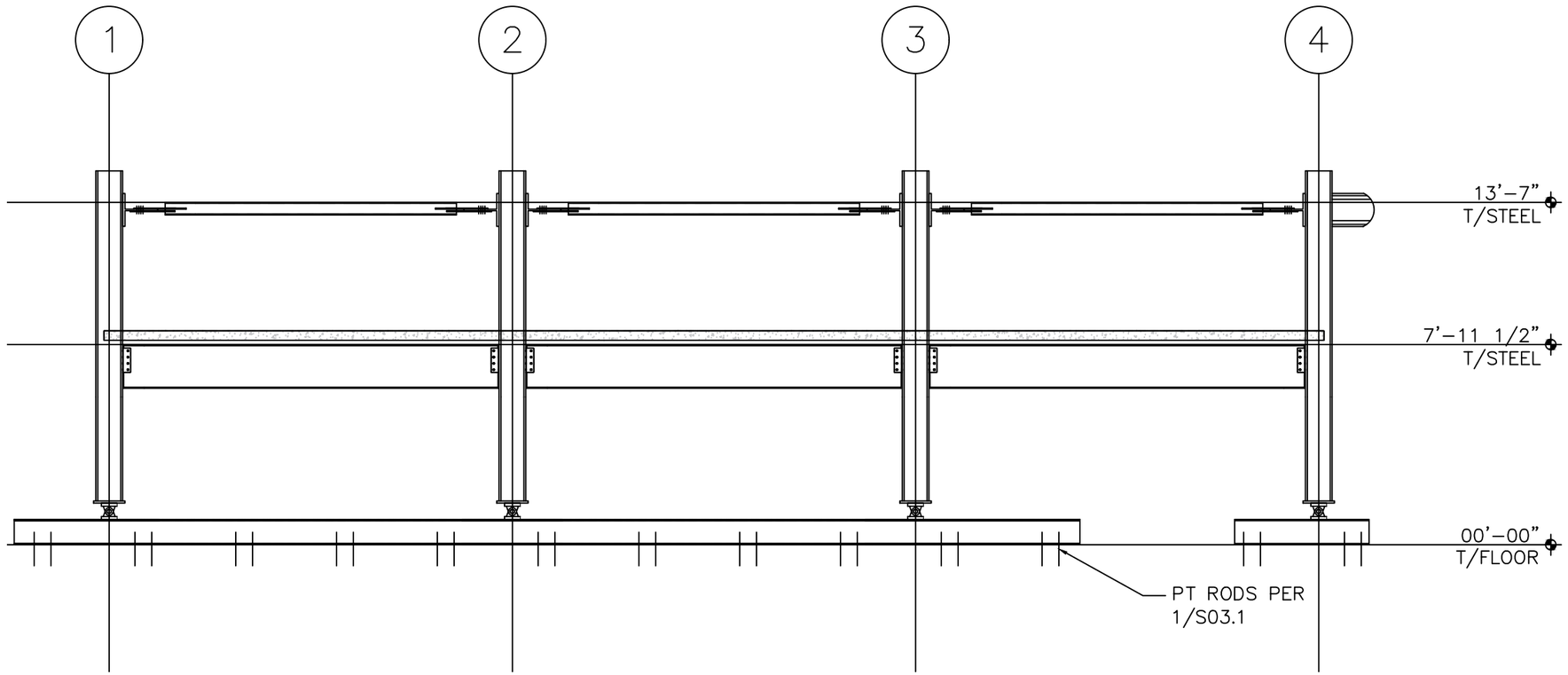

1 EAST-WEST ELEVATION

SCALE: 3/16"=1'

General Notes

No.	Revision/Issue	Date

Firm Name and Address

Project Name and Address

NSF Gravity Framing

Project

Date 3/8/2021

Scale As Noted

Sheet S2.2

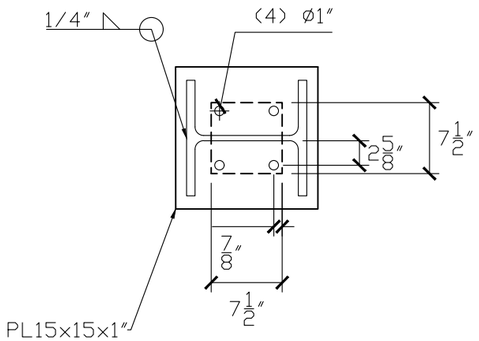

1 DETAIL

SCALE:3/4″ = 1′

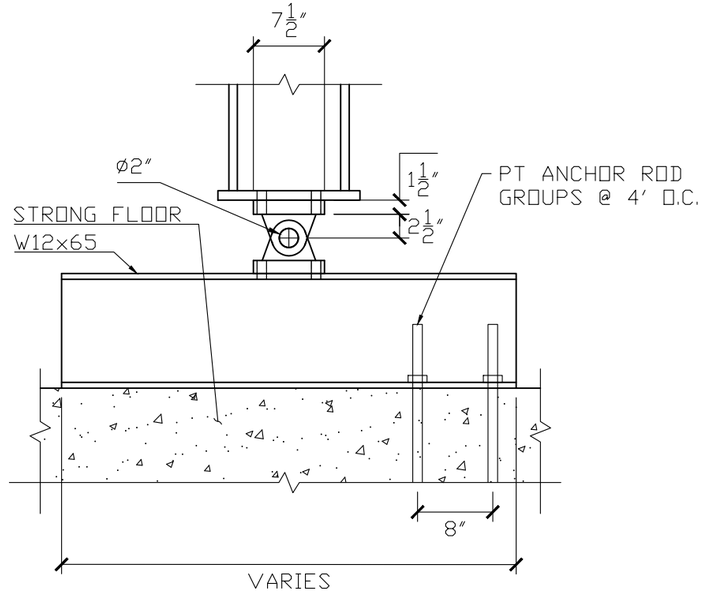

2 DETAIL

SCALE:3/4″ = 1′

General Notes

No.	Revision/Issue	Date

Firm Name and Address

Project Name and Address

NSF Gravity Framing

Project

Sheet

Date 3/8/2021

Scale As Noted

S3.1

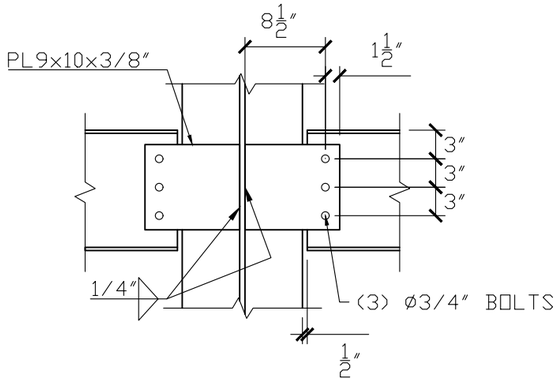

1 DETAIL
SCALE:3/4″ = 1′

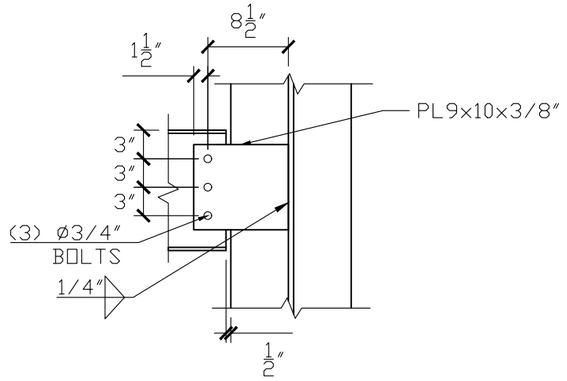

2 DETAIL
SCALE:3/4″ = 1′

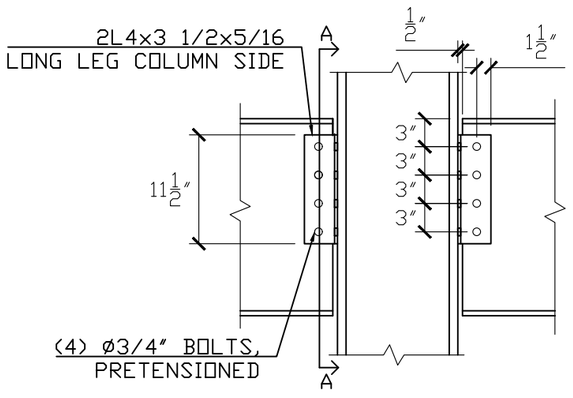

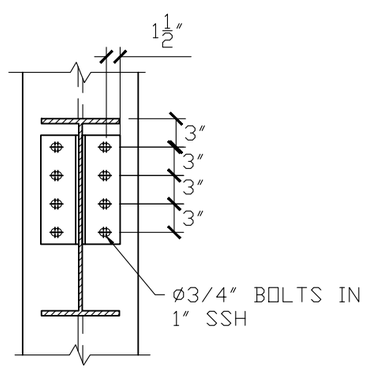

A–A
3/S04.1

3 DETAIL
SCALE:3/4″ = 1′

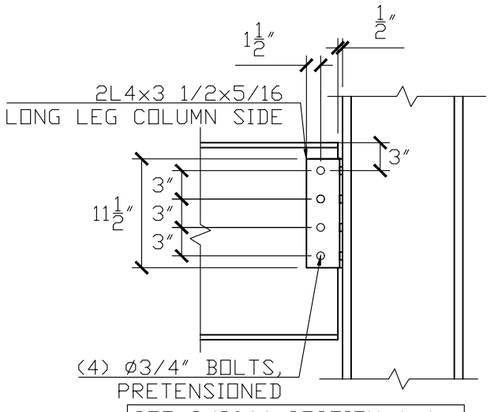

SEE 3/S04.1 SECTION A-A
FOR COLUMN CONNECTION

4 DETAIL
SCALE:3/4″ = 1′

General Notes

No.	Revision/Issue	Date

Firm Name and Address

Project Name and Address
NSF Gravity Framing

Project	Sheet
Date 3/8/2021	S4.1
Scale As Noted	

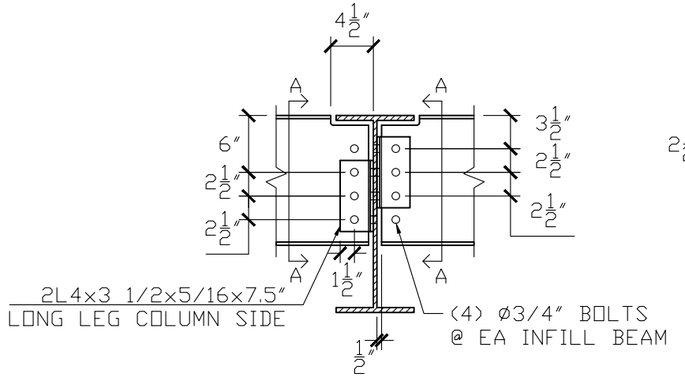

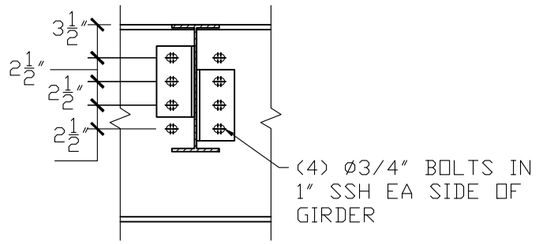

A–A
1/S04.2

1 DETAIL
SCALE:3/4" = 1'

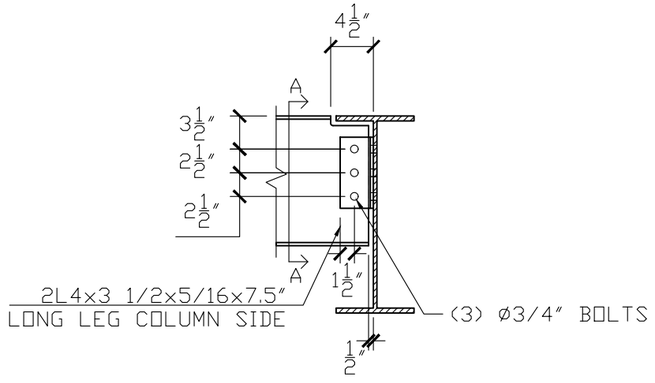

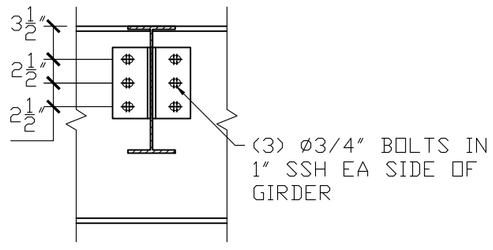

A–A
2/S04.2

2 DETAIL
SCALE:3/4" = 1'

General Notes

No.	Revision/Issue	Date

Firm Name and Address

Project Name and Address
NSF Gravity Framing

Project	Sheet
Date 3/8/2021	S4.2
Scale As Noted	

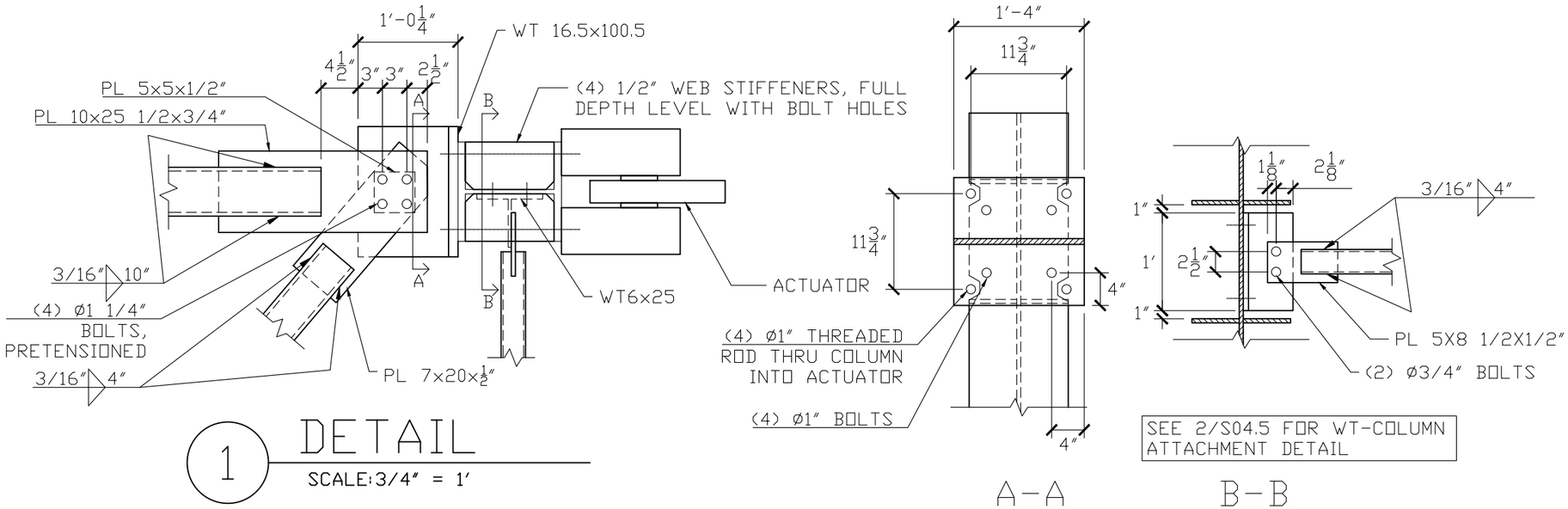

1 DETAIL

SCALE:3/4" = 1'

A-A
1/S04.3

B-B
1/S04.3

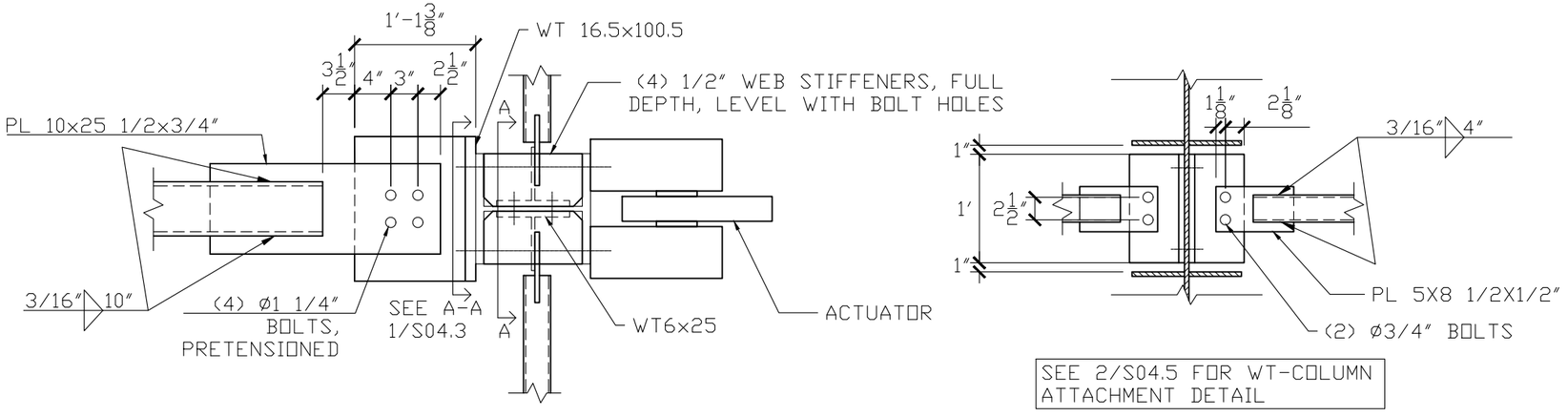

2 DETAIL

SCALE:3/4" = 1'

A-A
2/S04.3

General Notes

No.	Revision/Issue	Date

Firm Name and Address

Project Name and Address

NSF Gravity Framing

Project

Date 3/8/2021

Scale As Noted

Sheet S4.3

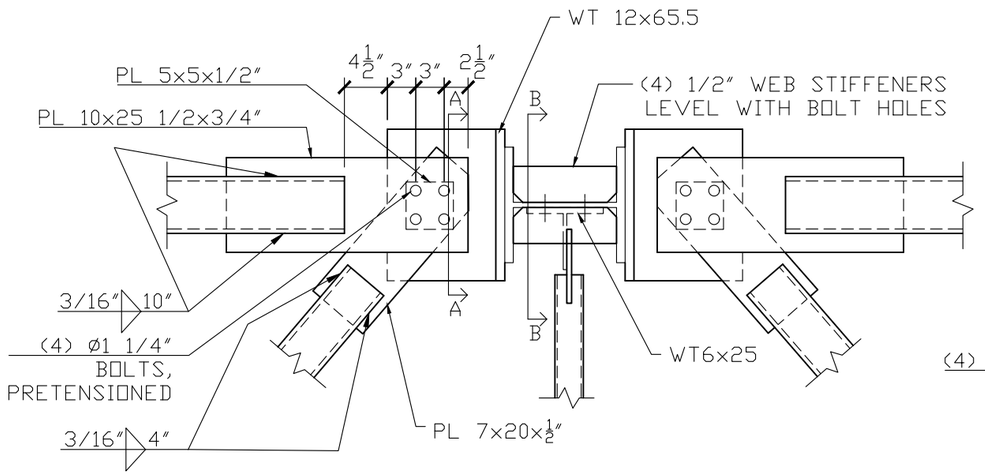

1 DETAIL

SCALE:3/4" = 1'

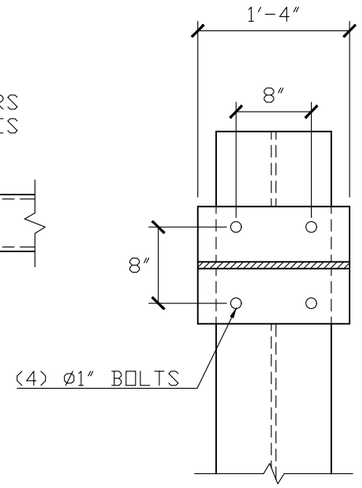

A–A
1/S04.4

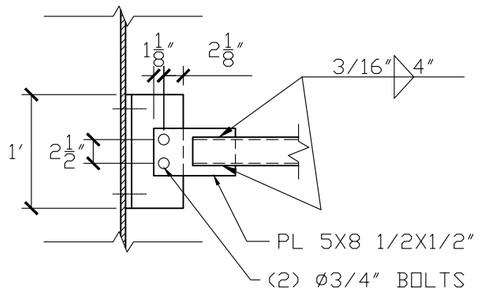

SEE 2/S04.5 FOR WT-COLUMN ATTACHMENT DETAIL

B–B
1/S04.4

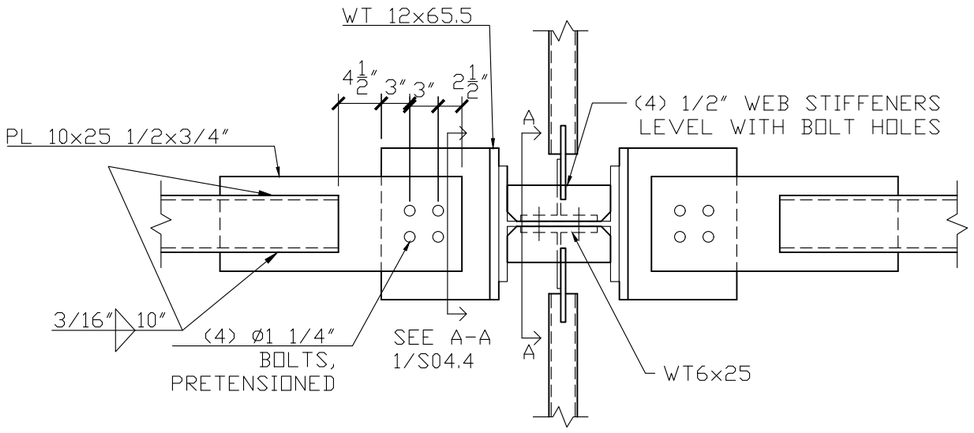

2 DETAIL

SCALE:3/4" = 1'

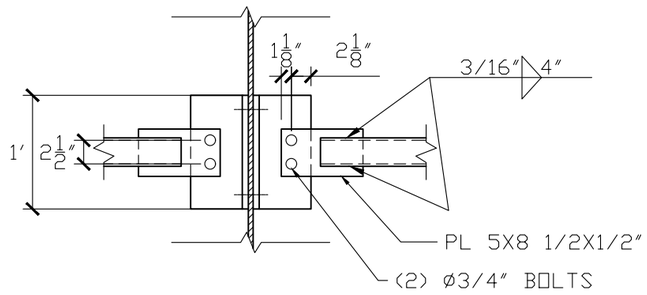

SEE 2/S04.5 FOR WT-COLUMN ATTACHMENT DETAIL

A–A
2/S04.4

General Notes

No.	Revision/Issue	Date

Firm Name and Address

Project Name and Address

NSF Gravity Framing

Project

Date 3/8/2021

Scale As Noted

Sheet S4.4

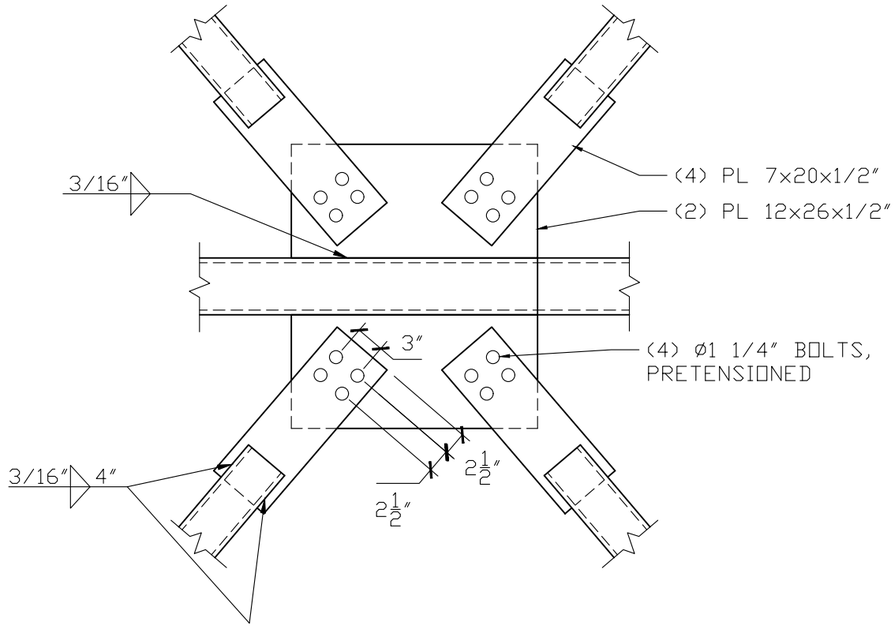

1 DETAIL

SCALE:3/4″ = 1′

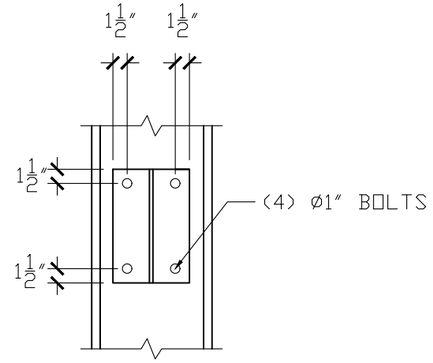

2 DETAIL

SCALE:3/4″ = 1′

General Notes

No.	Revision/Issue	Date

Firm Name and Address

Project Name and Address

NSF Gravity Framing

Project	Sheet
Date 3/8/2021	S4.5
Scale As Noted	

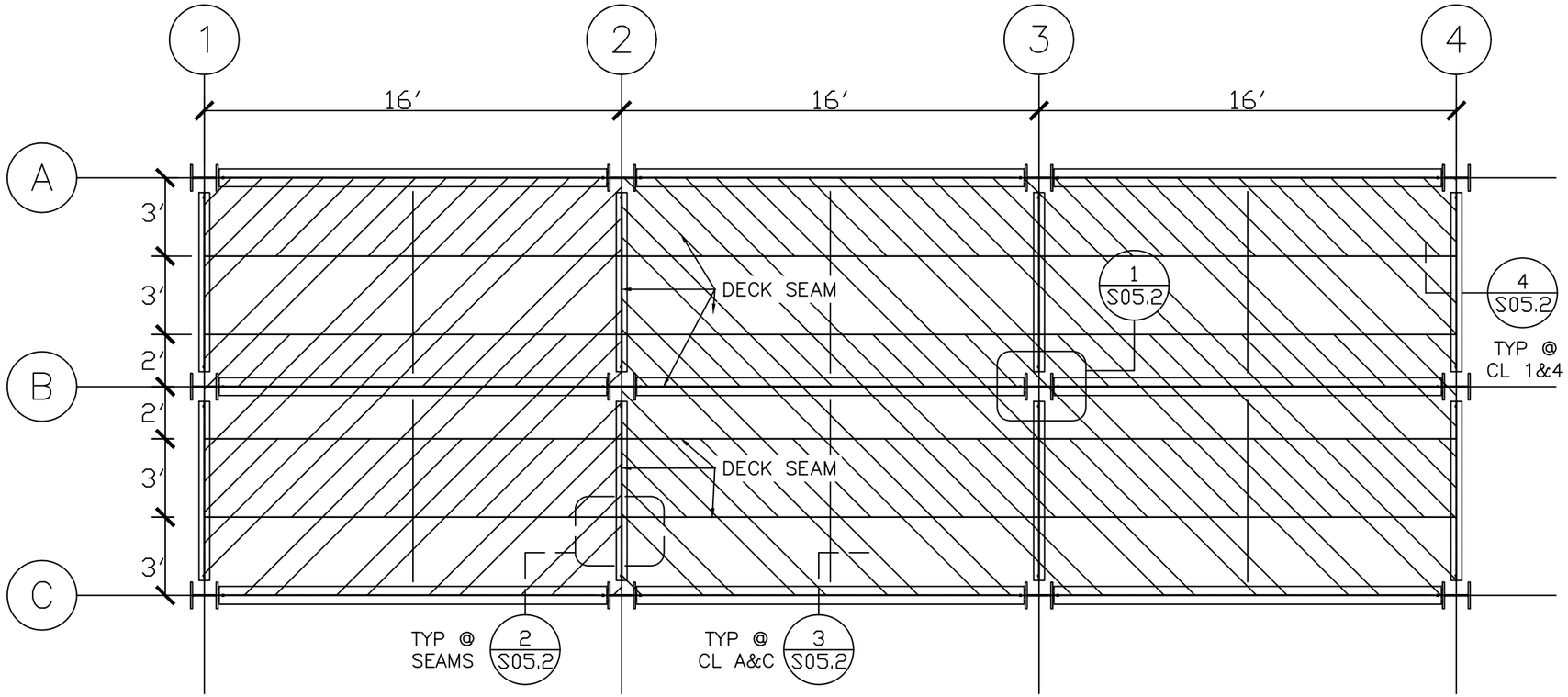

1 DECK ATTACHMENT PLAN

SCALE: 3/16″=1′

N

1. SEE PLAN NOTE 3 ON SHEET S01.1 FOR COMPOSITE FLOOR CONSTRUCTION
2. DECK SEAMS BUTT SPLICED WITH #10 TEK SCREWS
3. POUR STOPS SHALL BE DIMENSIONAL LUMBER AND SHALL BE REMOVED PRIOR TO TESTING

General Notes

No.	Revision/Issue	Date

Firm Name and Address

Project Name and Address

NSF Gravity Framing

Project	Sheet
Date 2/26/2020	S5.1
Scale As Noted	

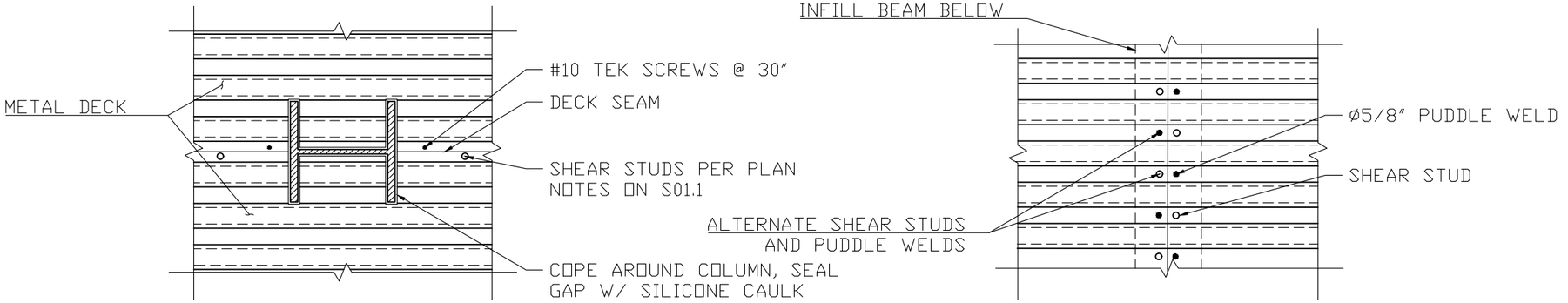

1 DETAIL
SCALE:3/4" = 1'

2 DETAIL
SCALE:3/4" = 1'

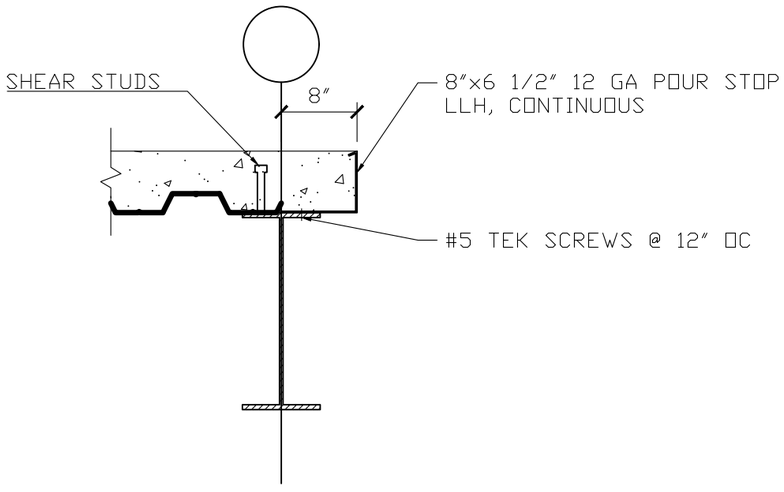

3 DETAIL
SCALE:3/4" = 1'

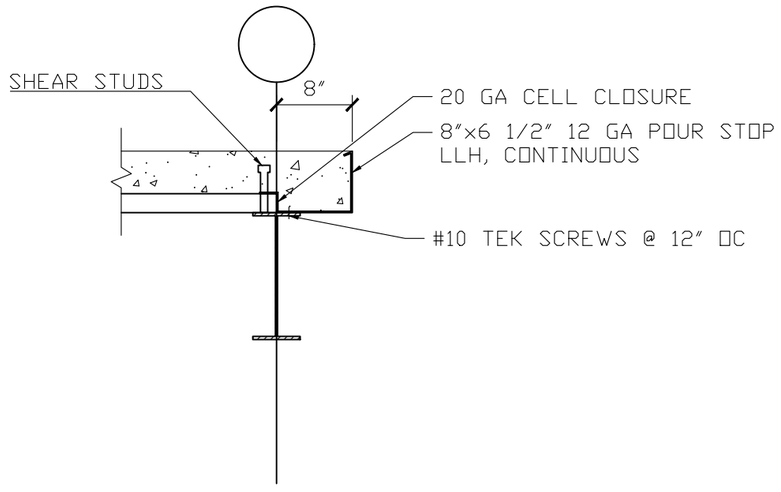

4 DETAIL
SCALE:3/4" = 1'

General Notes

No.	Revision/Issue	Date

Firm Name and Address

Project Name and Address
NSF Gravity Framing

Project

Sheet
S5.2

Date
2/26/2020

Scale
As Noted

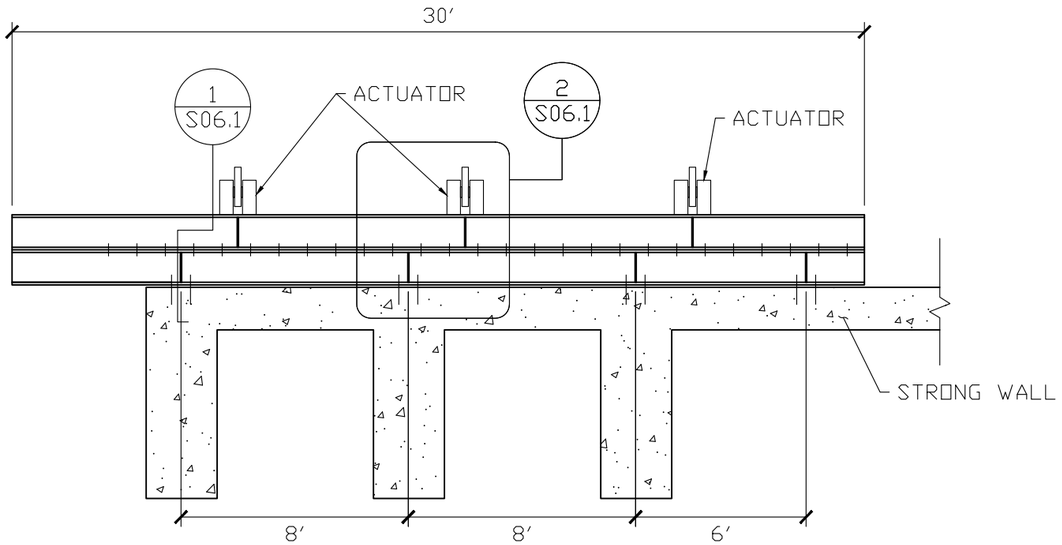

1 STRONG WALL ATTACHMENT PLAN

SCALE: 3/16"=1'

N

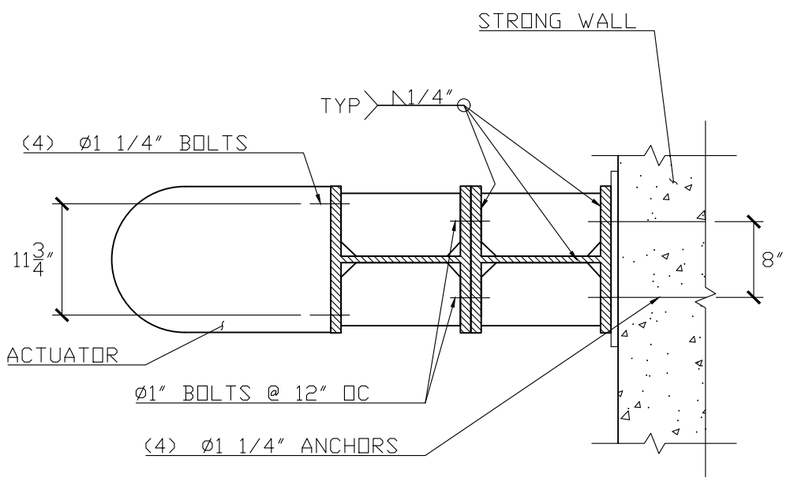

1 DETAIL

SCALE: 3/4" = 1'

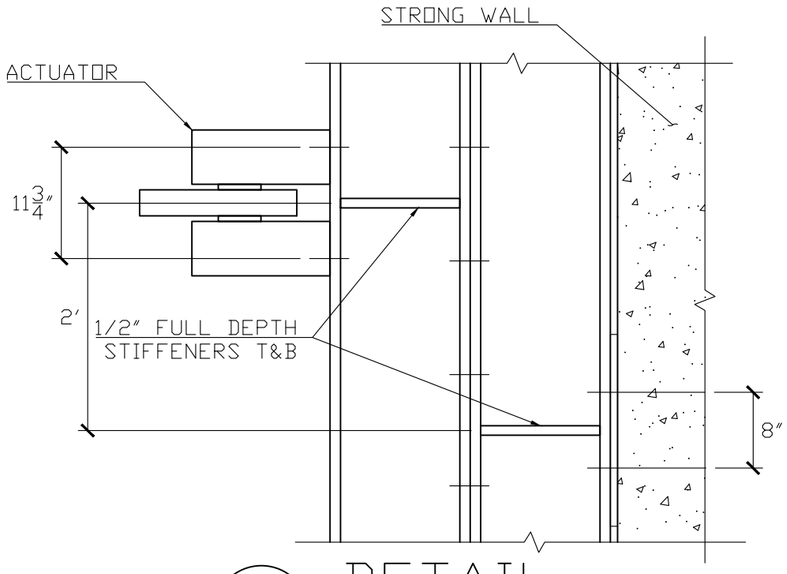

2 DETAIL

SCALE: 3/4" = 1'

General Notes

No.	Revision/Issue	Date

Firm Name and Address

Project Name and Address

NSF Gravity Framing

Project

Date 3/8/2021

Scale As Noted

Sheet S6.1

REFERENCES

ANSYS, Inc. (2019). ANSYS Workbench. Canonsburg, PA.

ASCE. (2006). *Minimum design loads for buildings and other structures.* Reston, VA: American Society of Civil Engineers.

ASCE. (2013). *Seismic rehabilitation of existing buildings (ASCE 41-13).* Reston, VA: American Society of Civil Engineers.

Donahue, S. (2019). *The role of the floor system in the seismic response of steel gravity framing.* Austin, Texas: The University of Texas at Austin, Department of Civil, Architectural, and Environmental Engineering.

FEMA. (2000). *FEMA-355C: State of the Art Report on Systems Performance of Steel Moment Frames Subject to Earthquake Ground Shaking.* Washington DC: FEMA.

FEMA. (2009). *Quantification of building seismic performance factors (FEMA P-695).* Washington, D.C.: Federal Emergency Management Agency.

Flores, F., Charney, F., & Lopez-Garcia, D. (2014). Influence of the gravity framing system on the collapse performance of special steel moment frames. *Journal of Constructional Steel Research, 101,* 351-362.

Foutch, D., & Yun, S. (2002). Modeling of Steel Moment Frames for Seismic Loads. *Journal of Construction Steel Research, 58,* 529-564.

Hernandez, J. (2020). *Preliminary analysis and design of a test setup for evaluating lateral resistance of steel gravity framing systems.* Austin, Texas: The University of Texas at Austin, Department of Civil, Architectural, and Environmental Engineering.

Leon, R. T. (1990). Semi-rigid Composite Construction. *Journal of Constructional Steel Research*, 99-120.

McKenna, F., Fenves, G., & Scott, M. (2006). OpenSees: open system for earthquake engineering simulation. Berkeley, CA: Pacific Earthquake Engineering Center, University of California.

NIST. (2010). *Evaluation of the FEMA P-695 methodology for quantification of building seismic performance factors.* Gaithersburg: National Institute of Standards and Technology.

Saavedra, C. (2020). *Analysis and design of a trop truss diaphragm for cyclic lateral load testing of multi-bay steel gravity frames.* Austin, TX: The University of Texas at Austin.

Shen, J., & Astaneh-Asl, A. (1999). Hysteretic behavior of bolted-angle connections. *Journal of Constructional Steel Research, 51*(3), 201-218.